The Dissertation Committee for Patrick Ryan Fitzpatrick Certifies that this is the approved version of the following dissertation:

Chemical Vapor Deposition of Boron Carbo-Nitride as a Potential Passivation Layer for Germanium Surfaces

Committee:

John G. Ekerdt, Supervisor

Gyeong S. Hwang

Brian A. Korgel

Jack Lee

Charles B. Mullins

Chemical Vapor Deposition of Boron Carbo-Nitride as a Potential Passivation Layer for Germanium Surfaces

by

Patrick Ryan Fitzpatrick, B.S. Ch.E.

Dissertation

Presented to the Faculty of the Graduate School of

The University of Texas at Austin

in Partial Fulfillment

of the Requirements

for the Degree of

Doctor of Philosophy

The University of Texas at Austin

May, 2009

Dedication

To my parents

Acknowledgements

First and foremost I would like to sincerely thank my advisor, Prof. John G. Ekerdt, who served as a constant source of motivation. Based on the high level of success he has reached in his career and the respect among scientific peers that he has earned, his technical insight into my research problems speaks for itself. But I am most impressed by the compassion and concern he has for the students he mentors. He has demonstrated a willingness to always make time for students and to address their problems, no matter how trivial. I think this is what truly separates him from others in his field, and because of that I am proud to have worked for him.

I would also like to thank the other faculty members that have helped steer my graduate research. I am thankful for the thoughtful insight and the genuine interest that Prof. Buddie Mullins and Prof. Gyeong Hwang have taken in my work. I thank Prof. Brian Korgel for the collaboration that he welcomed. And I am grateful to Prof. Jack Lee for extremely helpful electrical testing discussions.

I am very grateful to the fellow research group members who have provided me with valuable training and guidance, especially Ward Engbrecht, Scott Stanley, and Shawn Coffee. They spent countless hours teaching me new techniques in the laboratory to help advance me to the point where I was competent on my own. I have also worked very closely over the years with Tuo Wang, Luke Henderson, Wyatt Winkenwerder, Wes

Ahearn, and Navneet Salivati. Each of these colleagues deserves special thanks for the daily assistance and insightful ideas that they have given me. I am also grateful to the other group members that I have worked along side of, including Jinhong Shin, Kai Wu, Tibor Bolom, Kelly Thom, Hyun Woo Kim, Ben Spivey, Dan Bost, Joe McCrate, and Blair Cox. Several other graduate colleagues were beneficial to my success, most notably Andy Heitsch, Sayan Saha, Davood Shahrjerdi, and Injo Ok. I also worked with several undergraduate and high school students, including Michael Qian, Tiffany Wu, Eric Teletzke, Aditi Ghatak-Roy, and Katie Jaycok. I am thankful for their research assistance.

I would like to extend a special thanks to Ben Spivey for offering me and convincing me to take on an organizational role in the 2008 Graduate And Industry Networking (GAIN) conference. I found the experience to be extremely worthwhile, and it was a pleasure working with him to prepare the event.

I would like to thank The University of Texas at Austin and the Cockrell School of Engineering for the excellent experimental facilities and resources. I would like to give special thanks to the departmental staff of Chemical Engineering for their critical support, especially T Stockman, Kay Swift, Eddie Ibarra, Jim Smitherman, Butch Cunningham, Randy Rife, Kevin Haynes, and Tammy McDade. The Center for Nano and Molecular Science and Technology (CNM) was especially helpful throughout the course of my research. I owe a special thanks to Dr. Bill Lackowski and Mike Tiner for their assistance with CNM equipment and insightful research ideas. I would also like to thank Mr. C. W. W. Cook for the financial support of the Thrust 2000 Fellowship that I received for many of my years here.

Finally I would like to thank all of the loved ones in my life. The process has been made tolerable by the enduring support of my parents, Patrick and Michele

Fitzpatrick; the constant encouragement of my sisters, Jordyn and Devan; and the endless patience of Danielle. I am also thankful for the many close friends I have made throughout the course of my life and the support they have given me. Without the support of all of these people I would lack the motivation necessary to succeed at any venture in life.

Chemical Vapor Deposition of Boron Carbo-Nitride as a Potential Passivation Layer for Germanium Surfaces

Publication No._____

Patrick Ryan Fitzpatrick, Ph.D.

The University of Texas at Austin, 2009

Supervisor: John G. Ekerdt

Motivated by the need for a Ge surface passivation layer, chemical vapor deposition of thin (< 10 nm) films of amorphous boron carbo-nitride (BC_xN_y) on Ge(100) surfaces were studied to assess film continuity, interface bonding, Ge oxidation prevention, and electrical passivation. BC_xN_y nominally 2.5–5 nm thick continuously covers Ge(100), as determined by ion scattering spectroscopy and two angle resolved x-ray photoelectron spectroscopy (ARXPS) techniques. ARXPS analysis reveals no evidence of an interfacial layer due to elemental intermixing at the BC_xN_y–Ge(100) interface. High resolution transmission electron microscopy images of HfO_2 / BC_xN_y / Ge(100) cross-sections reveal abrupt BC_xN_y–Ge(100) interfaces. XPS was used to track Ge oxidation of BC_xN_y-covered Ge(100) upon exposure to ambient, 50 °C deionized water, and a 250 °C atomic layer deposition HfO_2 process. If the BC_xN_y layer is continuous (≥ ~ 4 nm), the underlying Ge(100) surface is not oxidized despite incorporation of O into BC_xN_y. Thinner films (≤ 3.2 nm) permitted Ge(100) oxidation in each oxidizing environment studied. Ge nanowires with a 5.7 nm BC_xN_y coating were

resistant to oxidation for at least 5 months of ambient exposure. *C–V* and *I–V* measurements were made for metal-insulator-semiconductor (MIS) structures fabricated from n-Si(100) and n-Ge(100) wafers passivated with 4.5–5 nm BC_xN_y. C-rich $BC_{0.61}N_{0.08}$ films studied up to this point exhibited large amounts of hysteresis and fixed negative charge, so they were abandoned in favor of N-rich BC_xN_y ($0.09 \leq x \leq 0.15$, $0.38 \leq y \leq 0.52$). N-rich BC_xN_y grown at 275–400 ºC showed that lower deposition temperatures resulted in improved electrical characteristics, including decreased hysteresis, lower V_{FB} shift, lower leakage current, and less *C–V* stretch-out. The electrical improvement is attributed to decreased bulk and interfacial defects in BC_xN_y deposited at lower temperatures. Even for the lowest growth temperature studied (275 ºC), BC_xN_y-passivated Ge(100) devices had considerable hysteresis and electrical characteristics worsened after a post-metallization anneal. BC_xN_y-passivated Si(100) devices outperformed similar Ge(100) devices, likely due to the higher interface state densities at the BC_xN_y–Ge(100) interface associated with the higher relative inertness of Ge(100) to thermal nitridation.

Table of Contents

List of Tables

List of Figures

List of Illustrations

Chapter 1: Introduction

1.1. OVERVIEW

For roughly 50 years, Si has served as the primary semiconductor material for transistors and integrated circuits. Its longevity is attributed to the stability of its oxide, SiO_2, which is used as the dielectric material in metal-oxide-semiconductor field-effect transistors (MOSFETs). The interface that forms naturally between Si and SiO_2 has a low density of interface states (~ 10^{10} cm^{-2} for carefully prepared Si(100) surfaces) [1]. Such a defect-free interface is essential to the electrical performance of the device.

In a trend known as Moore's Law, the density of transistors on an integrated circuit has approximately doubled every 18 to 24 months [2]. This has been achieved through significant scaling of the transistor dimensions. As a result, the required thickness of the SiO_2 dielectric layer has shrunk to less than 1 nm [3]. With such a thin dielectric layer, enhanced leakage current due to electron tunneling through the dielectric is detrimental to device performance. This has motivated a shift towards new dielectric materials with higher dielectric constants, *e.g.* HfO_2 and ZrO_2. With movement away from SiO_2, the choice of semiconductor material is no longer limited to Si.

Ge has attracted considerable attention in the semiconductor industry in recent years, partly due to is chemical similarity to Si. The greater motivation for switching to Ge, however, is the higher intrinsic carrier mobility in Ge compared to Si. At 27 °C and low impurity concentrations (10^{14} – 10^{15} cm^{-3}), Ge hole and electron mobilities are approximately 2000 and 4500 cm^2/V-s, respectively. Under the same conditions Si hole and electron mobilities are approximately 450 and 1500 cm^2/V-s, respectively [4]. This

Ge advantage leads to higher drive currents in MOSFET devices. Additionally, dopant activation in Ge is possible at a lower temperature than in Si [5].

The major drawback to Ge, however, is the unstable native oxide that easily forms on its surface. Unlike SiO_2, GeO_2 is both water-soluble and thermally unstable, thus complicating processing of Ge devices. Furthermore, a high density of interface states (> 10^{13} cm^{-2}) makes the Ge–GeO_x interface electrically unstable [6]. These interface states serve as charge traps, which reduce mobility and also contribute to device hysteresis [6-8]. The use of Ge in MOSFET devices is also complicated by unstable germanide formation upon high-κ oxide deposition. Recent studies have shown that HfO_2 deposition on Ge(100) is especially troublesome due to Hf–Ge bond formation, which produces interface states in the band gap [9,10].

A passivation layer is needed to chemically and electrically stabilize the surface of Ge and make it viable for use in electronic applications. Illustration 1.1 depicts a MOSFET cross-section, in which the passivation film serves as an interfacial layer between the semiconductor channel and the gate dielectric. The first requirement of the passivation layer is that it should form a continuous layer on the Ge surface. Discontinuous coverage would not only allow formation of the unstable GeO_x, but additional poor interfaces could result during device processing. The continuous layer also needs to be as thin and uniform as possible, especially if the film will serve as an interface between Ge and a high-κ dielectric in a MOSFET. Films that are too thick lower the effective dielectric constant of the high-κ / passivation layer film stack. To preserve the equivalent oxide thickness the physical thickness of this gate oxide stack must then decrease, which makes it more susceptible to leakage.

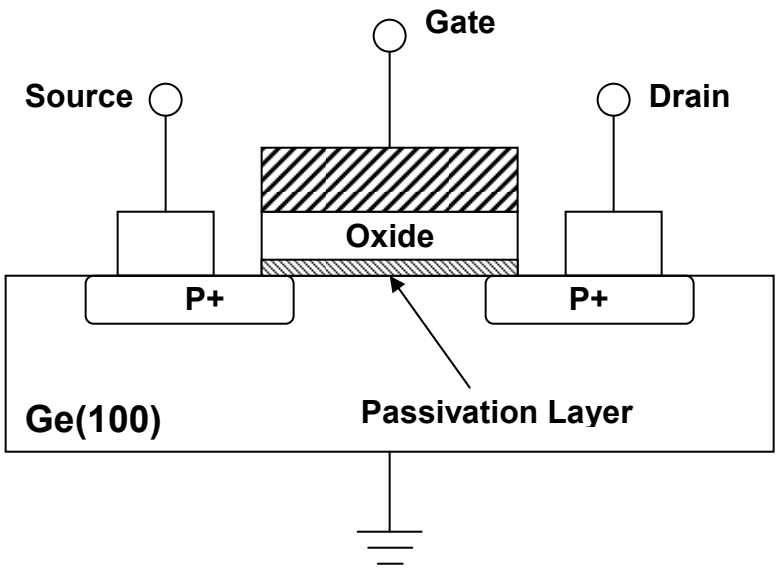

Illustration 1.1. Cross-section cartoon of pMOSFET on Ge(100) substrate highlighting the passivation layer at the interface between the semiconductor channel and gate dielectric.

The second requirement is that the passivating layer should form a clean, abrupt interface with Ge. A poor interface where the passivating film intermixes with the Ge surface will result in mechanical or electrical defects. Beyond not intermixing with the Ge, the passivation layer should also form an interface with Ge in which the crystalline lattice structure of bulk Ge is preserved at the passivation layer interface. Otherwise, interface states can result from a distortion of the Ge surface bonds, which will cause increased carrier scattering and reduce device performance [8].

The passivation layer should also be chemically stable in multiple oxidizing environments. During MOSFET device fabrication, the passivating film must resist oxidation of the underlying Ge substrate during deposition of a high-κ gate oxide as well as during potential exposure to aqueous environments. For this application, it may be

sufficient to protect the Ge substrate from oxidation just long enough to reach the next step in the device processing sequence. As MOSFET fabrication proceeds, the multiple layers on top of the passivated Ge surface will prevent the semiconductor from being exposed to additional harsh environments throughout the lifetime of the device.

However, the use of Ge in electronics is not limited solely to MOSFETs. Ge also plays a role in solar cells [11], microelectromechanical systems [12], chemical sensors [13], and infrared detectors [14,15]. Furthermore, Ge nanowires (GeNWs) have also been the focus of substantial research, due to their potential use in various nanoelectronic and photonic devices [7,8,16-18]. These alternative Ge applications present their own unique passivation challenges. For some Ge(100) and GeNW applications (e.g. chemical sensors), the passivating layer may be the only material between the operating Ge device and the ambient environment. For such a device to be effective it may not be enough for the passivating film to merely protect the device until the next processing step. Rather, the passivating film must preserve the chemical and electrical integrity of the Ge surface for the lifetime of the device upon exposure to numerous environments.

1.2. CURRENT RESEARCH

1.2.1. Ge Passivation

Substantial efforts have been made to passivate Ge surfaces by making Ge oxidation resistant. Hydrogen termination by either dry [19-22] (vacuum adsorption of atomic hydrogen) or wet [23-26] (HF etch) treatment was one approach taken to passivate Ge surfaces. Another approach has been to etch the oxide with HCl, temporarily passivating the Ge in the process through Cl-termination [7,23-25,27,28]. However both of these treatments have shown very limited stability with prolonged

ambient exposure. A more promising passivation technique has been by sulfide termination. Ge surfaces with sulfur overlayers have demonstrated oxidation resistance when exposed to ambient for several days [23,25,29,30]. However, when aqueous sulfidation treatment is applied to GeNWs, one study observed the formation of a 5 nm GeS_x layer, which is undesirable for electronic device applications [23].

A number of studies have investigated organic passivation layers [23,25,26,28,31-37]. Organic functionalization has been achieved by either hydrogermylation reactions, alkanethiol reactions, or Grignard reactions on Cl-terminated Ge surfaces. Organic passivated Ge surfaces have demonstrated varying degrees of stability. In general, organically passivated surfaces resist oxidation better than H- or Cl- terminated surfaces. In one study, Grignard-alkylated Ge (111) surfaces resisted oxidation upon 5 days exposure to ambient [33].

Ultrathin (<1 nm) Si layers grown on Ge have also demonstrated improved Ge oxidation resistance in addition to improved electrical characteristics. In one study, metal-insulator-semiconductor (MIS) devices incorporating HfO_2 and Ge show improved C–V characteristics when epitaxially grown Si is used to passivate the Ge surface prior to HfO_2 deposition [38]. This improvement is indicative of a reduction in the number of interface states at the Ge surface. In another study Si is used to passivate Ge nMOSFETs prior to deposition of the HfO_2 gate dielectric [39]. The result of this effort is a 61% improvement in the peak electron mobility of the Ge device relative to a control HfO_2 / Si device.

Another approach to passivation has been to employ nitrogen to produce GeON or Ge_3N_4 [40-44]. The incorporation of N into the interfacial passivation layer has been shown to reduce the density of interface states and prevent the interdiffusion of Ge or high-κ species across the passivation interface [40,41,43,45]. One study used a Ge

oxynitride passivation layer in constructing a Ge pMOSFET that had twice the hole mobility of a Si control device [46]. The passivation layer was deposited by evaporating Ge in an oxygen and nitrogen plasma environment. In another study nitridation of the surface was done by a rapid thermal NH_3 annealing prior to depositing the HfO_2 gate dielectric [47]. A 2.5× improvement in the electron mobility of this Ge nMOSFET relative to Si control devices was achieved.

Recent research has shown that if oxidation of a clean Ge surface is done in a controlled manner, GeO_2 can actually electrically passivate a Ge surface. Low interface state densities (mid-10^{11} $cm^{-2}eV^{-1}$) have been reported for MIS capacitors consisting of GeO_2 / Ge(100) interfaces [10,48,49]. However, complications arise during subsequent device processing due to GeO_2 dissociation and GeO out-diffusion around 430–450 ° C [50]. Integration of the GeO_2 / Ge stack with a high-κ dielectric also degrades device performance due to intermixing of many dielectrics, such as ZrO_2 and HfO_2, with GeO_2 [48]. First-principles simulations have shown that surface states do not arise from Ge–O or Ge–O–Hf bonding, but rather from the more metallic Hf–Ge bonding of Hf germanide [10]. Thus, despite the recent ability to form a GeO_2 / Ge interface that is electrically passivated, integration with a suitable high-κ dielectric remains a challenge.

The challenge of passivating Ge surfaces is also complicated by the substrate charge carrier type. While some passivation efforts have been successful at reducing interface state densities (low to mid 10^{11} cm^{-2}) [43,48] and improving mobility for pMOS Ge devices [51-53], n-type devices continue to perform poorly [39,54,55]. The reason for the increased surface passivation difficulty in n-type devices is still being debated [39,47,56]. But it has been suggested that an enhanced sensitivity to band alignment with interfacial layers [56] or impurity induced structural defects at the Ge surface [47] may be a factor in the deterioration of electrical properties.

1.2.2. Boron Carbo-Nitride

The research of this thesis will focus on the effectiveness of boron carbo-nitride (BC_xN_y, henceforth referred to as BCN for simplicity) as a passivation layer for Ge surfaces. Significant attention has been given to B–C–N ternary compounds grown by a variety of techniques. The wide range of growth conditions studied thus far has resulted in a material class with vastly tunable properties, including microstructure, crystallinity, hardness, and dielectric constant [57-66].

Several studies involving BCN suggest its use as a passivating film is promising. For example, BCN is reported to form a smooth interfacial layer when deposited on Si(100), a substrate chemically similar to Ge(100) [64]. In passivation efforts, controlling the chemistry and thickness of the interface that BCN forms with Ge will be essential in minimizing the number of interface states and preserving the electrical integrity of the Ge surface. Therefore a thin, smooth interface is desirable. The ability of B, C, and N to bond with Si or Ge makes such an interface achievable without introducing excessive interface traps.

In addition to forming a good interface, a passivation layer needs to be chemically stable and oxidation resistant. An Auger electron spectroscopy concentration depth profile of a SiCBN film pyrolyzed at 900 ºC reveals an extremely uniform atomic profile throughout the bulk of the film. Exposure to air for 8 h at 1000 ºC resulted in only a slight mass gain of 0.11 % by the same film [67]. This indicates the SiCBN film has excellent oxidation resistance. The non-oxidic nature of BCN also suggests that Ge will not oxidize during the deposition process.

The promising electrical characteristics of BCN on semiconductor substrates are evident in a report that claims interface state densities as low as 1.1×10^{11} eV^{-1} cm^{-2} for

S-doped BCN films deposited on GaAs [68]. Furthermore, based on the mobility improvements of devices with nitridated Ge surfaces discussed above, BCN films that are N-rich may electrically passivate Ge surfaces. Additional evidence of BCN's promising electrical properties comes from work in our laboratories. 50 nm $BC_{0.90}N_{0.08}$, of similar stoichiometry to many of the films in this study, exhibited low leakage current when used in MIS capacitor structures [59].

In our laboratory amorphous BCN is grown by thermal chemical vapor deposition (CVD) using dimethylamine borane (DMAB) as a single-source precursor with Ar as a carrier gas. To tailor the stoichiometric composition as well as the relative amounts of B–B, B–C, and B–N bonding, ethylene and ammonia are used in varying proportions as coreactants with DMAB. Changing the constituent bonding in this manner provides the flexibility to alter the dielectric constant and electrical leakage of BCN, two properties that will be important in the integration of passivated Ge surfaces into electronic devices. BC_xN_y grown in our laboratory has tunable stoichiometry ($0.05 \leq x \leq 1.51$, $0.05 \leq y \leq 0.67$) and dielectric constant ($3.7 \leq \kappa \leq 4.6$) depending on the reaction conditions [66].

1.3. Objective and Overview of Chapters

The objective of this work is to determine the ability of BCN grown by CVD to passivate Ge(100) and GeNW surfaces. This will include a study of the minimum film thickness that results in continuous coverage of Ge(100) as well as examination of the BCN–Ge(100) interface that forms (Chapter 2). Chapter 3 examines the ability of BCN to resist oxidation of Ge(100) and GeNW substrates in multiple oxidizing environments. The ultimate test of BCN's effectiveness as a passivation layer is to determine how well BCN-passivated Ge devices perform electrically. This is addressed in Chapter 4 through the electrical testing of MIS capacitors fabricated on BCN-passivated Ge(100). Chapter

5 presents a summary of the ability of BCN to passivate Ge surfaces as well as suggestions for future work.

Chapter 2 presents a study of film continuity and interface bonding for thin (< 10 nm) films of amorphous BCN deposited on Ge(100) substrates. CVD on Ge(100) and Si(100) (studied for comparison) produced $BC_{0.75}N_{0.07}$ and $BCN_{0.07}$ stoichiometry films, respectively. When BCN is nominally 2.5–5 nm thick, the film's coverage of Ge(100) is continuous. This range was determined by (i) 0.5 kV He^+ ion scattering spectroscopy scans, in which the underlying Ge(100) substrate signal disappears upon continuous BCN coverage and (ii) the convergence to unity of the ratio of BCN thicknesses estimated by two angle resolved x-ray photoelectron spectroscopy (ARXPS) techniques. Only 1.5–2 nm BCN was required for continuous coverage of Si(100), possibly due to better nucleation on this surface. ARXPS analysis indicates that the BCN–Ge(100) interface is clean and abrupt, with no evidence of an interfacial layer due to elemental intermixing. Constituent bonding in the BCN bulk is maintained at the Ge(100) interface. Preservation of the Ge 3*d* and Ge 2*p* full-width-half-maximum values after BCN deposition suggests a lack of distortion of Ge surface bonds, a criterion necessary for passivation if low interface state densities are to be achieved. BCN–Si(100) interface characteristics were similar to BCN–Ge(100).

In Chapter 3, CVD of thin (< 10 nm) films of amorphous BCN ($BC_{0.7}N_{0.08}$ stoichiometry) on Ge(100) and GeNW surfaces was studied to determine the ability of BCN to prevent oxidation of Ge. XPS was used to track Ge oxidation of BCN-covered Ge(100) upon exposure to ambient, 50 °C deionized water, and a 250 °C atomic layer deposition (ALD) HfO_2 process. BCN overlayers incorporate O immediately upon ambient or water exposure, but it is limited to 15% O uptake. If the BCN layer is continuous, the underlying Ge(100) surface is not oxidized despite the incorporation of O

into BCN. The minimum continuous BCN film thickness that prevents Ge(100) oxidation is ~ 4 nm. Thinner films (≤ 3.2 nm) permitted Ge(100) oxidation in each of the oxidizing environments studied. GeNWs with a 5.7 nm BCN coating were resistant to oxidation for at least 5 months of ambient exposure. High resolution transmission electron microscopy images of HfO_2 / BCN / Ge(100) cross-sections and BCN-coated GeNWs reveal clean, abrupt BCN–Ge(100) interfaces.

In Chapter 4, MIS structures were fabricated from n-Ge(100) and n-Si(100) (for comparison) wafers passivated with thin (4.5–5 nm) films of N-rich BC_xN_y ($0.09 \leq x \leq 0.15$, $0.38 \leq y \leq 0.52$) and with ALD HfO_2 (10 nm) as the gate dielectric. *C–V* and *I–V* characteristics of devices with BC_xN_y films grown at 275–400 ºC by CVD showed that lower deposition temperatures resulted in improved electrical characteristics, including decreased hysteresis, lower V_{FB} shift, lower leakage current, and less *C–V* stretch-out. The electrical improvement is attributed to decreased bulk and interfacial defects in BC_xN_y deposited at lower temperatures, which also has a higher optical band gap (E_g = 3.55 eV at 275 ºC on Ge(100)), lower sub-band gap absorption, lower index of refraction (n(633 nm) = 1.84 at 275 ºC on Ge(100)), reduced O uptake during ambient exposure, and increased %B. Even for the lowest growth temperature studied (275 ºC), BC_xN_y-passivated Ge(100) devices had considerable hysteresis (1.05 V) and electrical characteristics worsened after a post-metallization anneal. BC_xN_y-passivated Si(100) devices outperformed similar Ge(100) devices, likely due to the higher interface state densities at the BC_xN_y–Ge(100) interface associated with the higher relative inertness of Ge(100) to thermal nitridation. C-rich $BC_{0.61}N_{0.08}$ films were also investigated, but large amounts of hysteresis and fixed negative charge motivated the abandonment of these films.

1.4. REFERENCES

[1] B. G. Streetman and S. Banerjee, *Solid State Electronic Devices*, Fifth Edition ed. (Prentice Hall, Upper Saddle River, New Jersey, 2000).

[2] G. E. Moore, Electronics **38**, 114 (1965).

[3] *International Technology Roadmap for Semiconductors 2007 Update*. (SIA, 2008).

[4] S. M. Sze, *Physics of Semiconductor Devices*, Second ed. (John Wiley & Sons, New York, 1981).

[5] P. W. Loscutoff and S. F. Bent, Annu. Rev. Phys. Chem. **57**, 467 (2006).

[6] R. H. Kingston, J. Appl. Phys. **27**, 101 (1956).

[7] D. W. Wang, Y. L. Chang, Q. Wang, J. Cao, D. B. Farmer, R. G. Gordon, and H. J. Dai, J. Am. Chem. Soc. **126**, 11602 (2004).

[8] D. W. Wang, Q. Wang, A. Javey, R. Tu, H. J. Dai, H. Kim, P. C. McIntyre, T. Krishnamohan, and K. C. Saraswat, Appl. Phys. Lett. **83**, 2432 (2003).

[9] M. Houssa, G. Pourtois, B. Kaczer, B. De Jaeger, F. E. Leys, D. Nelis, K. Paredis, A. Vantomme, M. Caymax, M. Meuris, and M. M. Heyns, Microelectron. Eng. **84**, 2267 (2007).

[10] M. Caymax, M. Houssa, G. Pourtois, F. Bellenger, K. Martens, A. Delabie, and S. Van Elshocht, Appl. Surf. Sci. **254**, 6094 (2008).

[11] D. Poelman, P. Clauws, and B. Depuydt, Sol. Energy Mater. **76**, 167 (2003).

[12] B. Li, B. Xiong, L. N. Jiang, Y. Zohar, and M. Wong, J. Microelectromech. Syst. **8**, 366 (1999).

[13] M. Koto, P. W. Leu, and P. C. McIntyre, J. Electrochem. Soc. **156**, K11 (2009).

[14] H. Temkin, T. P. Pearsall, J. C. Bean, R. A. Logan, and S. Luryi, Appl. Phys. Lett. **48**, 963 (1986).

[15] M. Oehme, J. Werner, M. Kaschel, O. Kirfel, and E. Kasper, Thin Solid Films **517**, 137 (2008).

[16] A. M. Morales and C. M. Lieber, Science **279**, 208 (1998).

[17] T. Hanrath and B. A. Korgel, J. Am. Chem. Soc. **124**, 1424 (2002).

[18] A. D. Schricker, S. V. Joshi, T. Hanrath, S. K. Banerjee, and B. A. Korgel, J. Phys. Chem. B **110**, 6816 (2006).

[19] J. A. Appelbaum, G. A. Baraff, D. R. Hamann, H. D. Hagstrum, and T. Sakurai, Surf. Sci. **70**, 654 (1978).

[20] Y. J. Chabal, Surf. Sci. **168**, 594 (1986).

[21] J. Y. Maeng, J. Y. Lee, Y. E. Cho, S. Kim, and S. K. Jo, Appl. Phys. Lett. **81**, 3555 (2002).

[22] L. Papagno, X. Y. Shen, J. Anderson, G. S. Spagnolo, and G. J. Lapeyre, Phys. Rev. B **34**, 7188 (1986).

[23] T. Hanrath and B. A. Korgel, J. Am. Chem. Soc. **126**, 15466 (2004).

[24] H. Adhikari, P. C. McIntyre, S. Y. Sun, P. Pianetta, and C. E. D. Chidsey, Appl. Phys. Lett. **87** (2005).

[25] D. Bodlaki, H. Yamamoto, D. H. Waldeck, and E. Borguet, Surf. Sci. **543**, 63 (2003).

[26] K. Choi and J. M. Buriak, Langmuir **16**, 7737 (2000).

[27] Z. H. Lu, Appl. Phys. Lett. **68**, 520 (1996).

[28] G. W. Cullen, J. A. Amick, and D. Gerlixh, J. Electrochem. Soc. **109**, 124 (1962).

[29] G. W. Anderson, M. C. Hanf, P. R. Norton, Z. H. Lu, and M. J. Graham, Appl. Phys. Lett. **66**, 1123 (1995).

[30] P. F. Lyman, O. Sakata, D. L. Marasco, T. L. Lee, K. D. Breneman, D. T. Keane, and M. J. Bedzyk, Surf. Sci. **462**, L594 (2000).

[31] D. W. Wang, Y. L. Chang, Z. Liu, and H. J. Dai, J. Am. Chem. Soc. **127**, 11871 (2005).

[32] T. Hanrath and B. A. Korgel, J. Phys. Chem. B **109**, 5518 (2005).

[33] J. L. He, Z. H. Lu, S. A. Mitchell, and D. D. M. Wayner, J. Am. Chem. Soc. **120**, 2660 (1998).

[34] S. M. Han, W. R. Ashurst, C. Carraro, and R. Maboudian, J. Am. Chem. Soc. **123**, 2422 (2001).

[35] A. V. Teplyakov, P. Lal, Y. A. Noah, and S. F. Bent, J. Am. Chem. Soc. **120**, 7377 (1998).

[36] R. J. Hamers, J. S. Hovis, C. M. Greenlief, and D. F. Padowitz, Jpn. J. Appl. Phys., Part 1 **38**, 3879 (1999).

[37] S. W. Lee, L. N. Nelen, H. Ihm, T. Scoggins, and C. M. Greenlief, Surf. Sci. **410**, L773 (1998).

[38] S. Van Elshocht, M. Caymax, T. Conard, S. De Gendt, I. Hoflijk, M. Houssa, F. Leys, R. Bonzom, B. De Jaeger, J. Van Steenbergen, W. Vandervorst, M. Heyns, and M. Meuris, Thin Solid Films **508**, 1 (2006).

[39] N. Wu, Q. C. Zhang, D. S. H. Chan, N. Balasubramanian, and C. X. Zhu, IEEE Electron Device Lett. **27**, 479 (2006).

[40] H. Kim, P. C. McIntyre, C. O. Chui, K. C. Saraswat, and M.-H. Cho, Appl. Phys. Lett. **85**, 2902 (2004).

[41] N. Lu, W. Bai, A. Ramirez, C. Mouli, A. Ritenour, M. L. Lee, D. Antoniadis, and D. L. Kwong, Appl. Phys. Lett. **87**, 051922 (2005).

[42] S. J. Wang, J. W. Chai, J. S. Pan, and A. C. H. Huan, Appl. Phys. Lett. **89**, 022105 (2006).

[43] T. Maeda, M. Nishizawa, Y. Morita, and S. Takagi, Appl. Phys. Lett. **90**, 072911 (2007).

[44] G. Lucovsky, J. P. Long, K.-B. Chung, H. Seo, B. Watts, R. Vasic, and M. D. Ulrich, J. Vac. Sci. Technol. B **27**, 294 (2009).

[45] T. Sugawara, Y. Oshima, R. Sreenivasan, and P. C. McIntyre, Appl. Phys. Lett. **90** (2007).

[46] A. Ritenour, A. Khakifirooz, D. A. Antoniadis, R. Z. Lei, W. Tsai, A. Dimoulas, G. Mavrou, and Y. Panayiotatos, Appl. Phys. Lett. **88** (2006).

[47] W. P. Bai, N. Lu, A. Ritenour, M. L. Lee, D. A. Antoniadis, and D. L. Kwong, IEEE Electron Device Lett. **27**, 175 (2006).

[48] A. Delabie, F. Bellenger, M. Houssa, T. Conard, S. Van Elshocht, M. Caymax, M. Heyns, and M. Meuris, Appl. Phys. Lett. **91** (2007).

[49] H. Matsubara, T. Sasada, M. Takenaka, and S. Takagi, Appl. Phys. Lett. **93** (2008).

[50] S. Takagi, T. Maeda, N. Taoka, M. Nishizawa, Y. Morita, K. Ikeda, Y. Yamashita, M. Nishikawa, H. Kumagai, R. Nakane, S. Sugahara, and N. Sugiyama, Microelectron. Eng. **84**, 2314 (2007).

[51] S. Joshi, C. Krug, D. Heh, H. J. Na, H. R. Harris, J. W. Oh, P. D. Kirsch, P. Majhi, B. H. Lee, H. H. Tseng, R. Jammy, J. C. Lee, and S. K. Banerjee, IEEE Electron Device Lett. **28**, 308 (2007).

[52] K. Saraswat, C. O. Chui, T. Krishnamohan, D. Kim, A. Nayfeh, and A. Pethe, Mater. Sci. Eng., B **135**, 242 (2006).

[53] G. Nicholas, D. P. Brunco, A. Dimoulas, J. Van Steenbergen, F. Bellenger, M. Houssa, M. Caymax, M. Meuris, Y. Panayiotatos, and A. Sotiropoulos, IEEE Trans. Electron Devices **54**, 1425 (2007).

[54] R. L. Xie, N. Wu, C. Shen, and C. X. Zhu, Appl. Phys. Lett. **93** (2008).

[55] H. L. Shang, K. L. Lee, P. Kozlowski, C. D'Emic, I. Babich, E. Sikorski, M. K. Ieong, H. S. P. Wong, K. Guarini, and N. Haensch, IEEE Electron Device Lett. **25**, 135 (2004).

[56] G. Lucovsky, S. Lee, J. P. Long, H. Seo, and J. Lüning, Appl. Surf. Sci. **254**, 7933 (2008).

[57] W. J. Ahearn, P. R. Fitzpatrick, and J. G. Ekerdt, J. Vac. Sci. Technol. A **25**, 570 (2007).

[58] E. R. Engbrecht, P. R. Fitzpatrick, K. H. Junker, Y. M. Sun, J. M. White, and J. G. Ekerdt, J. Mater. Res. **20**, 2218 (2005).

[59] E. R. Engbrecht, Y. M. Sun, K. H. Junker, J. M. White, and J. G. Ekerdt, J. Vac. Sci. Technol. B **23**, 463 (2005).

[60] T. Sugiyama, T. Tai, and T. Sugino, Appl. Phys. Lett. **80**, 4214 (2002).

[61] Z. J. Zhang, C. Kimura, and T. Sugino, J. Appl. Phys. **98**, 036105 (2005).

[62] M. N. Uddin, M. Shimoyama, Y. Baba, T. Sekiguchi, and M. Nagano, J. Vac. Sci. Technol. A **23**, 497 (2005).

[63] M. Mieno and T. Satoh, J. Mater. Sci. **36**, 3925 (2001).

[64] M. K. Lei, Q. Li, Z. F. Zhou, I. Bello, C. S. Lee, and S. T. Lee, Thin Solid Films **389**, 194 (2001).

[65] Z. F. Zhou, I. Bello, M. K. Lei, K. Y. Li, C. S. Lee, and S. T. Lee, Surf. Coat. Technol. **128-129**, 334 (2000).

[66] E. R. Engbrecht, Y. M. Sun, K. H. Junker, J. M. White, and J. G. Ekerdt, J. Vac. Sci. Technol. A **22**, 2152 (2004).

[67] Q. D. Nghiem and D. P. Kim, J. Mater. Chem. **15**, 2188 (2005).

[68] S. Umeda, T. Yuki, T. Sugiyama, and T. Sugino, Diamond Relat. Mater. **13**, 1135 (2004).

Chapter 2: Film Continuity and Interface Bonding of BC_xN_y on Si(100) and Ge(100)

2.1. INTRODUCTION

As the dimensions of electronic devices such as field effect transistors (FETs) are scaled down, considerable attention is being given to Ge as an alternative to Si as the semiconducting material. The primary motivation for such a change is the higher mobility of holes and electrons in Ge compared to Si. At 300K and low impurity concentrations (10^{14}–10^{15} cm^{-3}), Ge hole and electron mobilities are approximately 2000 and 4500 $cm^2/V–s$, respectively. Under the same conditions Si hole and electron mobilities are approximately 450 and 1500 $cm^2/V–s$, respectively [1]. This Ge advantage leads to better device performance. Additionally, dopant activation in Ge is possible at a lower temperature than in Si [2]. However, the Ge–GeO_x interface is unstable. GeO_2 is soluble in H_2O, inviting H_2O adsorption on unpassivated Ge. This H_2O adsorption has been shown to cause hysteresis in unpassivated Ge nanowire (GeNW) devices [3]. In addition to the chemical instability of the Ge–GeO_x interface, a high number of surface states ($> 10^{13}$ cm^{-2}) are also present making the interface electrically unstable [4]. These surface states serve as charge traps, which also contribute to device hysteresis [3-5].

A passivation layer is needed to chemically and electrically stabilize the surface of Ge and make it viable for use in electronic applications. The first requirement of the passivation layer is that it should form a continuous layer on the Ge surface. Discontinuous coverage would not only allow formation of the unstable GeO_x, but additional poor interfaces could result during device processing. The continuous layer also needs to be as thin and uniform as possible, especially if the film will serve as an

interface between Ge and a high κ dielectric in a FET. Films that are too thick lower the effective dielectric constant of the high κ / passivation layer film stack. To preserve the equivalent oxide thickness the physical thickness of this gate oxide stack must then decrease, which makes it more susceptible to leakage.

The second requirement is that the passivating layer should form a clean, abrupt interface with Ge. A poor interface where the passivating film intermixes with the Ge surface will result in mechanical or electrical defects. Beyond not intermixing with the Ge, the passivation layer should also form an interface with Ge in which the crystalline lattice structure of bulk Ge is preserved at the passivation layer interface. Otherwise, interface states can result from a distortion of the Ge surface bonds, which will cause increased carrier scattering and reduce device performance [5]. Furthermore, a passivation layer should be chemically stable, resistant to oxidation, electrically insulating, and not change with time.

This study explores the ability of boron carbo-nitride (BC_xN_y, henceforth referred to as BCN for simplicity) to form a continuous coating and a clean interface with Ge(100), two criteria that are essential for passivation of Ge(100) surfaces. This study also investigates the minimum continuous film thickness and interfacial chemistry of BCN films deposited on Si(100) in addition to Ge(100). Significant attention has been given to B–C–N ternary compounds grown by a variety of techniques. The wide range of growth conditions studied thus far has resulted in a material class with vastly tunable properties, including microstructure, crystallinity, hardness, and dielectric constant [6-15].

Several studies involving BCN suggest its use as a passivating film is promising. For example, BCN is reported to form a smooth interfacial layer when deposited on Si(100), a substrate chemically similar to Ge(100) [13]. In passivation efforts,

controlling the chemistry and thickness of the interface that BCN forms with Ge will be essential in minimizing the number of interface states and preserving the electrical integrity of the Ge surface. Therefore a thin, smooth interface is desirable. The ability of B, C, and N to bond with Ge makes such an interface achievable without introducing excessive interface traps. Another report indicates that a SiCBN film is resistant to oxidation [16]. Such oxidation resistance is necessary to prevent the formation of unstable GeO_x. The promising electrical characteristics of BCN on semiconducting substrates are evident in a report that claims interface state densities as low as 1.1×10^{11} $eV^{-1}cm^{-2}$ for S-doped BCN films deposited on GaAs [17]. Further evidence that BCN will behave well electrically comes from previous work in our laboratories, which showed that 50 nm $BC_{0.90}N_{0.08}$, of similar stoichiometry to the films in this study, exhibit low leakage current [8].

The minimum thickness of BCN that results in a continuous film was determined using ion scattering spectroscopy (ISS) and angle resolved x-ray photoelectron spectroscopy (ARXPS), two surface sensitive compositional analysis techniques. In ISS, He^+ ions are scattered from the sample surface, and the kinetic energy loss due to inelastic collisions with surface atoms is measured. Because of the low energy of the He^+ ions (0.5–1.0 kV in this study), scattering should only occur from collisions with atoms on the topmost surface [18]. Upon complete substrate coverage the He^+ ions scatter from only the B, C, and N elements; and the signal from the underlying Ge(100) is completely attenuated.

BCN film continuity was also assessed using ARXPS, a non-destructive technique in which the film composition is profiled at different sampling depths by changing the angle at which photoelectrons are detected. Two methods of estimating overlayer thickness by ARXPS were employed. The first, referred to as conventional

ARXPS in this chapter, assumes uniform coverage of a BCN overlayer on Ge(100) and is commonly used in the literature [19-22]. The second method, referred to as fractional coverage ARXPS in this chapter, is adopted from a model by Mack *et al.* in which the overlayer is assumed to cover some fraction, *f*, of the substrate with rectangular islands [23]. Both techniques involve modification of the Beer-Lambert law to estimate the signal intensity of the species of interest. The ratio of the BCN overlayer thickness estimated by the two ARXPS techniques provides insight into the continuous nature of the film.

2.2. EXPERIMENTAL DETAILS

BCN films were grown on 2.2 × 2.2 cm substrates cleaved from larger wafers of either Ge(100) or Si(100). Prior to film growth, each underwent a preclean step to remove adventitious carbon (Si(100)) and the native oxide layer (Ge(100) and Si(100)). Ge(100) samples were etched for 10 min in 36% HCl solution followed by a 5 s de-ionized (DI) water rinse. Si(100) samples were sequentially rinsed for 30 s each with acetone, ethanol, and DI water; etched for 20 min in Piranna solution (H_2SO_4 : H_2O_2 : H_2O = 6:2:1); etched for 1 min in 2% HF solution; and rinsed for 5 s in DI water. HCl was chosen instead of HF to remove GeO_x because of reports that an HCl-treated Ge surface is stable in ambient longer than an HF-treated Ge surface [2,24]. After cleaning, each sample was dried with He and immediately (< 5 min ambient exposure time) loaded into vacuum for film growth and analysis. Measurements of surface roughness of cleaned Ge(100) and Si(100) substrates were taken with a Digital Instruments Dimension 3100^{TM} atomic force microscope (AFM) using noncontact mode over a 1 μm × 1 μm area at 1 Hz scan rate.

All *in situ* experiments were conducted in a system consisting of a vacuum load lock, sample transfer system, CVD growth chamber, and analysis chamber equipped with XPS and ISS capabilities. All BCN films were grown by thermal CVD using a commercially available solid dimethylamine borane [$NH(CH_3)_2$: BH_3] (DMAB) precursor complex with a melting point of 36 °C. DMAB was kept at 41°C in a stainless steel vessel through which 10 standard cm^3 / min (sccm) Ar was bubbled to deliver the precursor to the CVD showerhead. The vapor pressure of DMAB is 290 mTorr at 41 °C. C_2H_4 coreactant gas was also delivered to the CVD showerhead at 0.8 sccm. After loading the sample into the vacuum load lock and transferring to the analysis chamber, predeposition XPS and ISS scans were taken. The sample was then transferred to the CVD chamber and preheated at 350 °C at 1×10^{-7} Torr for 30 min. The DMAB / Ar and C_2H_4 coreactants were then admitted to the chamber, and the chamber was maintained at 1 Torr throughout the growth period. The sample was cooled for 15 min to 150 °C under 10 sccm Ar at 1 Torr and then further cooled under vacuum at 1×10^{-7} Torr before transferring to the analysis chamber for post-deposition XPS and ISS analysis.

In situ sample analysis was done in a chamber consisting of an XPS / ISS system and an ion gun for Ar^+ sputtering and He^+ ISS. The analysis chamber was kept at a base pressure of 1×10^{-8} Torr. XPS measurements were taken before and after BCN deposition using a Physical Electronics 5500^{TM} XPS system with an Al anode and a 56.7 eV pass energy. A rotatable sample stage allowed for ARXPS measurements, which were taken before and after deposition at photoelectron takeoff angles of 20º–90º relative to the sample surface. The film composition was calculated using sensitivity factors for incident x-rays at 54.7º to the analyzer [25]. Films of $BC_{0.75}N_{0.07}$ and $BCN_{0.07}$ stoichiometry were deposited on Ge(100) and Si(100) substrates, respectively. BCN film thicknesses on Ge(100) and Si(100) were determined by XPS peak attenuation using

effective attenuation lengths (λ) calculated from the TPP-2M equation within the NIST Electron Effective Attenuation Length Database [26]. For a Ge 3*d* and Si 2*p* photoelectron traveling through a BCN overlayer, the calculated values were $\lambda_{Ge,BCN}$ = 3.41 nm and $\lambda_{Si,BCN}$ = 3.24 nm, respectively. PeakFit™ software was used to deconvolute the XP spectra for each element into the individual bonding states. The peaks were fit using a Gaussian-Lorentzian sum function. The full width half maximums (FWHM) of the peaks were fixed using the following reference samples to calibrate: PVD TaC_x for C 1*s* (1.8 eV), BN for B 1*s* (2.1 eV) and N 1*s* (1.8 eV), Si(100) for Si 2*p* (1.5 eV), and Ge(100) for Ge 3*d* (1.6 eV) [15].

ISS measurements were taken before and after deposition with 0.5 and 1.0 kV He^+ ions using an ion gun operating at 25 mA and 2.5 mPa (0.5 kV He^+) or 5 mPa (1.0 kV He^+). The same hemispherical analyzer used for XPS was used for ISS, operating at 375.7 eV pass energy. Post-BCN ISS scans were purposely taken in a different region of the sample than the pre-BCN ISS scan to avoid scanning an area that may have been changed by the incident He^+ ions.

2.3. RESULTS AND DISCUSSION

2.3.1. Film Continuity

2.3.1.1. Ion Scattering Spectroscopy

Figure 2.1(a) is a representative ISS scan showing the attenuation of the Ge(100) signal at $E/E_o \approx 0.95$ after two discontinuous BCN depositions. The close overlap of two IS spectra taken at different points on a control Ge(100) surface that has been etched with HCl indicates the reproducibility in the measured substrate signal intensity. Also note the higher intensity at low E/E_o values for the 1.5 nm BCN film relative to the 0.4 nm BCN

film. The low atomic number B, C, and N elements result in a more inelastic He^+ collision, and thus a lower E/E_o value, than collisions with the heavier Ge substrate atoms. Therefore the higher coverage 1.5 nm BCN film has a higher measured ISS intensity at the low E/E_o values. However, the substrate coverage is not complete at this BCN thickness, so a small Ge(100) signal remains. Upon complete substrate coverage the low energy He^+ ions should inelastically scatter from only BCN elements at lower E/E_o values and not from the underlying Ge atoms. Unfortunately, this ISS instrument was unable to separate the signal contributions from the individual BCN elements due to their close proximity in atomic weight.

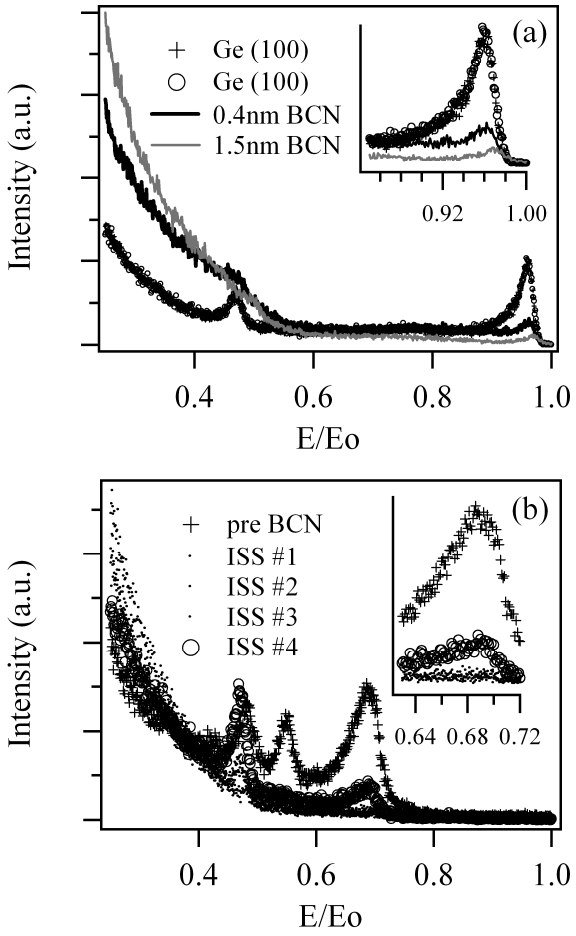

Figure 2.1. (a) Representative pre- and post-BCN ISS scans for BCN on Ge(100). The remaining Ge substrate signal at $E/E_o = 0.95$ suggests a discontinuous film. (b) IS spectra of 1.9 nm BCN on Si(100) showing re-emergence of Si substrate peak with repeated ISS measurements.

It is possible that the 1.0 kV He^+ ions physically sputter the BCN film to expose the underlying substrate [27]. In this case, the minimum continuous film thickness predicted by ISS would actually be less than was predicted above, because He^+ ion damage would cause a thin, continuous film to appear discontinuous. We suspected such damage may be occurring because when the sample was removed from the analysis chamber there was a visible contrast change at the region on the sample where ISS was performed. Film damage was also evident from repeated ISS scans in the same region. Figure 2.1(b) shows repeated ISS scans of a seemingly continuous 1.9 nm BCN film on Si(100). The sputtering capability of the 1.0 kV He^+ ions is demonstrated by the reappearance of the substrate signal at $E/E_o \approx 0.7$, but it is not visible until the fourth scan. To reduce film damage during sample analysis, ISS experiments were also performed with 0.5 kV He^+ ions.

Figure 2.2(a) shows the minimum thickness of BCN required for continuous coverage of Ge(100), determined by 1 kV and 0.5 kV He^+ ISS. To determine BCN film continuity using 1 kV He^+, the ratio of the post- to pre-BCN Ge(100) substrate signal areas (left axis) was plotted as a function of BCN thickness. With the lower energy 0.5 kV He^+ ions the sputtering is reduced, but the signal intensity also severely decreases. Because of this it was difficult to measure the post-BCN : pre-BCN substrate ratios to determine continuity. Instead the post-BCN substrate intensity was averaged over the expected range of E/E_o values (E/E_o = 0.8–1.0 from Fig. 2.1(a)), and this value was plotted versus BCN thickness (right axis).

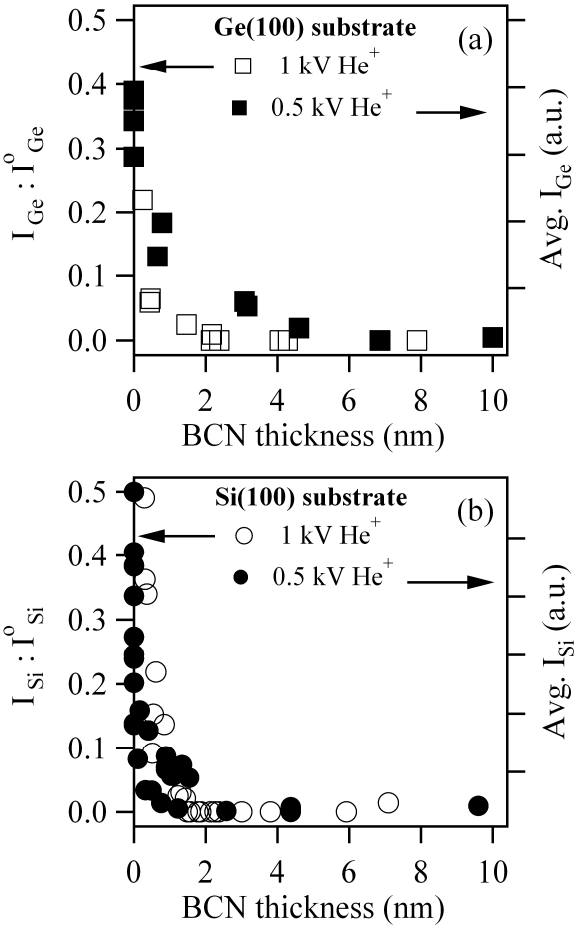

Figure 2.2. BCN film continuity measured from ISS for (a) Ge(100) substrates and (b) Si(100) substrates. BCN is continuous when the ratio of the post- to predeposition substrate signal area ($I_{Substrate} : I^{o}_{Substrate}$) (1 kV He^{+}) or the average substrate signal intensity (0.5 kV He^{+}) approaches 0.

The minimum continuous film thickness from Fig. 2.2(a) appears dependent on the He^{+} ion beam energy used. Measurements with 1 kV He^{+} predict that BCN results in continuous coverage of Ge(100) when the film is ~ 2.5 nm thick. With 0.5 kV He^{+} the minimum continuous thickness is ~ 4–5 nm. The reason the minimum continuous film thickness is higher at 0.5 kV could be because the method of averaging the substrate

signal intensity is more sensitive to subtle changes at low intensities than the method of taking the post-BCN to pre-BCN ratio. If the post-BCN Ge(100) signals from the 1.0 kV ISS scans of Fig. 2.2(a) are averaged in the same way as the 0.5 kV ISS scans, the minimum continuous BCN film thickness appears closer to 4 nm.

Figure 2.2(b) shows the film continuity results from ISS measurements on BCN-covered Si(100) substrates. For Si(100), BCN becomes continuous at 1.5–2 nm with both of the ion beam energies studied.

2.3.1.2. Angle Resolved X-ray Photoelectron Spectroscopy

The second technique to estimate the minimum thickness of BCN necessary for continuous coverage of Ge(100) was ARXPS. As discussed in the Introduction, the BCN overlayer thickness can be estimated two ways by ARXPS. The first is conventional ARXPS, in which a uniform, continuous BCN overlayer is assumed. Modification of the Beer-Lambert law for a BCN overlayer of thickness d on Ge(100) leads to

$$\ln\left(1+\frac{R}{R^{\infty}}\right)=\frac{d}{\lambda_{B,BCN}}\frac{1}{\sin\theta} \qquad (2.1)$$

where R is the ratio of the B 1s and Ge 3d signal intensities; R^{∞} is the ratio of the same intensities from a thick BCN layer and a Ge(100) substrate, respectively; θ is the photoelectron takeoff angle relative to the sample surface; and $\lambda_{B,BCN}$ is the electron effective attenuation length calculated for a B 1s photoelectron traveling through a BCN overlayer (calculated as 3.07 nm) [19,21]. Measuring the B 1s and Ge 3d signals for several takeoff angles and plotting the left-hand side of Eqn. (2.1) versus 1 / sinθ allows one to extract the BCN film thickness, d, from the slope. Figure 2.3 shows the thicknesses calculated from this conventional ARXPS technique for a series of BCN

depositions on Ge(100). This technique was also applied to Si(100) substrates, for which $\lambda_{Si,BCN}$, the estimated attenuation length of a Si 2*p* photoelectron traveling through BCN, was 3.24 nm.

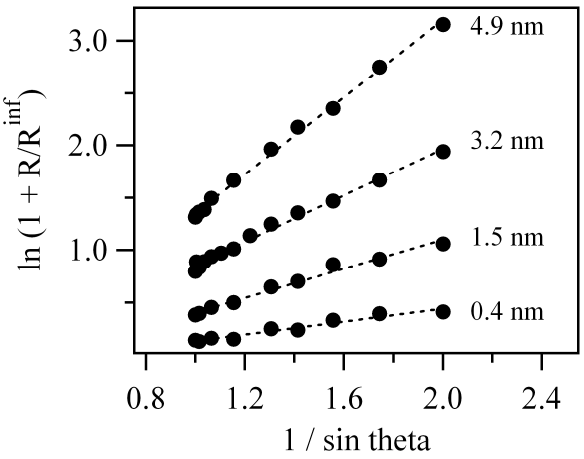

Figure 2.3. Conventional ARXPS thickness estimates for four different BCN films deposited on Ge(100).

The second ARXPS method to estimate BCN thickness is fractional coverage ARXPS, in which the possibility of discontinuous coverage is accounted for. Illustration 2.1 shows the schematic used to model the fractional coverage, *f*, of a BCN film of thickness *d* on Ge(100). For the BCN / Ge(100) system, the equations in the model developed by Mack *et al.* were modified slightly to provide I_B and I_{Ge}, the theoretical B 1*s* and Ge 3*d* signal intensities, respectively [23]. The theoretical $I_B : I_{Ge}$ ratios for a BCN film of thickness *d* and fractional coverage *f* were plotted for a range of takeoff angles. Comparing these curves to the experimentally determined $I_B : I_{Ge}$ ratios collected for a range of takeoff angles allows one to assess film continuity, as well as estimate the

BCN thickness. Figure 2.4 shows three representative cases for BCN deposited on Ge(100). The experimental $I_B : I_{Ge}$ ratios were plotted on the backdrop of the theoretical curves, which were plotted for guessed values of f and d. A least squares regression analysis was then performed to find the values for d and f that result in the smallest difference between the experimental and theoretical ratios. This optimized value of d is the BCN overlayer thickness estimated by fractional coverage ARXPS and is the thickness listed in Fig. 2.4.

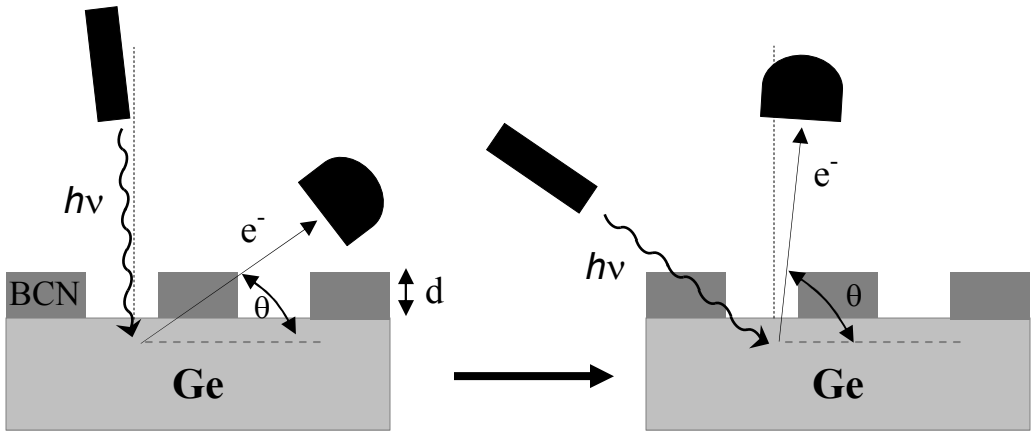

Illustration 2.1. ARXPS model to estimate fractional coverage, f, and thickness, d, of a BCN film deposited on Ge(100).

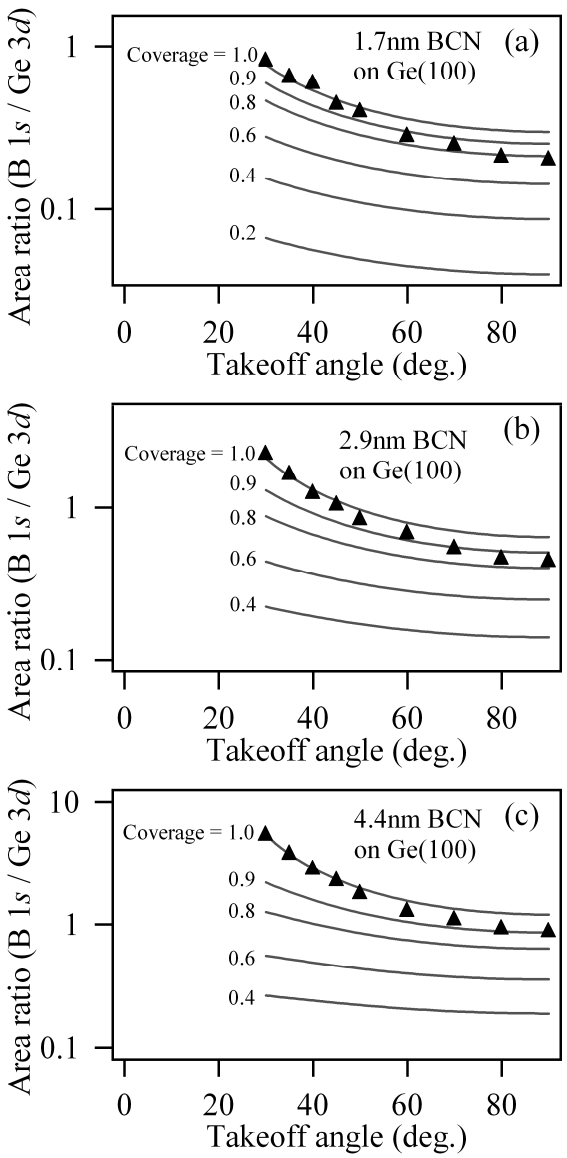

Figure 2.4. ARXPS plots of $I_B : I_{Ge}$ ratios of (a) 1.7 nm, (b) 2.9 nm, and (c) 4.4 nm BCN deposited on Ge(100) over a range of photoelectron takeoff angles. The background curves display theoretical $I_B : I_{Ge}$ ratios for several fractional coverages of BCN. The thickness is estimated by a least squares regression analysis of the theoretical and experimental $I_B : I_{Ge}$ ratios.

With our system it is difficult to use this fractional coverage model by itself to determine the exact point at which BCN becomes discontinuous. This is because there is a tendency for the experimental $I_B : I_{Ge}$ ratios to deviate from the $f = 1.0$ theoretical curve at higher takeoff angles, while the lower takeoff angles seem to predict 100% substrate coverage. This is seen in Fig. 2.4. This deviation at high takeoff angles can possibly be explained by BCN surface roughness. If the BCN layer is continuous but not perfectly smooth, then there will be regions where the thickness is less than the measured thickness. Ge 3*d* photoelectrons emitted at close to normal takeoff angles in these regions of thinner BCN will be attenuated less than in the regions of thicker BCN. This will cause the measured I_{Ge} value to be greater than expected. Likewise the I_B signal from thinner BCN regions will be less than predicted. The net effect of this varying thickness overlayer will be to decrease the $I_B : I_{Ge}$ ratio at high takeoff angles, making the film appear discontinuous when it is actually continuous. At shallow takeoff angles the influence of a rough BCN film on the $I_B : I_{Ge}$ ratio is less pronounced because the majority of emitted photoelectrons will travel a path through both thin and thick sections of a continuous BCN overlayer. This could explain why the experimental $I_B : I_{Ge}$ ratios dip below 100% coverage at the higher takeoff angles.

To use the two discussed ARXPS techniques in conjunction with one another to determine film continuity, the ratio of the thickness estimated by each ARXPS technique is plotted as a function of BCN thickness measured by XPS peak attenuation. When the fractional coverage ARXPS model predicts a continuous film ($f = 1$), the thickness should be the same as that calculated by conventional ARXPS, and the ratio should be unity. As the film becomes discontinuous at lower deposition times, the two techniques should estimate different thicknesses, and the ratio will stray from unity. This method was used

by Mack *et al.* to assess the continuity of an atomic layer deposition (ALD) Al_2O_3 film on SiO_2 [23].

Figure 2.5(a) shows this ratio plotted as a function of BCN XPS peak attenuation thickness. At approximately 3–4 nm, the curve approaches unity and the BCN is considered continuous. The ISS experiments predicted a minimum continuous film thickness of 2.5–5 nm for Ge(100) substrates, depending on the He^+ ion beam energy used. So the 0.5 kV ISS and ARXPS techniques for determining film continuity are in close agreement.

For comparison, Fig. 2.5(b) shows the ratio of the ARXPS thickness estimates for BCN grown on Si(100) substrates. BCN becomes continuous on Si(100) at ~ 2 nm according to this figure. This is also in close agreement with the 1.5–2 nm minimum continuous film thickness predicted by ISS.

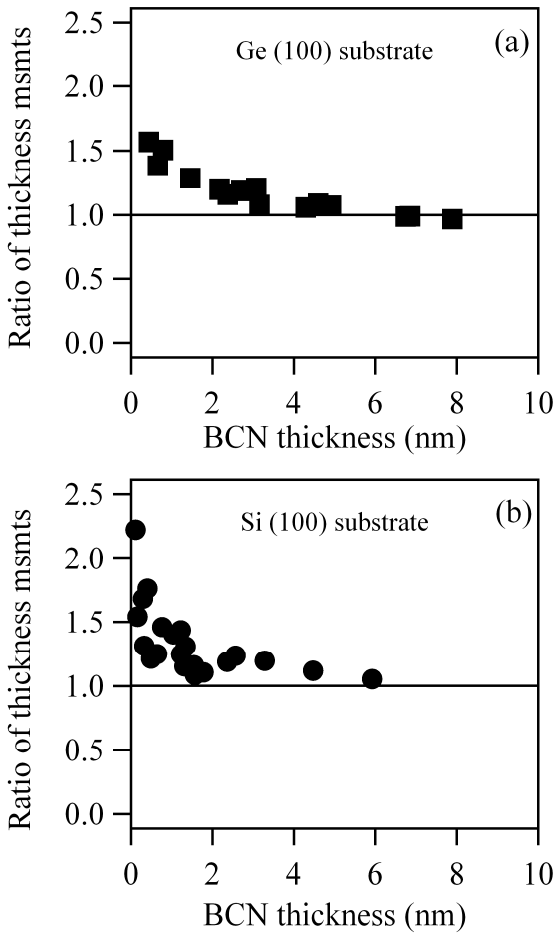

Figure 2.5. Ratio of thickness measurements estimated by conventional ARXPS and fractional coverage ARXPS for BCN deposited on (a) Ge(100) and (b) Si(100) substrates. The ratio is plotted vs. the XPS peak attenuation thickness. The BCN coverage is continuous when the ratio deviates from unity.

The reason for the larger minimum continuous film thickness on Ge(100) is not entirely clear. One possibility is that BCN does not nucleate on Ge(100) as well as it does on Si(100). This would result in more three dimensional growth as the BCN prefers to grow on already-nucleated BCN, whereas BCN may grow in a more two dimensional manner on Si(100). The difference in minimum continuous film thickness does not appear to be due to a difference in roughness between the starting Ge(100) and Si(100) substrates. AFM measurements of both control substrates reveal an RMS roughness of ~ 0.3 nm.

Knowing the nominal thickness of BCN required for continuous coverage of Ge(100) motivates the thickness that should be used in future studies of BCN as a passivation layer. From ISS and ARXPS we know with certainty that BCN thinner than 2.5 nm will leave portions of the underlying Ge(100) substrate exposed. During the fabrication of Ge electronic devices, these uncoated regions will be sites where surface states can develop and where formation of the unstable GeO_x can occur. Films that are nominally 2.5–5 nm thick appear to be on the threshold of being continuous. To ensure that a BCN overlayer will completely coat Ge(100), a film at least 5 nm thick should be used in future passivation studies.

2.3.2. Interface Bonding

2.3.2.1. BCN on Ge(100)

HCl etching of Ge(100) results in a Cl-covered surface, as is evident in Fig. 2.6. To determine whether this Cl plays a role in the bonding at the BCN–Ge(100) interface, we tested the stability of this Cl layer under typical BCN deposition conditions. To do this, an HCl-etched Ge(100) sample was annealed at 350 ºC for 30 min, the same thermal

treatment endured during the preheat step of BCN deposition. XPS following this anneal reveals an attenuated signal around 199 eV. However, etching Ge(100) for 1 min in a 2% HF solution reveals the same signal. Therefore this peak is not attributed to Cl 2*p*, but rather to a bulk plasmon line associated with the Ge 3*s* orbital. Such energy loss lines are known to be present in metals and semiconductors due to a shielding of emitted photoelectrons by group oscillations of conduction electrons. The plasmon signals typically show up at binding energies 20–25 eV higher than the parent line [25]. This is consistent with the expected bulk plasmon line from a Ge 3*s* photoelectron, which has a binding energy of 181 eV. To further support this assignment, the 199 eV signal attenuates in a 30º takeoff XPS scan (not shown). If the signal were from Cl 2*p*, we would expect the signal to increase due to the enhanced surface sensitivity of the shallow takeoff angle scan. However if the signal is from a bulk plasmon, the signal should attenuate at the shallower takeoff angle, as was observed.

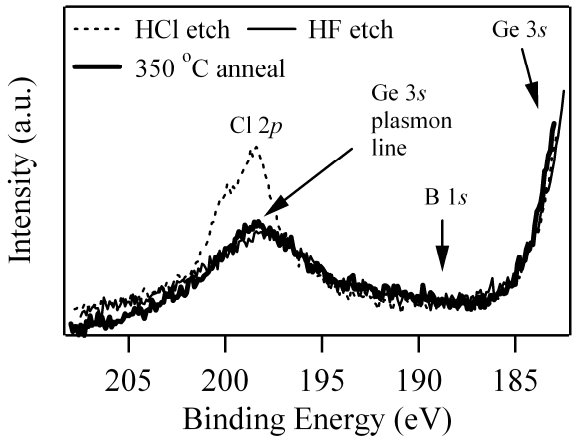

Figure 2.6. XP spectra of B 1*s*, Cl 2*p*, and Ge 3*s* regions of HF-treated Ge(100) and of HCl-treated Ge(100) surface after etch and after 350 ºC, 30 min anneal in CVD chamber.

The disappearance of Cl following the 350 ºC anneal is consistent with Cl and Ge interactions studied by temperature programmed desorption (TPD) [28]. HCl and $GeCl_2$ are reported to desorb from Ge(100) surfaces at ~ 300ºC and 400 ºC, respectively. But the $GeCl_2$ desorption process actually begins around 350 ºC. During the 350 ºC preheat step, we therefore expect $GeCl_2$ as well as any adsorbed HCl to desorb, leaving a clean Ge(100) surface. When BCN reactant gases are introduced, there is no remaining Cl available to participate in interface bonding.

To study the bonding that occurs at the Ge(100) interface, a discontinuous 1.5 nm BCN film was studied first. As a thicker overlayer of BCN is deposited, contributions to the XPS signal intensities from B, C, and N interactions with Ge(100) are overshadowed by bonding interactions within the bulk BCN film. Therefore a discontinuous film was chosen to maximize the XPS signal intensities at the substrate interface. The N 1*s* signal is not shown because of the small amount of N (< 5 at. %) in all the films studied. The C 1*s* signal in Fig. 2.7(a) shows that most of the C at the interface occupies either the C–C or C–B bonding states. There is a lesser amount of C–N bonding, which is to be expected from the small amount of N in the films. The B 1*s* signal in Fig. 2.7(b) reveals that B–C bonding dominates the B–B and B–N contributions. To our knowledge, the binding energy of C–Ge and B–Ge bonding in the C 1*s* and B 1*s* orbitals, respectively, has not been reported. However, C–Si and B–Si bonding has been reported at 283.5 eV and 188.3 eV, respectively [29,30]. Based on the similarities between Ge and Si, it is reasonable to assume similar binding energies would be witnessed for C–Ge and B–Ge. If this is the case then any C interaction with the Ge(100) substrate could easily be lost in the C–B contribution to the C 1*s* signal. Likewise, B interaction with Ge(100) could be lost in B–B contribution to the B 1*s* signal. Interfacial bonding with the substrate

becomes even more difficult to detect if the interface is abrupt, and there is no interfacial layer.

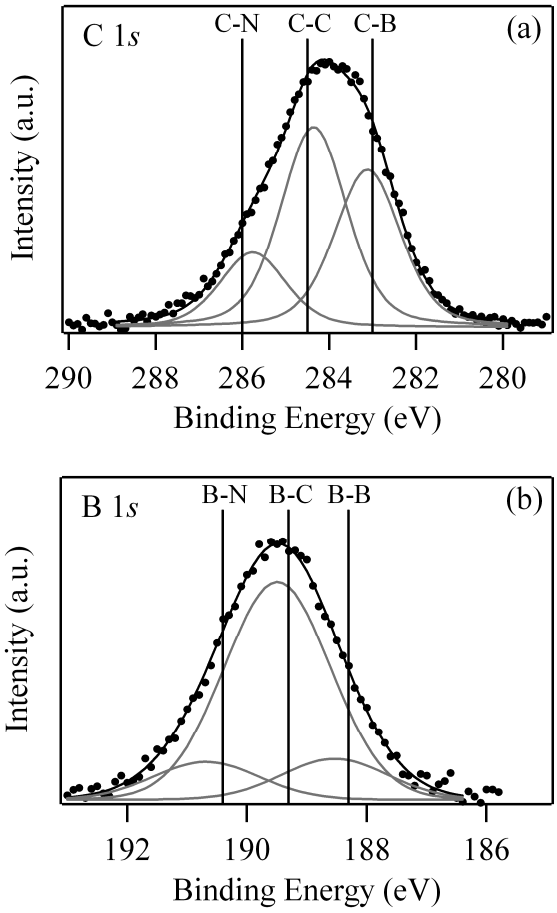

Figure 2.7. XP spectra of (a) C 1*s* and (b) B 1*s* regions of discontinuous 1.5 nm BCN on Ge(100).

To help highlight this interface, ARXPS was used to look at changes to the Ge signal's full-width-half-maximum (FWHM), shown in Fig. 2.8. Increases in the FWHM following film deposition would be indicative of additional bonding features involving the Ge atom, other than the Ge–Ge bonding found in the bulk [31-33]. Figure 2.8(a) shows the changes in the Ge 3*d* FWHM of an HCl-etched Ge(100) control sample following annealing for 30 min at 350 ºC and deposition of BCN. There is actually a slight decrease in the FWHM upon annealing. This is consistent with the desorption of HCl and $GeCl_2$ discussed above. The Ge 3*d* FWHM values plotted for BCN on Ge(100) in Fig. 2.8(a) are the average values measured for several BCN films ranging from 0.4–3.2 nm. Upon deposition of BCN, there is virtually no change in the FWHM of an annealed Ge(100) sample. Both the annealed Ge(100) and BCN-coated Ge(100) have lower Ge 3*d* FWHM values than the Cl-covered Ge(100) control surface. This implies that the Ge–Ge bonding found in the bulk crystal is better preserved when passivated with BCN than with Cl. This is further confirmed by the more drastic differences in the Ge 2*p* signal FWHM seen in Fig. 2.8(b). The Ge 2*p* FWHM values of annealed and BCN-coated Ge(100) are 0.2–0.3 eV less than the HCl-etched Ge(100). Since photoelectrons emitted from the Ge 2*p* orbital have a much lower kinetic energy than photoelectrons emitted from the Ge 3*d* orbital, the Ge 2*p* signal is more surface sensitive. Therefore bonding at the Ge(100) surface relative to Ge(100) bulk bonding is more easily seen with the Ge 2*p* XPS signal than the Ge 3*d* signal. The larger Ge 2*p* FWHM values of the Cl-covered sample therefore suggest there is a significant difference in the preservation of bonding at the interface by Cl compared to BCN. Since the FWHM values of the BCN on Ge(100) sample are close to the Cl-free annealed Ge(100) sample, the bulk Ge(100) bonding is better preserved by BCN. Another notable feature of Fig. 2.8(b) is that the slope of the FWHM versus takeoff angle is closer to zero for the BCN

sample than the HCl-treated control sample. The fact that the FWHM of the control sample increases with decreasing takeoff angle further confirms that the bonding of Ge at or close to the surface is different than the bulk Ge sampled at high takeoff angles. This is due to the Ge–Cl interaction from the Cl-covered surface (seen in Fig. 2.6). The lack of such an increase in the FWHM of the BCN-coated sample indicates that the BCN forms a clean, abrupt interface with Ge(100).

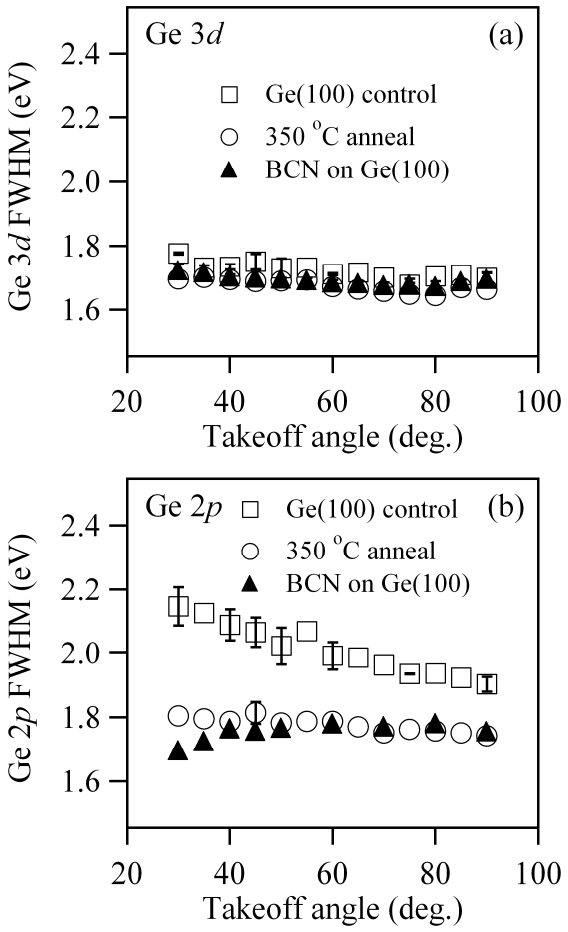

Figure 2.8. FWHM of (a) Ge 3*d* and (b) Ge 2*p* XP spectra at various takeoff angles for control Ge(100) surface following HCl etch, HCl etch and 350 ºC anneal, and HCl etch and discontinuous BCN deposition.

ARXPS was employed to look at a thicker 7.6 nm BCN film to compare how B, C, and N bonding at the Ge(100) interface compares with bonding in the bulk of the BCN film (Fig. 2.9). Again the N 1*s* signal is not shown because the nitrogen incorporation is less than 5 at. %. The C 1*s* and B 1*s* signal contributions are in close agreement with the signals from the thinner film in Fig. 2.7, suggesting the interface bonding matches the bulk film bonding. As the takeoff angle decreases the sampling depth becomes shallower, as is evident by the gradual attenuation of the Ge 3*d* substrate signal in Fig. 2.9(c). Between 60º and 20º the Ge 3*d* signal disappears completely. If a BCN–Ge interfacial layer exists, or the B and C bonding at the Ge(100) interface is different than in bulk BCN, there should be a notable change in the C 1*s* and B 1*s* spectra between 60º and 20º. The interface is included in the spectra at 60º and excluded at 20º. However, the C 1*s* and B 1*s* signals are consistent over the range of takeoff angles studied. This is further evidence that BCN forms a clean interface with no intermixing at the Ge(100) surface.

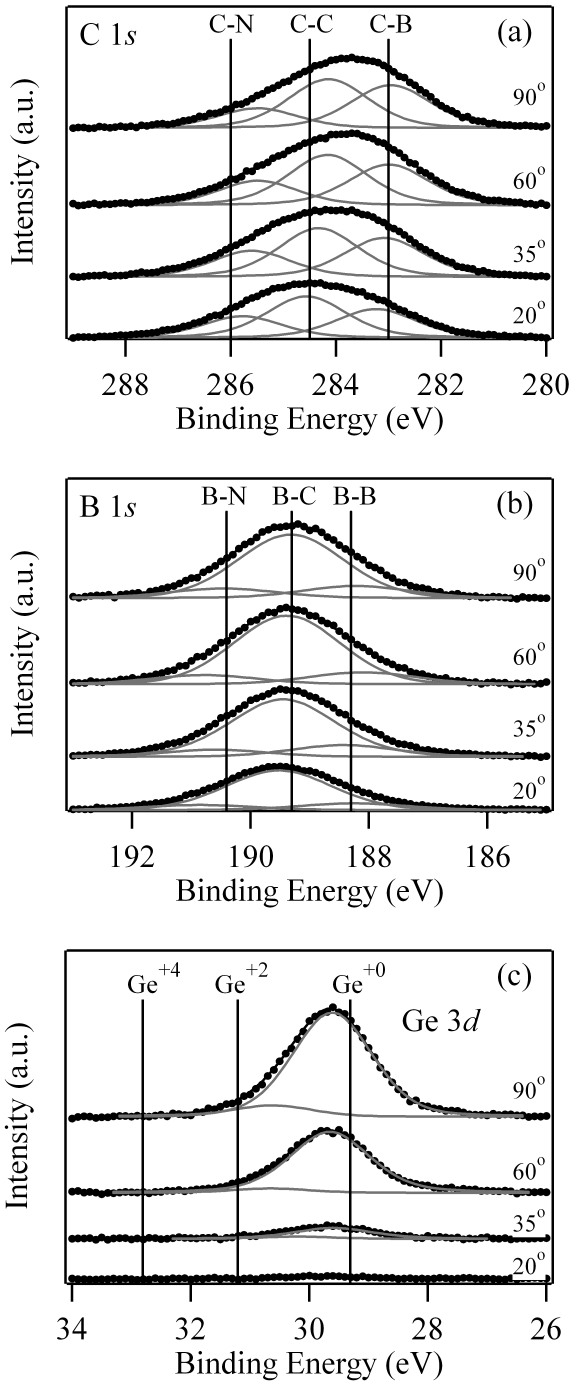

Figure 2.9. ARXP spectra of (a) C 1*s*, (b) B 1*s*, and (c) Ge 3*d* regions of continuous 7.6 nm BCN on Ge(100).

Figure 2.10 shows the depth profile from this ARXPS experiment. The depth profile was obtained for a series of ARXPS scans, with the shallowest angles detecting only the elements in the topmost portion of BCN and the higher angles probing down to the substrate interface. There is a greater amount of C detected on the surface than in the film bulk. This is to be expected because transfer of the sample from the CVD chamber to the analysis chamber via the vacuum load lock chamber likely leads to adventitious C on the topmost BCN surface. Importantly, the atomic percents from 45º to 90º are fairly constant; this suggests that aside from the C-contaminated surface layer, the BCN composition is uniform throughout the bulk.

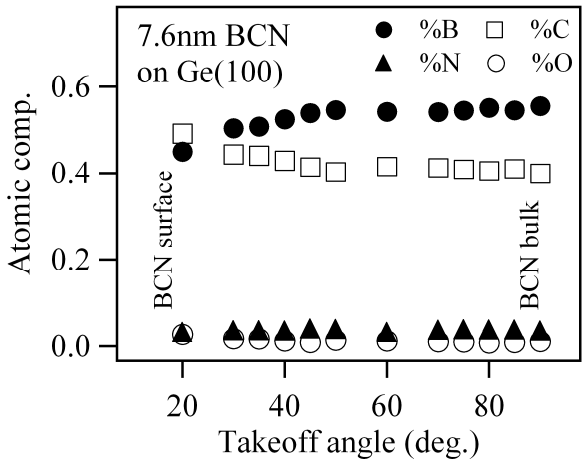

Figure 2.10. ARXPS depth profile showing BCN composition difference between top surface and bulk for 7.6 nm BCN on Ge(100). The contribution from the Ge 3*d* substrate signal was neglected in the calculation of atomic composition.

2.3.2.2. BCN on Si(100)

BCN interface formation with Si(100) substrates were also studied. The deconvoluted XP spectra of 1.6 nm BCN grown on Si(100) (not shown) were much like the C 1*s* and B 1*s* spectra of the 1.5 nm BCN film on Ge(100) in Fig. 2.7. The Si 2*p* region in Fig. 2.11 shows that C–Si bonding likely plays a significant role in the initiation of BCN film growth on Si(100) substrates. It is also possible that B–Si bonding occurs. The Si–B feature referenced at 101.9 eV is actually for B_4Si [30]. Though no reports were found in literature, it is likely that lower B:Si stoichiometric ratios will result in less of a binding energy shift for Si 2*p* photoelectrons. If BCN forms a clean interface with Si(100), then such lower B:Si ratios are likely, and the contribution to the Si 2*p* signal will be shared with the Si-C bonding attribute.

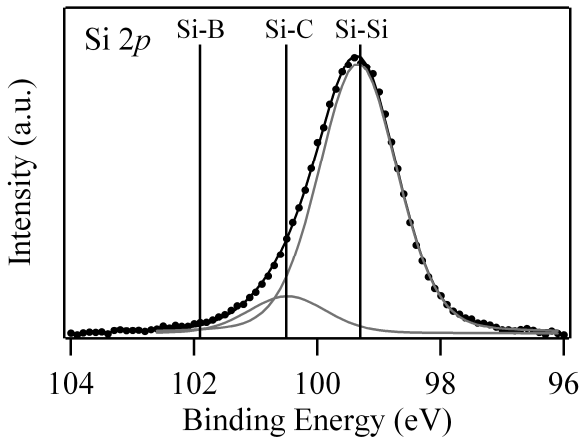

Figure 2.11. Si 2*p* XP spectrum of 1.6 nm BCN on Si(100).

ARXPS was also used to study the change in the FWHM of the Si 2*p* signal following BCN deposition (not shown). For Si(100) substrates there was virtually no change in the Si 2*p* FWHM for the HF-treated, 350 ºC annealed, and BCN-coated substrates. Like the Ge(100) substrate, this indicates that the bonding features in the crystalline bulk of Si(100) are preserved at the interface with BCN.

ARXPS is employed in Fig. 2.12 to look at a thicker, 5.9 nm continuous BCN film to determine how bonding at the Si(100) interface compares to bonding in the bulk BCN. Figure 2.12(c) shows that the contribution from the substrate Si 2*p* signal is lost as the takeoff angle becomes shallower. Any interface bonding features should also be lost at the shallow angles. But there is virtually no change in the C 1*s* and B 1*s* signals over the entire range of angles. This reveals that the bonding in the bulk is preserved at the Si(100) interface. The lack of an additional XPS feature at the larger takeoff angles suggests that there is no intermixing of B, C, and N with the Si(100) surface. It also suggests there is no preferential accumulation of any particular element at the interface, and the film composition is uniform throughout. There appears to be a clean, abrupt interface, which is vital if BCN is to successfully passivate semiconductor surfaces.

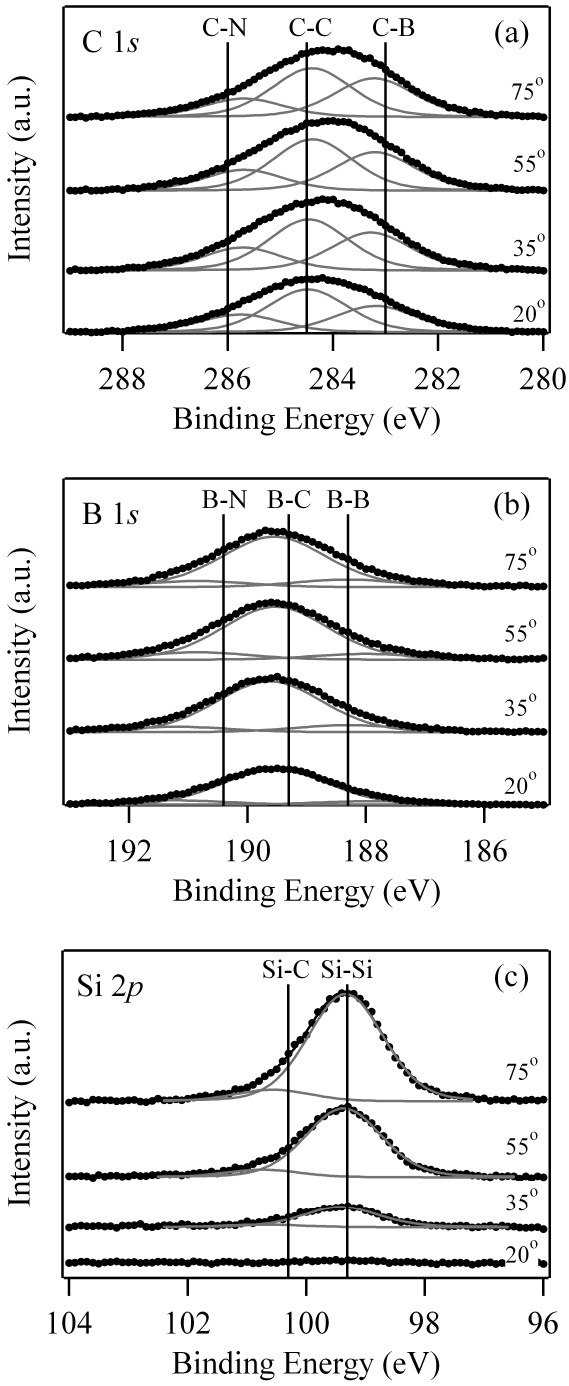

Figure 2.12. ARXP spectra of (a) C 1*s*, (b) B 1*s*, and (c) Si 2*p* regions of continuous 5.9 nm BCN on Si(100).

Figure 2.13 shows how the BCN atomic composition changes with depth for Si(100) substrates, as measured by ARXPS. As was the case for the Ge(100) substrate, there is a greater amount of C detected on the surface than in the film bulk due to sample transfer through the vacuum load lock. But aside from this C-contaminated surface layer, the BCN composition is uniform throughout the bulk. The contribution from the Si 2*p* signal was neglected in the calculation of atomic composition. One notable difference between the Ge(100) and Si(100) substrates was the BCN film stoichiometry. Films grown on Si(100) were $BCN_{0.07}$ stoichiometry, whereas growth on Ge(100) resulted in $BC_{0.75}N_{0.07}$ films. The higher B:C ratio on the Ge(100) is attributed to differences in the temperature of Ge(100) substrates compared to Si(100) during typical BCN deposition conditions. An investigation into the growth rate of BCN on the two substrates supports this hypothesis.

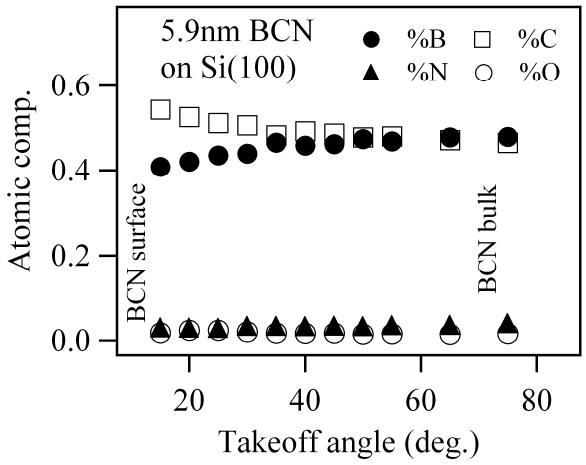

Figure 2.13. ARXPS depth profile showing BCN composition difference between top surface and bulk for 5.9 nm BCN on Si(100). The contribution from the Si 2*p* substrate signal was neglected in the calculation of atomic composition.

2.3.2.3. BCN growth rate

Figure 2.14 shows the difference in BCN growth rate observed for the Ge(100) and Si(100) surfaces. BCN deposited on Si(100) proceeds at a rate of ~ 0.2 nm/min. However, BCN deposits on Ge(100) at nearly 1 nm/min, roughly five times the rate of growth on Si(100). This is suspected to be due to different heating characteristics of the Ge(100) substrates. To determine the substrate temperature under growth conditions, a thermocouple glued to the surface of a Si(100) substrate is calibrated to a reference thermocouple in the CVD chamber. This allows estimation of the surface temperature of Si(100) during film growth. This calibration is most likely different for Ge(100). When BCN is grown on Ge(100) at 325 ºC (calibrated surface temperature of Si(100)) both the growth rate and stoichiometry more closely match those of growths on Si(100) at 350 ºC. This suggests that the radiative heating of Ge(100) is more efficient than Si(100), and identical reaction conditions will produce higher surface temperatures on Ge(100) than on Si(100). This higher surface temperature results in faster growth rates and higher B:C stoichiometric ratios.

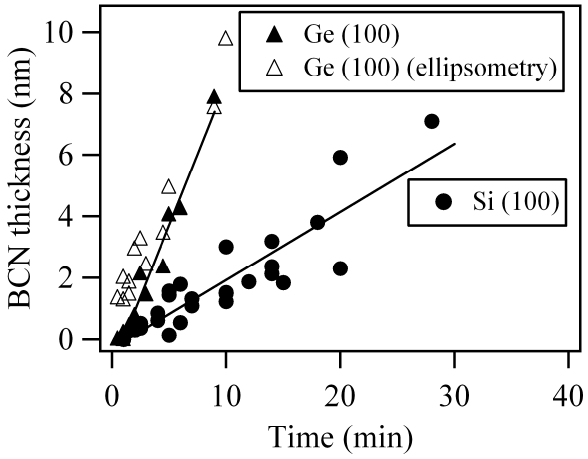

Figure 2.14. BCN deposition rate on Ge(100) and Si(100). All thicknesses were calculated by XPS peak attenuation. BCN thicknesses calculated by spectroscopic ellipsometry on Ge(100) substrates are included for comparison.

2.4. SUMMARY

$BC_{0.75}N_{0.07}$ stoichiometry films were deposited on Ge(100) substrates, and $BCN_{0.07}$ stoichiometry films were deposited on Si(100) substrates. From ISS and ARXPS measurements, it appears the minimum continuous BCN film on Ge(100) is nominally 2.5–5 nm thick, measured by XPS peak attenuation. Future passivation studies involving BCN on Ge(100) should target at least this thickness. Below this thickness range there will be exposed portions of Ge(100), which will be free to oxidize during subsequent electronic device processing steps. On Si(100) substrates the required thickness for continuity determined by ISS and ARXPS is 1.5–2 nm.

ARXPS was also used to study the interface bonding of BCN with Ge(100) and Si(100) surfaces. In each case, BCN appears to create a clean, abrupt interface with the substrate. There is no evidence of intermixing with either substrate to create an interfacial layer. BCN bonding in the bulk matched bonding at the Ge(100) and Si(100) surfaces. Analysis of the FWHM of the Ge 3*d*, Ge 2*p*, and Si 2*p* signals before and after BCN deposition suggests that Ge and Si bonding within their respective bulk crystalline lattices is preserved at the interface with BCN.

For passivation purposes, it is critical that an interfacial layer does not form from intermixing of the BCN passivating elements with the Ge(100). Such an occurrence would create mechanical and electrical defects in the Ge. But an abrupt interface is not enough to ensure passivation. It is also essential that the Ge bonding features in the crystalline bulk are preserved at the interface with BCN. It is possible to have an abrupt interface that still distorts the Ge surface bonds. Such a distortion in bonding would result in interface states, which would reduce charge carrier mobility in an electronic device. The ARXPS analysis in this study shows that the BCN–Ge(100) interface is

abrupt and that the Ge bulk bonding is very well preserved at the BCN interface. Based on these criteria, BCN looks to be a promising passivation layer. These results motivate ongoing work to determine the ability of BCN to resist oxidation of Ge, as well as the electrical characteristics of BCN-passivated Ge devices.

2.5. REFERENCES

[1] S. M. Sze, *Physics of Semiconductor Devices*, Second ed. (John Wiley & Sons, New York, 1981).

[2] P. W. Loscutoff and S. F. Bent, Annu. Rev. Phys. Chem. **57**, 467 (2006).

[3] D. W. Wang, Y. L. Chang, Q. Wang, J. Cao, D. B. Farmer, R. G. Gordon, and H. J. Dai, J. Am. Chem. Soc. **126**, 11602 (2004).

[4] R. H. Kingston, J. Appl. Phys. **27**, 101 (1956).

[5] D. W. Wang, Q. Wang, A. Javey, R. Tu, H. J. Dai, H. Kim, P. C. McIntyre, T. Krishnamohan, and K. C. Saraswat, Appl. Phys. Lett. **83**, 2432 (2003).

[6] W. J. Ahearn, P. R. Fitzpatrick, and J. G. Ekerdt, J. Vac. Sci. Technol. A **25**, 570 (2007).

[7] E. R. Engbrecht, P. R. Fitzpatrick, K. H. Junker, Y. M. Sun, J. M. White, and J. G. Ekerdt, J. Mater. Res. **20**, 2218 (2005).

[8] E. R. Engbrecht, Y. M. Sun, K. H. Junker, J. M. White, and J. G. Ekerdt, J. Vac. Sci. Technol. B **23**, 463 (2005).

[9] T. Sugiyama, T. Tai, and T. Sugino, Appl. Phys. Lett. **80**, 4214 (2002).

[10] Z. J. Zhang, C. Kimura, and T. Sugino, J. Appl. Phys. **98**, 036105 (2005).

[11] M. N. Uddin, M. Shimoyama, Y. Baba, T. Sekiguchi, and M. Nagano, J. Vac. Sci. Technol. A **23**, 497 (2005).

[12] M. Mieno and T. Satoh, J. Mater. Sci. **36**, 3925 (2001).

[13] M. K. Lei, Q. Li, Z. F. Zhou, I. Bello, C. S. Lee, and S. T. Lee, Thin Solid Films **389**, 194 (2001).

[14] Z. F. Zhou, I. Bello, M. K. Lei, K. Y. Li, C. S. Lee, and S. T. Lee, Surf. Coat. Technol. **128-129**, 334 (2000).

[15] E. R. Engbrecht, Y. M. Sun, K. H. Junker, J. M. White, and J. G. Ekerdt, J. Vac. Sci. Technol. A **22**, 2152 (2004).

[16] Q. D. Nghiem and D. P. Kim, J. Mater. Chem. **15**, 2188 (2005).

[17] S. Umeda, T. Yuki, T. Sugiyama, and T. Sugino, Diamond Relat. Mater. **13**, 1135 (2004).

[18] H. H. Brongersma, M. Draxler, M. de Ridder, and P. Bauer, Surface Science Reports **62**, 63 (2007).

[19] M. P. Seah and S. J. Spencer, Surf. Interface Anal. **33**, 640 (2002).

[20] M. P. Seah and R. White, Surf. Interface Anal. **33**, 960 (2002).

[21] R. Champaneria, P. Mack, R. White, and J. Wolstenholme, Surf. Interface Anal. **35**, 1028 (2003).

[22] R. G. Vitchev, J. J. Pireaux, T. Conard, H. Bender, J. Wolstenholme, and C. Defranoux, Appl. Surf. Sci. **235**, 21 (2004).

[23] P. Mack, R. G. White, J. Wolstenholme, and T. Conard, Appl. Surf. Sci. **252**, 8270 (2006).

[24] D. Bodlaki, H. Yamamoto, D. H. Waldeck, and E. Borguet, Surf. Sci. **543**, 63 (2003).

[25] J. F. Moulder, W. F. Stickle, P. E. Sobol, and K. D. Bomben, *Handbook of X-ray Photoelectron Spectroscopy*. (Physical Electronics, Inc., Eden Prairie, MN, 1995).

[26] C. J. Powell and A. Jablonski, NIST Electron Effective Attenuation Length Database (National Institute of Standards and Technology, Gaithersburg, MD, 2001).

[27] H. H. Brongersma and J. P. Jacobs, Appl. Surf. Sci. **75**, 133 (1994).

[28] S. M. Cohen, T. I. Hukka, Y. L. Yang, and M. P. D'Evelyn, Thin Solid Films **225**, 155 (1993).

[29] C. Guimon, D. Gonbeau, G. Pfisterguillouzo, O. Dugne, A. Guette, R. Naslain, and M. Lahaye, Surf. Interface Anal. **16**, 440 (1990).

[30] L. Chen, T. Goto, T. Hirai, and T. Amano, J. Mater. Sci. Lett. **9**, 997 (1990).

[31] B. P. Swain, Surf. Coat. Technol. **201**, 1589 (2006).

[32] A. Toneva, T. Marinova, and V. Krastev, J. Lumin. **80**, 455 (1998).

[33] I. Kusunoki, T. Takagaki, S. Ishidzuka, Y. Igari, and T. Takaoka, Surf. Sci. **380**, 131 (1997).

Chapter 3: Oxidation Resistance of BC_xN_y on Ge(100) and Ge Nanowires

3.1. INTRODUCTION

Complementary metal-oxide-semiconductor (CMOS) devices incorporating Ge as the channel material have attracted considerable attention in recent years. This is due to the higher intrinsic carrier mobility in Ge compared to Si. Ge nanowires (GeNWs) have also been the focus of substantial research, due to their potential use in various nanoelectronic and photonic devices [1-5]. One major drawback to both single crystal Ge and GeNWs, however, is the unstable native oxide that easily forms on Ge. GeO_2 is both water-soluble and thermally unstable, thus complicating processing of Ge devices. A recent report indicates that despite the solubility of GeO_2 in water, a thin Ge suboxide layer forms when Ge surfaces are treated with water [6]. Furthermore, a high density of surface states makes the Ge–GeO_x interface electrically unstable. The use of Ge in CMOS devices is also complicated by unstable germanide formation upon high-κ oxide deposition. Recent studies have shown that HfO_2 deposition on Ge(100) is especially troublesome due to Hf–Ge bond formation, which produces interface states in the band gap [7,8].

To realize the promising applications of Ge- and GeNW-based devices, the Ge surface must be chemically passivated to remain stable in multiple oxidizing environments. For some Ge(100) and GeNW applications (e.g. chemical sensors), the passivating layer may be the only material between the operating Ge device and the ambient environment. For such a device to be effective the passivating film must preserve the chemical and electrical integrity of the Ge surface for the lifetime of the

device. Other applications of Ge (e.g., CMOS devices) will require the passivating film to protect the Ge during subsequent device processing steps. This will include deposition of a high-κ gate oxide as well as potential exposure to aqueous environments.

Substantial efforts have been made to passivate Ge surfaces by making Ge oxidation resistant. Hydrogen termination by either dry [9-12] (vacuum adsorption of atomic hydrogen) or wet [13-16] treatment is one approach taken. Another approach has been to etch the oxide with HCl, temporarily passivating the Ge in the process through Cl-termination [5,13-15,17,18]. However both of these treatments have shown very limited stability with prolonged ambient exposure. A more promising passivation technique has been by sulfide termination of Ge, which has demonstrated oxidation resistance when exposed to ambient for several days [13,15,19,20]. However, when aqueous sulfidation treatment is applied to GeNWs, one study observed the formation of a 5 nm GeS_x layer, which is undesirable for electronic device applications [13]. A number of studies have investigated organic functionalization by either hydrogermylation reactions, alkanethiol reactions, or Grignard reactions on Cl-terminated Ge surfaces [16,18,21,22]. Ultrathin (<1 nm) Si layers grown on Ge have also demonstrated improved Ge oxidation resistance in addition to improved electrical characteristics [23,24].

This chapter examines the ability of boron carbo-nitride (BC_xN_y, henceforth referred to as BCN for simplicity) grown by chemical vapor deposition (CVD) to passivate Ge(100) and GeNW surfaces by preventing formation of unstable GeO_x. BCN is a non-oxidic ceramic, and its growth should not lead to Ge oxidation. BCN grown in our laboratory has a tunable dielectric constant between 3.7 and 4.6 [25]; the films grown herein are close to $\kappa \approx 3.7$. BCN was the focus of a prior Ge passivation study in our laboratory that explored the BCN–Ge(100) interface properties as well as the minimum

BCN thickness required for continuous coverage of Ge(100) [26]. This study found that BCN forms a clean, abrupt interface with Ge(100) and that Ge bulk bonding features were preserved at the interface with BCN. The minimum thickness of BCN that resulted in continuous coverage of Ge(100) was 2.5–5 nm, measured by X-ray photoelectron spectroscopy (XPS) peak attenuation.

Also motivating the use of BCN as a passivating film are reports that SiCBN films are resistant to oxidation [27], and carbon-rich BCN resists incorporation of water into the film [28]. BCN has also been reported to perform well electrically when deposited on semiconducting substrates. S-doped BCN films deposited on GaAs exhibit interface state densities as low as 1.1×10^{11} $eV^{-1}cm^{-2}$ [29], and 50 nm $BC_{0.90}N_{0.08}$ grown in our laboratory exhibits low leakage current [30].

To study the resistance to Ge oxidation, BCN films of varying thickness were deposited on Ge(100) and GeNWs and exposed to ambient. Periodic XPS measurements were made to track the formation of the various Ge oxidation states with increasing ambient exposure. XPS depth profiles of HfO_2 / BCN / Ge(100) samples were performed to determine how BCN resists Ge oxidation and unstable germanide formation upon exposure to a HfO_2 deposition process. Wet oxidation of BCN-coated Ge(100) samples was studied by treating the samples with 50° C de-ionized (DI) water and looking for the formation of GeO_x. For this test, oxidation resistance of N-rich $BC_{0.25}N_{0.4}$ was compared to C-rich $BC_{0.7}N_{0.08}$. N-rich BCN films may be desirable based on reports of improved electrical performance of nitridated Ge surfaces [31,32]. High resolution transmission electron microscope (HRTEM) images of HfO_2 / BCN / Ge(100) cross sections and BCN-coated GeNWs were also taken for visual inspection of the BCN–Ge interface.

3.2. EXPERIMENTAL DETAILS

Single-side polished Ge(100) wafers (n- and p-type, Waferworld) were cut into 2.2 × 2.2 cm substrates using a dicing saw. To remove the native GeO_2 prior to BCN deposition the samples were etched for 10 min in 36% HCl solution, rinsed for 5 s in DI water, dried with He, and immediately (< 5 min ambient exposure time) placed in a vacuum load lock chamber. Reports that HCl-etched Ge surfaces are stable in ambient longer than HF-treated Ge motivated this cleaning procedure [15].

Single-crystal GeNWs with diameters ranging from 10–50 nm and a predominately [110] growth direction were obtained from a supercritical fluid-liquid-solid (SFLS) synthesis involving diphenylgermane as the Ge precursor. Details of the GeNW synthesis are provided elsewhere [2]. The wires were on a 0.4 cm × 3 cm Si(100) wafer piece that had been placed in the reactor to collect the wires. This piece was cleaved into 0.4 cm × 0.6 cm segments and mounted with Ag paste (Ted Pella, Inc.) to a 2.2 × 2.2 cm Si(100) wafer. Prior to BCN deposition, the native GeO_2 was removed with the same cleaning procedure used for the Ge(100) samples, and the sample was immediately placed in the vacuum load lock.

The system used to conduct all *in situ* experiments consists of a vacuum load lock, sample transfer system, CVD growth chamber for BCN, atomic layer deposition (ALD) chamber for HfO_2, and an XPS analysis chamber with Ar^+ sputter capabilities. BCN films were grown by thermal CVD using a commercially available solid dimethylamine borane [$NH(CH_3)_2 : BH_3$] (DMAB) precursor complex with a melting point of 36 °C. DMAB was kept at 41°C in a stainless steel vessel, and Ar carrier gas was bubbled through at 10 standard cm^3 / min (sccm) to deliver the precursor to the CVD showerhead. The vapor pressure of DMAB is 290 mTorr at 41 °C. Either C_2H_4 or NH_3 coreactant gas was also delivered to the CVD showerhead at 0.8 sccm or 10.0 sccm,

respectively. After removing the native oxide and loading the sample into the vacuum load lock, the sample was transferred to the analysis chamber for a predeposition XPS scan to be taken. The sample was then transferred to the CVD chamber and preheated for 30 min at 350 °C at 1×10^{-7} Torr. The DMAB / Ar and C_2H_4 (or NH_3) coreactants were then admitted to the chamber, and the chamber was maintained at 1 Torr throughout the growth period. The sample was cooled to 150 °C under 10 sccm Ar at 1 Torr for 15 min and then further cooled under vacuum at 1×10^{-7} Torr before transferring to the analysis chamber for post-deposition XPS analysis.

Samples were analyzed *in situ* in a chamber consisting of an XPS system and an ion gun for Ar^+ sputtering. The analysis chamber was kept at a base pressure of 1×10^{-8} Torr. XPS measurements were taken before and after BCN deposition using a Physical Electronics 5500^{TM} XPS system with an Al anode and a 56.7 eV pass energy. BCN film composition was calculated using sensitivity factors for incident X-rays at 54.7º to the analyzer [33]. Films of $BC_{0.7}N_{0.08}$ and $BC_{0.25}N_{0.4}$ stoichiometry were deposited on Ge(100) using C_2H_4 and NH_3 coreactant gases, respectively. BCN thicknesses on Ge(100) were determined by XPS peak attenuation using the electron effective attenuation length for a Ge 3*d* photoelectron traveling through a BCN overlayer. This length was calculated as 3.41 nm from the TPP-2M equation within the NIST Electron Effective Attenuation Length Database [34]. XPS depth profiling of selected samples was performed by alternating XPS scans with Ar^+ sputter cycles lasting 30–120 s. The Ar^+ ion gun was operated at 2–4 kV, 25 mA beam current, 4×10^{-5} Torr ionization chamber pressure, and 1×1 or 3×3 mm^2 raster area.

BCN films of several different thicknesses (adjusted by changing the deposition time), were deposited on Ge(100) and GeNW samples. After post-BCN deposition *in situ* XPS analysis, the samples were left in ambient. Periodically the samples were

analyzed again with XPS to look for oxidation of the underlying Ge. Resistance to wet oxidation of several thicknesses of $BC_{0.7}N_{0.08}$ and $BC_{0.25}N_{0.4}$ deposited on Ge(100) was also tested. These samples were submerged in 50° C DI water for 1–20 min with periodic XPS evaluation.

Two BCN films deposited on Ge(100) were prepared for cross-sectional HRTEM analysis. Following BCN deposition and XPS analysis, the sample was transferred *in situ* to an ALD growth chamber where a 10 nm HfO_2 layer was deposited to protect the BCN–Ge(100) film stack. The ALD HfO_2 was deposited using tetrakis (ethylmethylamino) hafnium, kept at 85 °C, and H_2O, kept at room temperature, as precursors. The precursors were delivered into the ALD chamber by Ar carrier gas at a flow rate of 36sccm. The deposition was conducted at 250 °C, and one ALD cycle was composed of [Hf precursor dosing] / [Ar purging] / [H_2O dosing] / [Ar purging]. The growth rate of ALD HfO_2 was characterized to be 0.824Å/cycle, so a 121-cycle deposition was able to lead to the target thickness. Then a 300nm SiO_2 protection layer was deposited *ex situ* onto the HfO_2 / BCN / Ge(100) samples using radio-frequency sputtering. Thin cross sections for HRTEM were prepared using a dicing saw followed by focused ion beam (FIB) milling. The FIB milling was conducted with a FEI Strata™ DB235 dual beam SEM/FIB system, which combines a scanning electron microscope (SEM) with thermal emission tip for high resolution imaging and a focused ion beam (FIB) with gallium metal ion beam source for nanoscale cutting. The thinning process starts at a rough milling step under 3000 pA, followed by a fine milling step under 300 pA, and finally a cleaning cross-section milling step under 30 pA. A JOEL 2010F High Resolution Transmission Electron Microscope with field emission gun operated at 200 kV was used to acquire digital images of the SiO_2 / HfO_2 / BCN / Ge(100) cross-sections.

Following BCN deposition and XPS analysis of the GeNW samples, a 200 copper mesh lacey carbon TEM grid (Electron Microscopy Sciences) was scraped across the surface of the wires to collect a few for imaging. HRTEM images of the GeNWs suspended over vacuum were acquired at various magnifications using the same microscope. To estimate the oxide or BCN thickness on GeNWs, the amorphous layer thicknesses estimated from over 20 similar images were averaged.

3.3. RESULTS AND DISCUSSION

3.3.1. Ge(100)

3.3.1.1. Ambient Exposure

Figure 3.1 shows how the Ge *3d* XPS signal changes with increasing ambient exposure for several BCN films of different thickness deposited on Ge(100). The films were all grown with C_2H_4 coreactant, and were thus approximately $BC_{0.7}N_{0.08}$ stoichiometry. Figure 3.1(a) shows a Ge(100) control sample with no BCN overlayer. The *in situ* Ge *3d* scan, taken immediately after removal of the native oxide with HCl, shows a slight shoulder attributed to residual Ge suboxide, but no evidence of GeO_2. After only 6 h of ambient exposure, however, there is a strong GeO_2 contribution to the Ge *3d* signal. This feature continues to develop with increasing exposure as the oxide layer thickens.

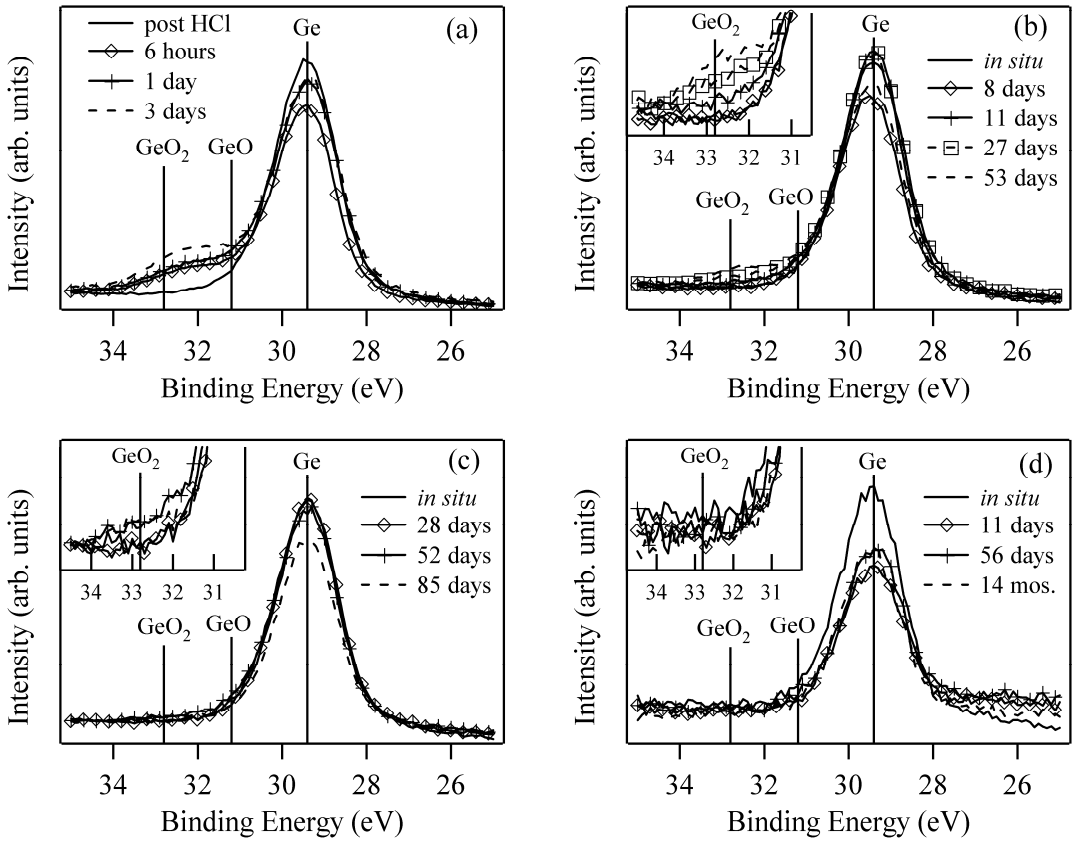

Figure 3.1. Evolution of Ge *3d* XP spectra with increasing ambient exposure for HCl-etched Ge(100) with (a) no BCN, (b) 2.3 nm BCN, (c) 3.2 nm BCN, and (d) 6.6 nm BCN.

In Fig. 3.1(b) there is no sign of Ge(100) oxidation for several days when a 2.3 nm BCN film is deposited. After 11 d ambient exposure there is a noticeable GeO_2 signal, which becomes more pronounced after 27 d of exposure. Ge(100) with a 3.2 nm BCN film does not show any signs of oxidation after 28 d of exposure (Fig. 3.1(c)). But at 52 d there is a subtle increase in the GeO_2 signal contribution. After 85 d the signal from the Ge^{+0} oxidation state at 29.4 eV decreases while the GeO_2 signal contribution

remains constant. This suggests the amount of GeO_2 increases between 52 d and 85 d of ambient exposure. A prior study in our laboratory determined that BCN deposited on Ge(100) does not become continuous until it is 2.5–5 nm thick [26]. Therefore GeO_2 formation for the 2.3 nm and 3.2 nm BCN / Ge(100) samples in Fig. 3.1(b),(c) is attributed to oxidation at exposed regions of Ge(100) due to discontinuous coverage by the BCN and not due to O diffusion through the BCN layer to the underlying substrate. A continuous 6.6 nm BCN overlayer in Fig. 3.1(d) shows no indication of GeO_2 formation for at least 14 months. This suggests that a continuous BCN coating protects Ge(100) from ambient oxidation.

In the process of oxidizing the exposed regions of Ge(100) substrates, ambient exposure also affects the BCN film. Figure 3.2 shows the B *1s* and C *1s* XP spectra for the 2.3 nm BCN / Ge(100) sample from Fig. 3.1(b). After just 1 d of ambient exposure, there are new binding features at ~ 192 eV in the B *1s* spectrum and ~ 288.4 eV in the C *1s* spectrum, indicating B–O and C–O bond formation, respectively. The majority of the B *1s* signal in Fig. 3.2(a) includes features at 188.3 eV and 189.3 eV, indicative of B–B and B–C bonding, respectively [33]. Prior to exposure to ambient, the C in the BCN film is found primarily in C–B (~ 283 eV) and C–C (~ 284.5 eV) binding states (Fig. 3.2(b)). The large increase in the C *1s* signal intensity around 284.5 eV after ambient exposure is due to adventitious C settling on the BCN surface [33]. Discussion of the N *1s* spectra is neglected due to minimal N composition (~ 5%) in these films.

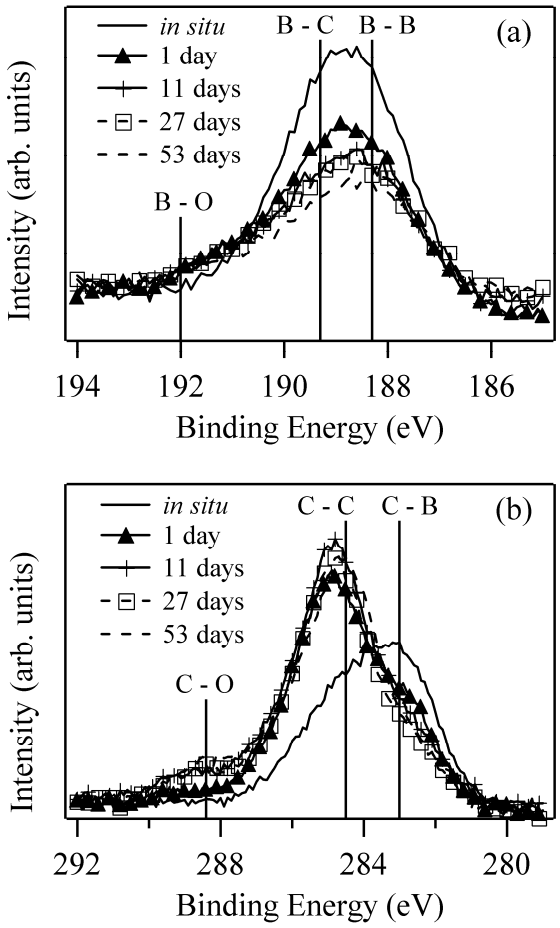

Figure 3.2. Evolution of (a) B *1s* and (b) C *1s* XP spectra with increasing ambient exposure for 2.3 nm BCN on Ge(100).

In Fig. 3.3 the atomic % O is calculated by XPS for BCN films of various thicknesses and plotted as a function of ambient exposure time. For the thinner 0.2 and 0.8 nm BCN films the % O steadily increases and does not appear to approach a limiting value. This is because BCN of this XPS-measured thickness is discontinuous. Large portions of the Ge(100) remain exposed, and ambient oxidation of these regions causes the % O to increase without bound. Conversely, the % O in the 6.6 nm BCN / Ge(100)

sample appears to saturate at 15–17% after a few days of exposure. Figure 3.1(d) showed that this continuous BCN film prevented oxidation of the Ge(100) substrate for at least 14 months. So the measured % O must be from O that becomes incorporated in the BCN film upon ambient exposure (similar to Fig. 3.2), not O that is reacting at the BCN–Ge(100) interface to create GeO_2. For the intermediate BCN film thicknesses in Fig. 3.3 (2.1, 2.3, and 3.2 nm) the % O increases rapidly within the first several days of ambient exposure then begins to level off after longer time spent in ambient. The rapid initial increase in % O is attributed to both O incorporation by the BCN and oxidation of exposed regions of Ge(100), since these films are presumed to be discontinuous. Because O uptake by BCN saturates after a few days, the continued, albeit slower, % O increase is due to continued GeO_2 formation at the exposed Ge(100) regions.

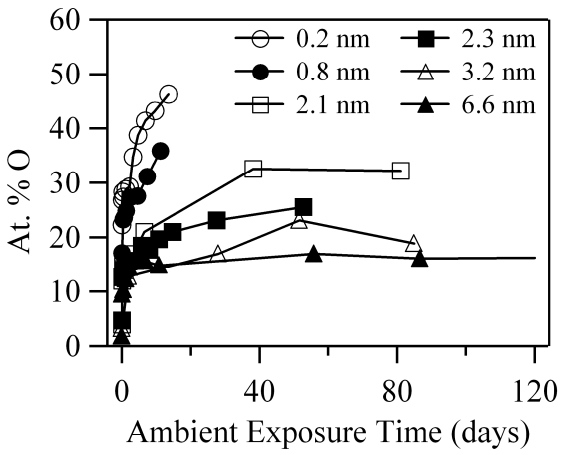

Figure 3.3. Atomic % O calculated from XPS for Ge(100) with BCN overlayers of various thickness versus ambient exposure time.

Further evidence of the self-limiting nature of BCN oxidation is provided by a series of XPS depth profiles in Fig. 3.4. Continuous BCN films ~ 10 nm thick were deposited on Ge(100) and exposed to ambient for various times. The % O measured by XPS is plotted versus the cumulative sputtering time with Ar^+ ions. After 300 s of sputtering, XPS peak attenuation indicates that ~ 5–7 nm of BCN is removed. The *in situ* depth profile shows that a BCN film that has not been exposed to ambient includes 3–4% O. After just 1 d exposure this value becomes 9–11% O, and after 2 weeks it increases to 13–15% O. But after 6 months in ambient, the O in the film is still 13–15%. These results suggest that BCN does not incorporate more than ~ 15% O upon ambient exposure, and this level is reached within the first several days of exposure. This limited O uptake is also evidence that any observed Ge(100) oxidation is due to exposed substrate regions and not due to O diffusion through the BCN overlayer.

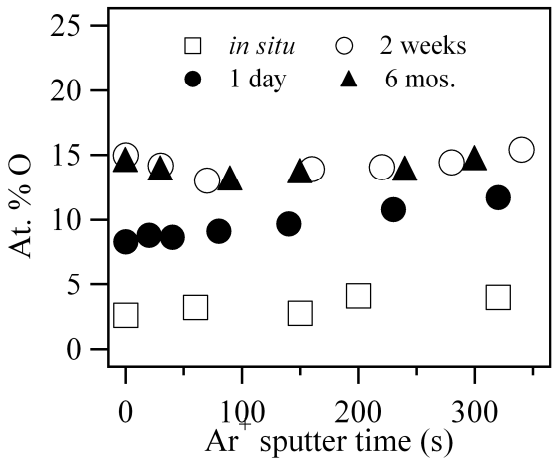

Figure 3.4. Atomic % O from XPS depth profile of ~ 10 nm BCN on Ge(100) after various ambient exposure times.

Figure 3.5(a) shows a cross-sectional HRTEM image of a discontinuous BCN film deposited on Ge(100) and *in situ* capped with HfO_2. Attenuation of the Ge *3d* substrate signal estimates this film at 2.2 nm. As expected from the film continuity study the BCN appears discontinuous [26]. The BCN film in Fig. 3.5(a) is 1.6 nm at its thickest region and nonexistent in some regions. It is these exposed regions that are susceptible to oxidation. Figure 3.5(b) shows a thicker BCN film grown on Ge(100); the XPS-based thickness is 3.8 nm. In this image the BCN–Ge(100) interface is well defined, and the coverage of BCN appears continuous. The continuous BCN in Fig. 3.5(b) ranges from 2.1 to 3.0 nm. This illustrates that XPS peak attenuation overestimates the actual BCN thickness, possibly from estimating too large a value for the electron effective attenuation length, λ. For XPS to accurately estimate the film thickness of the sample in Fig. 3.5(b), the value of λ for a Ge *3d* photoelectron would have to be 20–45% smaller than the 3.41 nm calculated from the TPP-2M equation within the NIST Electron Effective Attenuation Length Database [34]. This error is not unreasonable as one study reports that the actual value for λ can easily deviate 20% from the empirically-determined value [35]. Underestimation of the BCN overlayer density could be the source of a small amount of this error, but not 20–45%. In calculating λ, the density of BN (2.18 g/cm^3) [36] was used as an estimate of the BCN overlayer density. If the BCN density is closer to that of B_4C (2.5 g/cm^3) [36], this lowers the estimate of λ to 3.35 nm, a 2% decrease. For λ to be 20% smaller the BCN density would need to be ~ 6.5 g/cm^3, an unreasonable assumption. The overestimation of λ could alternatively be due to an overestimation of the inelastic mean free path (IMFP) from the TPP-2M equation for BCN. Deviations close to 20% have been observed between the IMFPs calculated from optical data and IMFPs calculated from the TPP-2M equation for inorganic compounds [37].

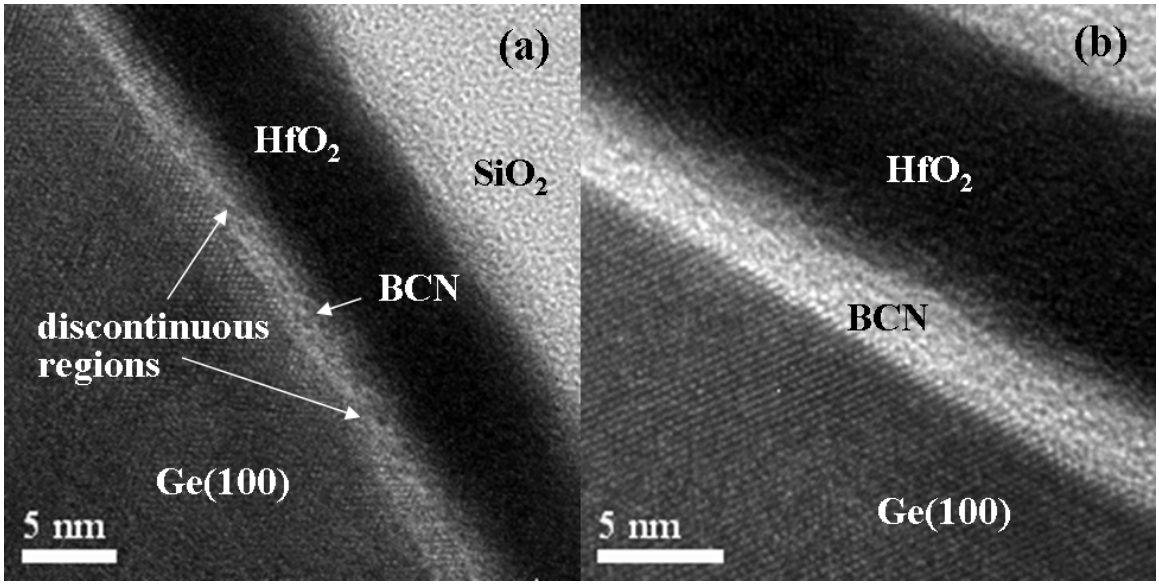

Figure 3.5. Cross-sectional HRTEM image of (a) discontinuous 2.2 nm BCN and (b) continuous 3.8 nm BCN on Ge(100). Both thicknesses are XPS-based.

Because of the overestimation of film thickness by XPS, the physical thickness of BCN that is capable of resisting oxidation of Ge(100) is likely less than the XPS-based thickness experiments discussed above. Though the actual film thickness is likely ~ 1–1.5 nm thinner, it is much more convenient to use XPS-based thicknesses for sample-to-sample comparisons than TEM. The time-consuming nature of TEM sample preparation makes it unfeasible to inspect every film studied, whereas *in situ* XPS analysis can quickly provide a basis for comparison for each experiment. Therefore the remainder of this chapter will continue to report BCN thicknesses measured by XPS peak attenuation, unless explicitly stated otherwise.

HfO_2 / BCN / Ge(100) film stacks similar to those in Fig. 3.5 were prepared for *in situ* XPS depth profile experiments to see how the Ge(100) interface is preserved by BCN

during HfO_2 deposition. Samples with 1.5 nm, 4.3 nm, and 8.7 nm BCN films were Ar^+ sputtered with periodic XPS analysis until the B *1s* signal was minimized in favor of the developing Ge *3p* and *2p* signals, indicating exposure of the BCN–Ge(100) interface; this interface was reached after ~ 1000, 1400, and 2000 s of sputtering, respectively. The Ge *3p* and Ge *2p* signals were tracked instead of Ge *3d* due to overlap with the Hf $5p_{3/2}$ signal. Figure 3.6 shows the normalized Ge *3p* and Ge *2p* signals at the BCN–Ge(100) interface for the three film stacks studied. The Ge *3p* signal in Fig. 3.6(a) is virtually identical for the 4.3 nm and 8.7 nm BCN layers, both of which should be continuous based on the HRTEM image of 3.8 nm BCN (Fig. 3.5(b)). However, the signal for the discontinuous 1.5 nm BCN film is broadened to include higher binding energy contributions for both the Ge $3p_{3/2}$ and $3p_{1/2}$ components. This is indicative of GeO_2 and/or Hf germanide formation. It is difficult to distinguish between the two binding states because they are only separated by ~ 0.4 eV in the 128–129 eV binding energy range [8]. The Ge *2p* signal in Fig. 3.6(b) confirms that GeO_2 forms when the 1.5 nm BCN film is exposed to the HfO_2 deposition process. Again there is no sign of GeO_2 formation for the thicker BCN films. These depth profiles suggest that continuous BCN films will resist Ge oxidation and electrically unstable germanide formation during deposition of a HfO_2 overlayer in an ALD process at 250 °C. This result is encouraging given the reported challenges associated with forming a quality high-κ oxide interface with Ge(100) for CMOS devices. BCN holds promise as potential interfacial control layer for such devices provided it does not introduce electrical defects.

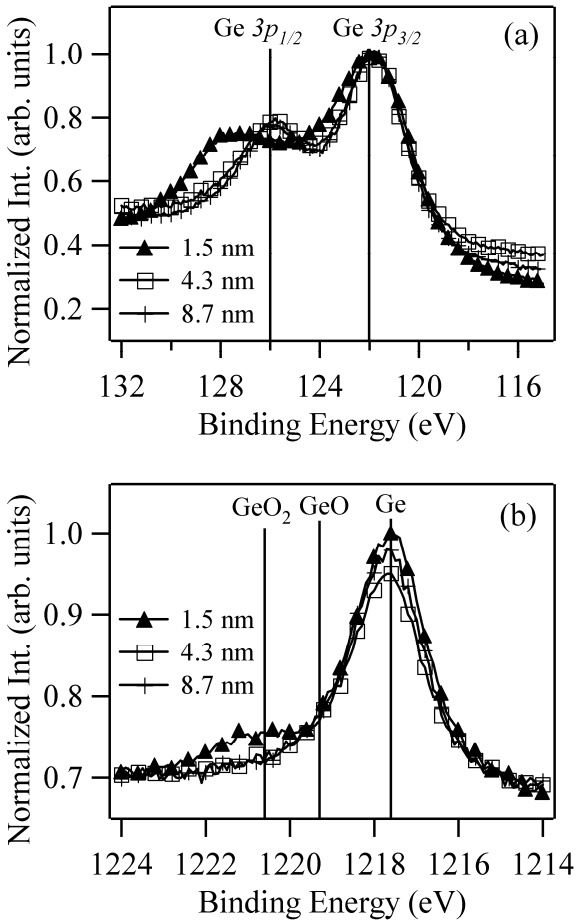

Figure 3.6. (a) Normalized Ge *3p* and (b) Ge *2p* XP spectra following Ar^+ sputtering to BCN–Ge(100) interface of HfO_2 / BCN / Ge(100) samples of varying BCN thickness.

3.3.1.2. DI Treatment

Wet oxidation of BCN-coated Ge(100) wafers was also tested by immersing the samples in 50 °C DI water for up to 20 min, conditions consistent with a recent Ge(100) wet oxidation study [6]. "C-rich" $BC_{0.7}N_{0.08}$ grown with C_2H_4 coreactant and "N-rich" $BC_{0.25}N_{0.4}$ deposited with NH_3 coreactant were both tested to look for differences in oxidation resistance behavior. After each DI treatment (either 1 min, 5 min, 10 min, or 20 min cumulative) XPS analysis was performed. Because GeO_2 dissolves in water, wet oxidation of Ge(100) produces GeO_x, which is evident by a subtle (< 1 eV) positive binding energy shift in the Ge *3d* signal from the Ge^{+0} state [6,38]. This is easily distinguished from the 3.4 eV binding energy shift exhibited by GeO_2 in the ambient oxidation studies discussed above [39]. Figure 3.7(a) shows representative Ge *3d* XP spectra for 1.9 nm N-rich BCN deposited on Ge(100) and treated with DI water for various times. After 10 min of cumulative DI treatment the Ge *3d* core level shifts ~ 0.3 eV as GeO_x forms. The Ge *3d* signal position after 20 min of treatment is shifted an additional 0.1 eV. In Fig. 3.7(b) there is no shift in the Ge *3d* core level after 20 min of DI treatment of 3.4 nm N-rich BCN on Ge(100). This suggests that N-rich BCN of this thickness sufficiently resists wet oxidation of Ge(100).

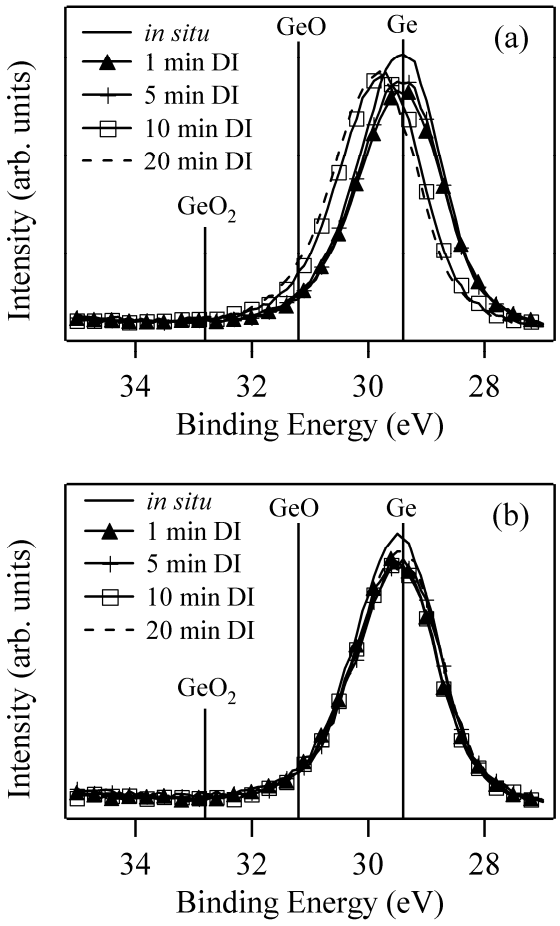

Figure 3.7. Representative Ge *3d* XP spectra for (a) 1.9 nm and (b) 3.4 nm N-rich BCN on Ge(100) for various 50 °C DI water treatment times.

Table 3.1 summarizes the DI treatment time that was necessary to detect GeO_x from the Ge *3d* signal shift for all samples tested. The thickness required to prevent GeO_x formation is between 3.0 and 4.0 nm for C-rich BCN and between 1.9 and 3.4 nm for N-rich BCN. The BCN thickness necessary to prevent wet oxidation of Ge(100) (4.0 nm for a C-rich film and 3.4 nm for a N-rich film) is consistent with the 4.3 nm BCN film that resisted oxidation of Ge(100) during a 250 °C ALD HfO_2 process involving H_2O

precursor. The absence of GeO_x formation in each of these cases is again attributed to the continuous nature of the BCN coating.

C-rich BCN		N-rich BCN	
BCN thickness	50 °C DI treatment result	BCN thickness	50 °C DI treatment result
0.2 nm	GeO_x after 1 min DI	0.5 nm	GeO_x after 1 min DI
1.1 nm	GeO_x after 4 min DI	1.9 nm	GeO_x after 10 min DI
3.0 nm	minor GeO_x after 20 min DI	3.4 nm	no GeO_x
4.0 nm	no GeO_x	4.3 nm	no GeO_x
9.3 nm	no GeO_x	5.1 nm	no GeO_x

Table 3.1. Summary of GeO_x observations for C-rich and N-rich BCN samples on Ge(100) after treatment with 50 °C DI for up to 20 min.

Figure 3.8(a) shows how the % O measured after the final DI treatment for each sample varies with thickness for C-rich and N-rich films. For all BCN films 3.4 nm and greater there was no evidence of GeO_x formation, so the % O measured is likely entirely due to water incorporated into the BCN. For discontinuous C-rich films ≤ 3.0 nm and N-rich films ≤ 1.9 nm, the % O measured by XPS likely includes contributions from the GeO_x at the exposed Ge(100) interface as well as water absorbed by the BCN film. The B *1s* and C *1s* spectra for both C-rich and N-rich DI-treated films (not shown) are similar to the spectra for the ambient-exposed BCN (Fig. 3.2). However the B–O and C–O contributions are somewhat less in the DI-treated films. The N *1s* spectra (not shown) of the N-rich films revealed significant N–O bond formation upon DI treatment. It is clear that some oxidation of the B, C, and N occurs upon exposure to DI water. Figure 3.8(b) shows that for the BCN films 3.4 nm and greater, which resist GeO_x formation, there is a rapid increase in % O upon initial DI treatment, but then there is little O accumulation with further treatment. The steady state O level in these films is 10– 15%. This behavior

is similar to the self-limiting oxidation of BCN observed for the ambient-exposed samples (Fig. 3.4).

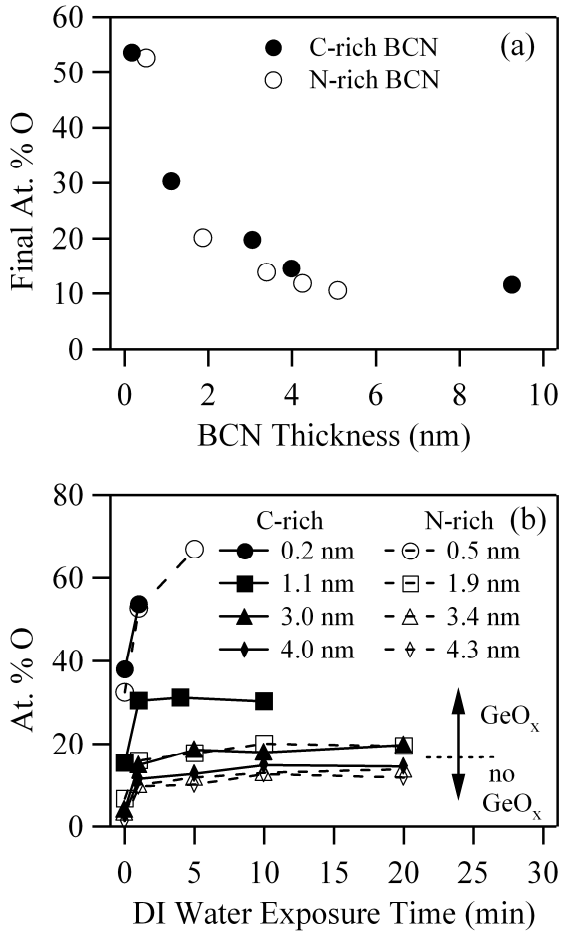

Figure 3.8. (a) Atomic % O measured after final 50 °C DI water treatment versus BCN overlayer thickness. (b) Atomic % O versus DI treatment time. The samples were C-rich and N-rich BCN overlayers of various thicknesses deposited on Ge (100).

Although resistance to GeO_x formation occurs with a thinner N-rich BCN film (3.4 nm) than C-rich BCN film (4.0nm) it is difficult to say that the higher N content makes BCN a better oxidation barrier because the thicknesses are very similar. But the results of the DI treatments demonstrate that a higher % N (and lower % C) does not make the BCN more susceptible to wet oxidation. This is contrary to a recent report that BCN films with lower C content incorporate more water moisture [28]. This contradiction with the cited study could be explained by a number of potential differences, including the film deposition method (plasma-assisted CVD with BCl_3, CH_4, and N_2 reactants at 390 °C), water treatment method (1 h DI water dip), and unknown H content in the film. Nonetheless, the comparable oxidation resistance of N-rich BCN to C-rich BCN motivates the use of N-rich BCN in future passivation studies. N-rich BCN may be a more promising passivation candidate for Ge(100) because of reports of enhanced electrical performance of nitridated Ge surfaces [31,32].

3.3.2. Ge Nanowires

BCN was also deposited on GeNWs to test oxidation resistance. Figure 3.9(a) shows a HRTEM image of a control GeNW that is untreated. A ~ 5 nm thick native oxide exists on the wire. After etching with HCl the oxide is mostly removed, except for ~ 1 nm of residual oxide (Fig. 3.9(b)). If the unpassivated wire is exposed to ambient, the oxide layer grows back, as demonstrated in Fig. 3.9(c) by the ~ 5 nm of oxide on the GeNW that was etched and left in ambient for 6 months. Analysis of the Ge *3d* spectra of a control GeNW sample that is etched and allowed to sit in ambient confirms this oxidation behavior. Figure 3.10 shows that upon etching, the GeO and GeO_2 features are reduced. The higher binding energy signals are not eliminated entirely, however. This suggests a small amount of oxide remains, as was seen in Fig. 3.9(b). After just one

week of ambient exposure the Ge *3d* signal shows significant signs of oxidation for an unpassivated wire.

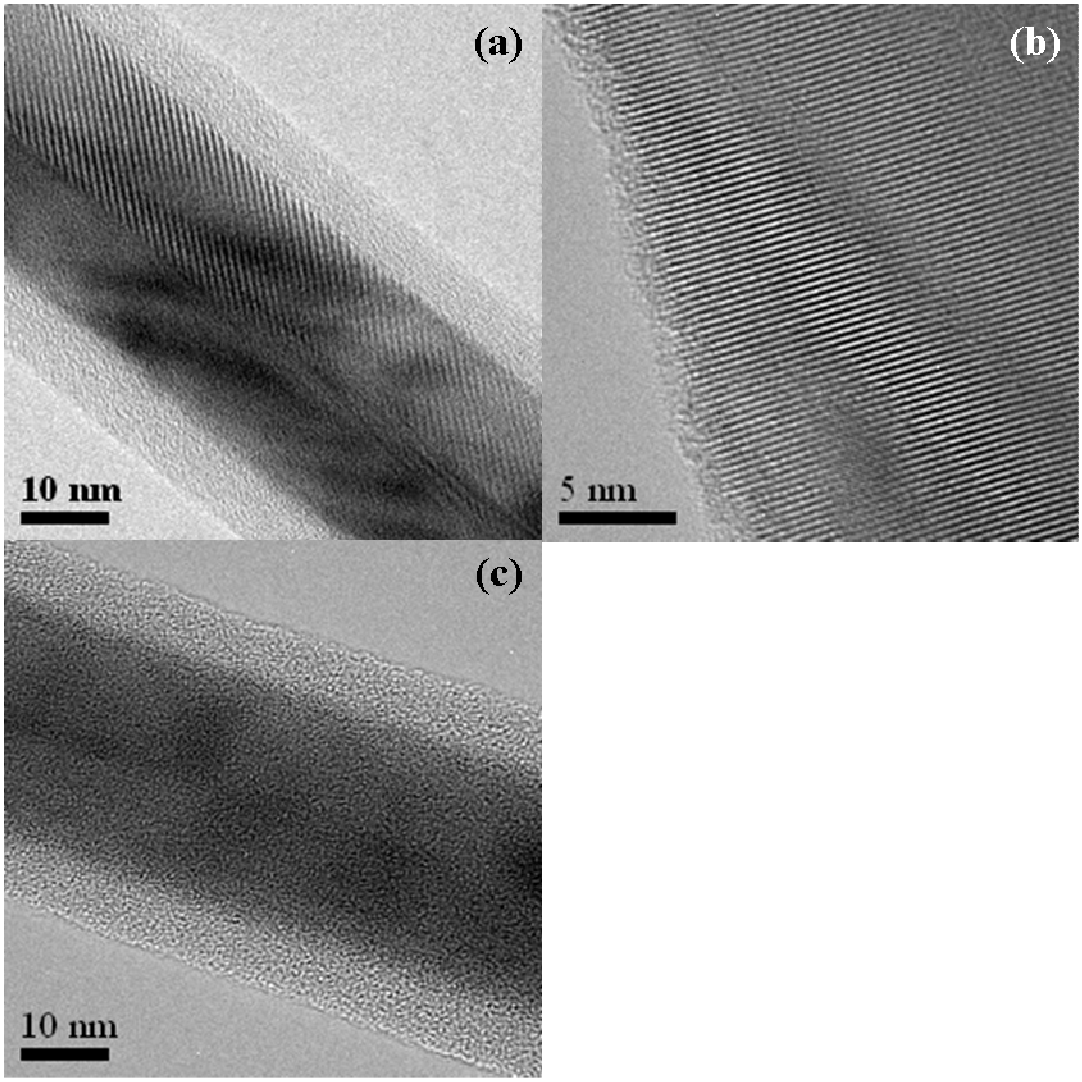

Figure 3.9. HRTEM image of GeNW that is (a) untreated, (b) HCl-etched and exposed to ambient for 2 h and (c) HCl-etched and exposed to ambient for 6 months.

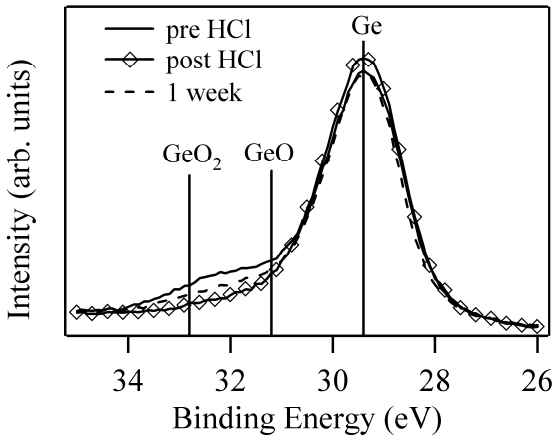

Figure 3.10. Evolution of Ge *3d* XP spectra for untreated GeNW sample following HCl etch and 1 week ambient exposure.

Figure 3.11(a),(b) shows representative HRTEM images of a GeNW passivated with BCN after removal of the oxide layer with HCl. The average BCN thickness on this GeNW sample was 2.7 nm, estimated by HRTEM. Given the wide range of photoelectron takeoff angles detected from a three-dimensional mass of GeNWs, it may be inappropriate to use XPS to accurately estimate the thickness of a BCN coating on a wire. Therefore only HRTEM-measured thicknesses are reported for the GeNW studies. The BCN forms an abrupt interface with the GeNW, as is evident by the sharp transition from the single crystal Ge to the amorphous BCN coating. Furthermore, the BCN appears to coat the nanowire uniformly, with little variation in overlayer thickness. Figure 3.11(c) shows that the thin BCN coating appears unchanged by 5 months of ambient exposure. However, the Ge *3d* signal in Fig. 3.12(a) shows that this BCN-coated GeNW sample begins to form GeO_2 after 50 d of ambient exposure. In Fig. 3.12(b) the Ge *2p* signal, which is more surface sensitive due to its shorter electron attenuation

length, more clearly shows the formation of GeO_2 after 50 d. The Ge *3d* and *2p* spectra show more GeO_2 formation after 5 months of ambient exposure. Analysis of the B *1s* and C *1s* signals (not shown) show similar B–O and C–O bond formation as the BCN samples deposited on Ge(100) (Fig. 3.2).

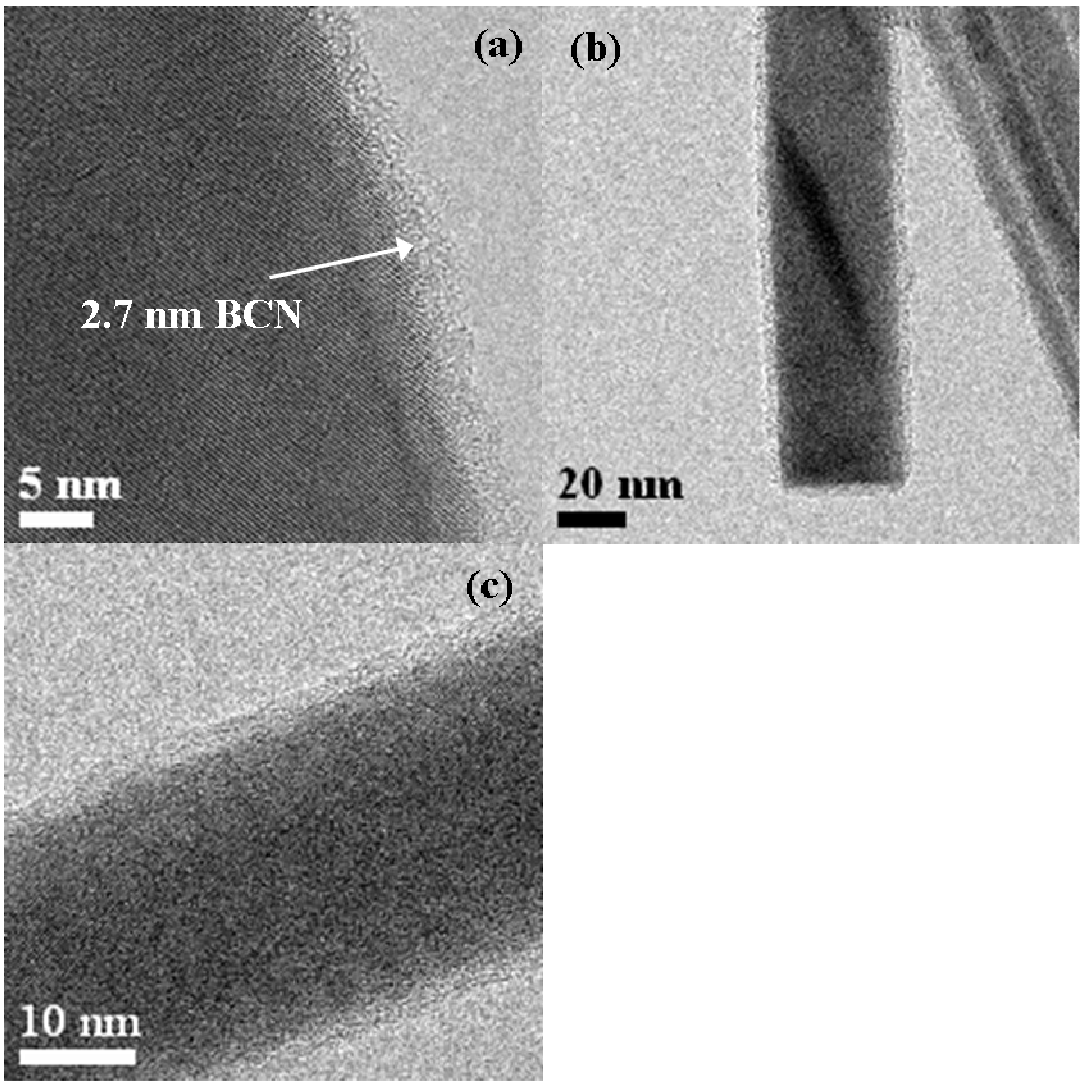

Figure 3.11. HRTEM image of 2.7 nm BCN on GeNW after (a), (b) 2 h ambient exposure, and (c) 5 months ambient exposure.

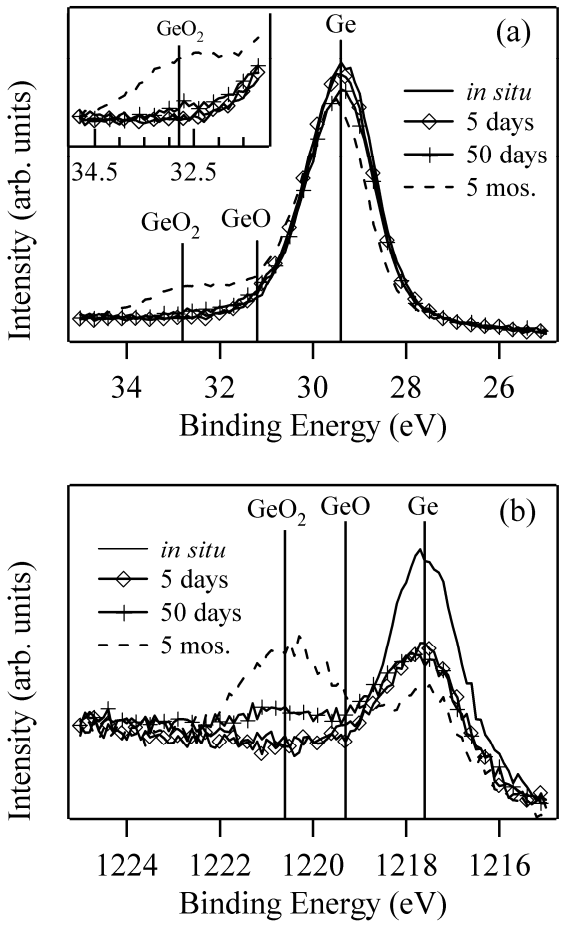

Figure 3.12. Evolution of (a) Ge *3d* and (b) Ge *2p* XP spectra with increasing ambient exposure for 2.7 nm BCN on GeNW.

Figure 3.13 shows HRTEM images of a GeNW passivated with a thicker 5.7 nm BCN layer. Again there is little difference between a representative image taken within 2 h of initial ambient exposure (Fig. 3.13(a)) and one taken after 5 months of exposure (Fig. 3.13(b)). The Ge *3d* spectra in Fig. 3.14 indicate that BCN of this thickness is capable of withstanding oxidation of the GeNW for at least 5 months.

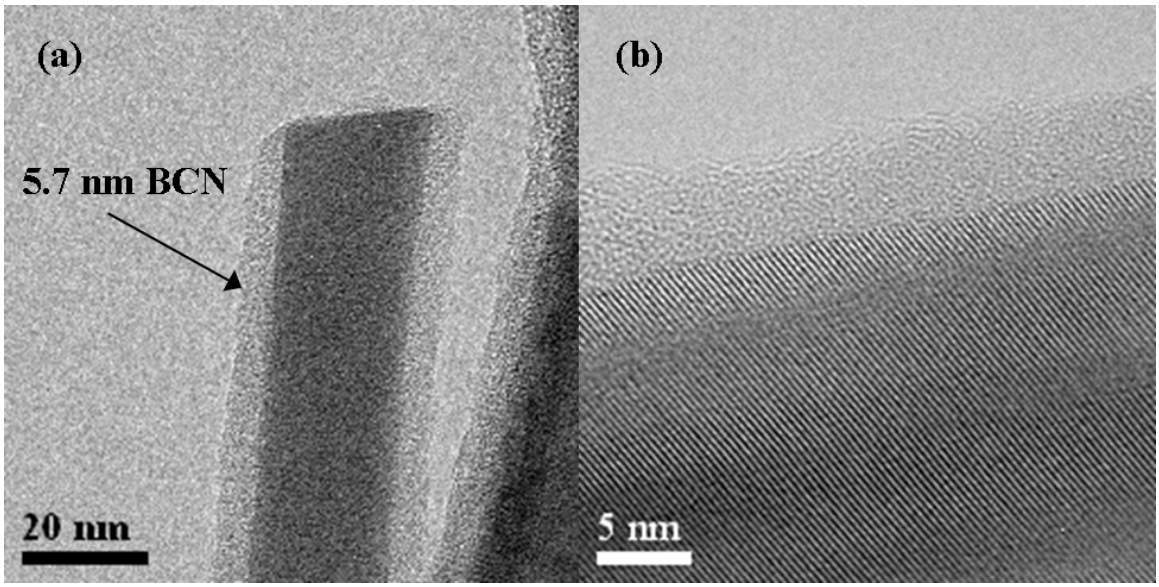

Figure 3.13. HRTEM image of 5.7 nm BCN on GeNW after (a) 2 h ambient exposure and (b) 5 months ambient exposure.

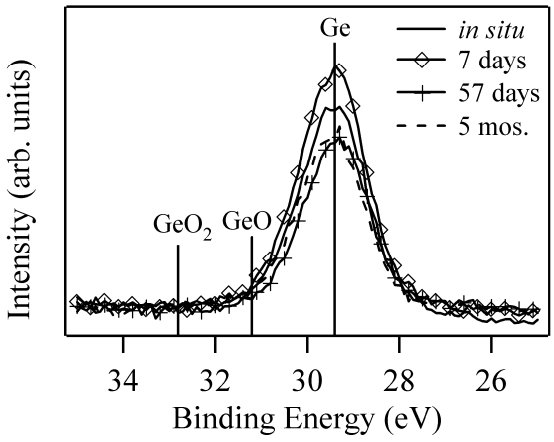

Figure 3.14. Evolution of Ge *3d* XP spectra with increasing ambient exposure for 5.7 nm BCN on GeNW.

The inability of the thinner 2.7 nm BCN layer to resist oxidation of the GeNW is likely due to discontinuous coverage of the wire that is not evident in the HRTEM images. Though the representative images in Fig. 3.11 make the BCN film look uniform and continuous, it is possible that the two dimensional representation of the three dimensional wire obscures some exposed regions of the GeNW. Prior characterization of the GeNWs reveals a combination of {111} and {100} surface facets [13]. BCN film growth on Ge(111) could behave differently than growth on Ge(100), so some facets of the wire may have a thinner, perhaps discontinuous BCN coating. Furthermore, comparison of the oxidized wires in Fig. 3.9(a),(c) with the BCN-coated wires in Figs. 3.11 and 3.13 shows that it is difficult to distinguish the amorphous GeO_2 from amorphous BCN. It is possible then that the ambient-exposed GeNW in Fig. 3.11(c) includes portions of GeO_2 that are indistinguishable from the BCN. This would be consistent with the GeO_2 witnessed in XPS (Fig. 3.12).

An alternative explanation for the detection of GeO_2 in spite of the unchanged wire appearance could be that the GeNW samples imaged by HRTEM are different from the GeNWs analyzed by XPS. The wires collected for HRTEM analysis were obtained by lightly scraping a TEM grid over the top surface of a much thicker, tangled collection of wires. This larger mass of GeNWs was used for XPS analysis. If BCN deposition was not uniform over the entire collection then it is possible that oxidation of GeNWs with a BCN layer of lower average thickness (< 2.7 nm) was detected by XPS.

3.4. SUMMARY

Films of $BC_{0.7}N_{0.08}$ stoichiometry were deposited on Ge(100) to test their ability to resist oxidation of Ge in several different oxidizing environments. The minimum BCN thickness that completely covers the Ge(100) substrate and prevents oxidation is ~ 4 nm. XPS analysis of the Ge *3d* spectra shows that a 6.6 nm BCN film resists oxidation of Ge(100) for at least 14 months. A 3.2 nm BCN film, which likely leaves a minor portion of the Ge(100) surface exposed, begins to show signs of GeO_2 formation after 2 months of ambient exposure. GeO_2 forms on an unpassivated control Ge(100) surface within several hours of ambient exposure. Oxidation of the BCN overlayer occurs immediately upon ambient exposure, leading to significant B–O and C–O bonding features within the film. XPS depth profile experiments reveal that this O incorporation saturates at 15% O, with no change in the % O from 2 weeks to 6 months of ambient exposure. This suggests that despite some oxidation of the BCN passivation layer, the underlying Ge(100) is protected.

In situ XPS depth profiles of HfO_2 / BCN / Ge(100) film stacks suggest that continuous BCN also resists formation of GeO_2 and Hf germanide upon exposure to the oxidizing environment of a 250 °C ALD HfO_2 process. Wet oxidation of BCN-coated

Ge(100) was studied by immersing samples in 50 °C DI water for up to 20 min and tracking GeO_x formation with XPS. The minimum C-rich $BC_{0.7}N_{0.08}$ film thickness required to resist GeO_x was between 3.0 and 4.0 nm, consistent with the minimum thickness at which BCN resists ambient oxidation of Ge(100).

BCN passivation of GeNWs was also studied. A 5.7 nm BCN film resists oxidation of a GeNW for at least 5 months. HRTEM images upon initial ambient exposure and after 5 months show no change, with BCN forming a sharp, abrupt interface with the Ge surface.

Based on the ability of continuous BCN films to resist Ge oxidation under several different oxidizing conditions, BCN appears to be a promising passivation candidate for Ge. This motivates further passivation studies of BCN on Ge(100) and GeNWs, including a look at the electrical characteristics of the BCN–Ge interface.

3.5. REFERENCES

[1] A. M. Morales and C. M. Lieber, Science **279**, 208 (1998).

[2] T. Hanrath and B. A. Korgel, J. Am. Chem. Soc. **124**, 1424 (2002).

[3] A. D. Schricker, S. V. Joshi, T. Hanrath, S. K. Banerjee, and B. A. Korgel, J. Phys. Chem. B **110**, 6816 (2006).

[4] D. W. Wang, Q. Wang, A. Javey, R. Tu, H. J. Dai, H. Kim, P. C. McIntyre, T. Krishnamohan, and K. C. Saraswat, Appl. Phys. Lett. **83**, 2432 (2003).

[5] D. W. Wang, Y. L. Chang, Q. Wang, J. Cao, D. B. Farmer, R. G. Gordon, and H. J. Dai, J. Am. Chem. Soc. **126**, 11602 (2004).

[6] K. Park, Y. Lee, J. Lee, and S. Lim, Appl. Surf. Sci. **254**, 4828 (2008).

[7] M. Houssa, G. Pourtois, B. Kaczer, B. De Jaeger, F. E. Leys, D. Nelis, K. Paredis, A. Vantomme, M. Caymax, M. Meuris, and M. M. Heyns, Microelectron. Eng. **84**, 2267 (2007).

[8] M. Caymax, M. Houssa, G. Pourtois, F. Bellenger, K. Martens, A. Delabie, and S. Van Elshocht, Appl. Surf. Sci. **254**, 6094 (2008).

[9] J. A. Appelbaum, G. A. Baraff, D. R. Hamann, H. D. Hagstrum, and T. Sakurai, Surf. Sci. **70**, 654 (1978).

[10] Y. J. Chabal, Surf. Sci. **168**, 594 (1986).

[11] J. Y. Maeng, J. Y. Lee, Y. E. Cho, S. Kim, and S. K. Jo, Appl. Phys. Lett. **81**, 3555 (2002).

[12] L. Papagno, X. Y. Shen, J. Anderson, G. S. Spagnolo, and G. J. Lapeyre, Phys. Rev. B **34**, 7188 (1986).

[13] T. Hanrath and B. A. Korgel, J. Am. Chem. Soc. **126**, 15466 (2004).

[14] H. Adhikari, P. C. McIntyre, S. Y. Sun, P. Pianetta, and C. E. D. Chidsey, Appl. Phys. Lett. **87** (2005).

[15] D. Bodlaki, H. Yamamoto, D. H. Waldeck, and E. Borguet, Surf. Sci. **543**, 63 (2003).

[16] K. Choi and J. M. Buriak, Langmuir **16**, 7737 (2000).

[17] Z. H. Lu, Appl. Phys. Lett. **68**, 520 (1996).

[18] G. W. Cullen, J. A. Amick, and D. Gerlixh, J. Electrochem. Soc. **109**, 124 (1962).

[19] G. W. Anderson, M. C. Hanf, P. R. Norton, Z. H. Lu, and M. J. Graham, Appl. Phys. Lett. **66**, 1123 (1995).

[20] P. F. Lyman, O. Sakata, D. L. Marasco, T. L. Lee, K. D. Breneman, D. T. Keane, and M. J. Bedzyk, Surf. Sci. **462**, L594 (2000).

[21] S. M. Han, W. R. Ashurst, C. Carraro, and R. Maboudian, J. Am. Chem. Soc. **123**, 2422 (2001).

[22] J. L. He, Z. H. Lu, S. A. Mitchell, and D. D. M. Wayner, J. Am. Chem. Soc. **120**, 2660 (1998).

[23] S. Van Elshocht, M. Caymax, T. Conard, S. De Gendt, I. Hoflijk, M. Houssa, F. Leys, R. Bonzom, B. De Jaeger, J. Van Steenbergen, W. Vandervorst, M. Heyns, and M. Meuris, Thin Solid Films **508**, 1 (2006).

[24] N. Wu, Q. C. Zhang, D. S. H. Chan, N. Balasubramanian, and C. X. Zhu, IEEE Electron Device Lett. **27**, 479 (2006).

[25] E. R. Engbrecht, Y. M. Sun, K. H. Junker, J. M. White, and J. G. Ekerdt, J. Vac. Sci. Technol. A **22**, 2152 (2004).

[26] P. R. Fitzpatrick and J. G. Ekerdt, J. Vac. Sci. Technol. A **26**, 1397 (2008).

[27] Q. D. Nghiem and D. P. Kim, J. Mater. Chem. **15**, 2188 (2005).

[28] H. Aoki, D. Watanabe, R. Moriyama, M. K. Mazumder, N. Komatsu, C. Kimura, and T. Sugino, Diamond Relat. Mater. **17**, 628 (2008).

[29] S. Umeda, T. Yuki, T. Sugiyama, and T. Sugino, Diamond Relat. Mater. **13**, 1135 (2004).

[30] E. R. Engbrecht, P. R. Fitzpatrick, K. H. Junker, Y. M. Sun, J. M. White, and J. G. Ekerdt, J. Mater. Res. **20**, 2218 (2005).

[31] A. Ritenour, A. Khakifirooz, D. A. Antoniadis, R. Z. Lei, W. Tsai, A. Dimoulas, G. Mavrou, and Y. Panayiotatos, Appl. Phys. Lett. **88** (2006).

[32] W. P. Bai, N. Lu, A. Ritenour, M. L. Lee, D. A. Antoniadis, and D. L. Kwong, IEEE Electron Device Lett. **27**, 175 (2006).

[33] J. F. Moulder, W. F. Stickle, P. E. Sobol, and K. D. Bomben, *Handbook of X-ray Photoelectron Spectroscopy*. (Physical Electronics, Inc., Eden Prairie, MN, 1995).

[34] C. J. Powell and A. Jablonski, NIST Electron Effective Attenuation Length Database (National Institute of Standards and Technology, Gaithersburg, MD, 2001).

[35] B. Feddes, A. M. Vredenberg, J. G. C. Wolke, and J. A. Jansen, Surf. Interface Anal. **35**, 287 (2003).

[36] D. R. Lide, *CRC Handbook of Chemistry and Physics*, 88 (Internet Version 2008) ed. (CRC Press/Taylor and Francis, Boca Raton, FL, 2008).

[37] S. Tanuma, C. J. Powell, and D. R. Penn, Surf. Interface Anal. **17**, 927 (1991).

[38] K. Prabhakaran and T. Ogino, Surf. Sci. **325**, 263 (1995).

[39] D. Schmeisser, R. D. Schnell, A. Bogen, F. J. Himpsel, D. Rieger, G. Landgren, and J. F. Morar, Surf. Sci. **172**, 455 (1986).

Chapter 4: Electrical characteristics of BC_xN_y on Ge(100) and Si(100)

4.1. INTRODUCTION

To improve the channel mobility of complementary metal oxide semiconductor (CMOS) devices beyond what is achievable for Si, Ge has received considerable attention as an alternative semiconductor [1-7]. This is due to the higher intrinsic carrier mobility in Ge compared to Si (~ 4× and 3× improvement for holes and electrons, respectively) [8]. However, the chemical and electrical instability of Ge's native oxide prevents its use as a gate dielectric. Unlike SiO_2, GeO_2 is both water-soluble and thermally unstable [9], and a high density of interface states (> 10^{13} cm^{-2}) plagues the Ge–oxide interface [1,2,10,11]. These interface states serve as charge traps, which reduce mobility and contribute to device hysteresis [11-13]. Integration of Ge into CMOS devices with a high-κ dielectric, such as HfO_2 or ZrO_2, has proven difficult as well. Recent studies have shown that HfO_2 deposition on Ge(100) results in Hf–Ge bond formation, which produces interface states in the band gap [2,14].

A passivation layer is needed to chemically and electrically stabilize the surface of Ge to make it viable for use in CMOS applications. The first requirement of this film is that it should form a continuous layer on the Ge surface. Discontinuous coverage would not only allow formation of the unstable native GeO_x, but additional poor interfaces could result during device processing. The continuous layer also needs to be as thin and uniform as possible to preserve the equivalent oxide thickness (EOT) of the high-κ / passivation layer film stack while maintaining low leakage current. The passivating layer should also form a clean, abrupt interface with Ge. A poor interface where intermixing or incomplete bonding with the Ge surface occurs will result in

mechanical or electrical defects that will serve as charge trapping centers. The passivation film must also resist oxidation of the underlying Ge during high-κ gate oxide deposition. Finally, the layer must behave well electrically when sandwiched between Ge and the high-κ oxide in a metal insulator semiconductor (MIS) structure.

Various Ge passivation layers have been investigated as a means to control the interface that Ge forms with a high-κ oxide, including Si / SiO_2 [1,14], thermally grown GeO_2 [14,15], TaON [16,17], and Dy_2O_3 [18]. Another approach has been to employ nitrogen to produce GeON or Ge_3N_4 [19-23]. The incorporation of N into the interfacial passivation layer has been shown to reduce the density of interface states and prevent the interdiffusion of Ge or high-κ species across the passivation interface [17,19,20,22]. While some passivation efforts have been successful at reducing interface state densities (low to mid 10^{11} cm^{-2}) [22,24] and improving mobility for pMOS Ge devices [4,5,25], n-type devices continue to perform poorly [26-28].

This study seeks to electrically passivate the Ge(100) surface with thin (< 5 nm), amorphous films of boron carbo-nitride (BC_xN_y). BC_xN_y films deposited by chemical vapor deposition (CVD) in our laboratory have tunable dielectric constants ($3.7 < \kappa < 4.6$) and stoichiometry ($0.05 \leq x \leq 1.51$, $0.05 \leq y \leq 0.67$) [29]. Two prior BC_xN_y (henceforth referred to as BCN for simplicity) passivation studies in our laboratory revealed that when BCN is ~ 4 nm it should be sufficiently thick to achieve continuous coverage of a Ge(100) substrate [30] and prevent oxidation of the Ge both in ambient and during a 250 ºC atomic layer deposition (ALD) HfO_2 process [31]. BCN was also observed to form an abrupt interface with Ge(100), with no signs of intermixing [30]. Motivated by these preliminary studies that addressed the passivation issues of film continuity, interface formation, and oxidation resistance, this work examines the ability of BCN to electrically passivate the Ge(100) surface.

To test the electrical properties of BCN-passivated Ge(100), MIS capacitor structures of TaN / HfO_2 / BCN / Ge(100) are fabricated and the capacitance-voltage (*C–V*) and current-voltage (*I–V*) characteristics are measured. Though C-rich $BC_{0.7}N_{0.08}$ ($\kappa \approx 3.7$) [29] has been the focus of recent studies [30,31], this work will primarily focus on N-rich $BC_{0.13}N_{0.45}$ ($\kappa \approx 4.4$) [29] films partially due to the improvement of Ge device electrical properties with N-containing passivation layers [17,19,20,22]. Depositions at substrate temperatures ranging from 275–400 ºC are compared in an attempt to optimize device performance. The effect of deposition temperature on the film's stoichiometry, optical properties, and resistance to ambient oxidation is also investigated. MIS devices fabricated on Si(100) substrates are also studied for comparison.

4.2. EXPERIMENTAL

BCN films were deposited on 2.2 × 2.2 cm substrates cleaved from larger wafers of either Ge(100) (n-type and undoped, Waferworld), Si(100) (n- and p-type), or 10.7 nm thermally grown SiO_2 / Si(100) (n-type). Prior to film growth, a preclean step was performed to remove adventitious carbon (Si(100) and SiO_2) and the native oxide layer (Ge(100) and Si(100)). All substrates were sonicated for 5 min in acetone, followed by a brief ethanol and de-ionized (DI) water rinse. Si(100) substrates were subsequently etched for 20 min in piranha solution (H_2SO_4 : H_2O_2 : H_2O = 6:2:1), etched for 30 s in 1% HF solution, and rinsed for 5 s in DI water. SiO_2 substrates received the same treatment without the HF etch. Ge(100) samples were subsequently etched with five 30 s 1% HF / 30 s DI water rinse cycles, substituting a 5 s rinse for the last DI water step [4,16,17,20]. After cleaning, each sample was dried with He and immediately (< 5 min ambient exposure time) loaded into vacuum for BCN film growth and analysis.

The system used to conduct all *in situ* experiments consists of a vacuum load lock, sample transfer system, CVD growth chamber for BCN, ALD chamber for HfO_2, and an x-ray photoelectron spectroscopy (XPS) analysis chamber with Ar^+ sputter capabilities. After removing the native oxide and loading the substrate into the vacuum load lock, a pre-deposition XPS scan was taken. The sample was then transferred to the CVD chamber and thin (4.5–5 nm) or thick (15–25 nm) BCN was deposited for MIS capacitor fabrication or *ex situ* analysis, respectively. BCN films were grown by thermal CVD using a commercially available solid dimethylamine borane [$NH(CH_3)_2 : BH_3$] (DMAB) precursor complex (melting point 36 ºC) and C_2H_4 or NH_3 coreactant gases for C-rich or N-rich films, respectively. A detailed description of the CVD procedure is provided elsewhere [31]. Depositions were conducted at substrate temperatures ranging from 275–400 ºC, determined using a reference thermocouple previously calibrated to a Si(100) wafer with a thermocouple glued to the surface. After BCN deposition, the sample was cooled to 150 ºC for 15 min under 10 standard cm^3 / min (sccm) Ar at 1 Torr and transferred to the XPS chamber for post-deposition analysis.

Samples were analyzed *in situ* in a chamber consisting of an XPS system and an ion gun for Ar^+ sputtering. The analysis chamber was kept at a base pressure of 6×10^{-9} Torr. XPS measurements were taken using a Physical Electronics 5500™ XPS system with an Al anode and 56.7 eV pass energy. BCN film composition was calculated using sensitivity factors for incident X-rays at 54.7º to the analyzer [32]. The thickness of thin BCN films on Si(100), SiO_2 / Si(100), and Ge(100) was determined by XPS peak attenuation using effective attenuation lengths (λ) calculated from the TPP-2M equation within the NIST Electron Effective Attenuation Length Database [33]. For a Si 2*p* and Ge 3*d* photoelectron traveling through a BCN overlayer, the calculated values were $\lambda_{Si,BCN}$ = 3.24 nm and $\lambda_{Ge,BCN}$ = 3.41 nm, respectively. PeakFit™ software was used to

deconvolute the XP spectra for each element into the individual bonding states. The peaks were fit using a Gaussian-Lorentzian sum function. The full width half maximums (FWHM) of the peaks were fixed using the following reference samples: PVD TaC_x for C 1*s* (1.8 eV), BN for B 1*s* (2.1 eV) and N 1*s* (1.8 eV) [29].

Following post-deposition XPS analysis, thin BCN samples intended for MIS capacitor fabrication were transferred *in situ* to the ALD chamber, where a 10 nm HfO_2 layer was deposited at 250 ºC using a procedure described elsewhere [31]. The sample was transferred back to the analysis chamber for post-HfO_2 deposition XPS and then removed from vacuum. Immediately (~ 10–15 min ambient exposure) following the HfO_2 / BCN depositions a 5 min post-deposition anneal (PDA) was performed in a quartz tube furnace at 400 ºC under 300 mTorr H_2. The sample was then loaded into a physical vapor deposition chamber, and an array of 300–400 μm diameter TaN dots were deposited using a shadow mask. The sample was then cleaved in half, and one portion received a 30 min post-metallization anneal (PMA) at 300 ºC under 300 mTorr H_2. Both pieces were mounted to a larger Si wafer piece using colloidal Ag paste (Ted Pella, Inc.) after scratching the backside to ensure an ohmic contact. Electrical testing of MIS devices was then performed on a Süss probe station with a Keithley 4200 semiconductor characterization system and a Keithley 590 CV analyzer. *C–V* measurements were made at 100 kHz over a -2V to 3.5V range, and *I-V* measurements were taken over a -3.5 V to 3.5 V range.

Thick BCN films were analyzed ex situ by spectroscopic ellipsometry on a J.A. Woollam VASETM instrument. Measurements were conducted at 65º and 70º relative to normal at wavelengths (λ) ranging from 190–1000 nm. Film thickness was calculated by fitting a two parameter Cauchy film model over the 500 – 1000 nm wavelength range. The refractive index, n, and extinction coefficient, k, were determined by a point-by-point

fit over the entire wavelength range after fixing the Cauchy film model values. The absorption coefficient, α, was calculated from the extinction coefficient using the following relation [34].

$$\alpha = \frac{4\pi k}{\lambda} \tag{4.1}$$

To monitor changes in %O upon ambient exposure, XPS depth profiling of selected thick BCN films was performed by alternating XPS scans with Ar^+ sputter cycles lasting 100–500 s. The Ar^+ ion gun was operated at 2 kV, 25 mA beam current, 4.5×10^{-5} Torr ionization chamber pressure, and 3×3 mm^2 raster area. Ambient exposure times ranged from 2 d to 35 d.

4.3. RESULTS

Before conducting experiments designed to optimize the electrical characteristics of MIS devices containing BCN passivation layers, a comparison of C-rich and N-rich BCN films was made to determine the stoichiometry that would perform better electrically. C-rich films of $BC_{0.61}N_{0.08}$ stoichiometry and N-rich films of $BC_{0.13}N_{0.45}$ stoichiometry were deposited at 350 ºC on Si(100) substrates. The B 1*s*, C 1*s*, and N 1*s* XP spectra were deconvoluted for each film to determine the relative contributions of the various bonding states. Figure 4.1 demonstrates this deconvolution for the C 1*s* spectra. For both films, C bonded to B, indicated by the signal at 283.2 eV, is the dominant bonding arrangement for C atoms. But the C-rich BCN film also includes C–C (284.5 eV) and C–N (286.5 eV) bonding features, which are not as prominent in the N-rich film. The B 1*s* deconvoultion (not shown) provided the relative amounts of B–B (188.3 eV), B–C (189.3 eV), and B–N (190.4 eV) bonding; and the N 1*s* deconvolution (not shown)

provided the N–B (398.1 eV) and N–C (400.4 eV) contributions [29,32]. Table 4.1 summarizes these results. The film composition values are the atomic percentages of each element calculated from the total area of the B 1*s*, C 1*s*, N 1*s*, and O 1*s* spectra, taking into account the atomic sensitivity factors [32]. The lower portion of Table 4.1 lists the % contribution of each deconvoluted peak to the total area of its respective element's XP spectrum. As an example, the deconvoluted C–B peak contribution for C-rich BCN in Fig. 4.1 constitutes 65 % of the total C 1*s* spectrum area.

Film Composition (percentage)			
		C-rich BCN	N-rich BCN
	B	58%	62%
	C	35%	8%
	N	5%	28%
	O	2%	2%
Deconvoluted Peak Contribution (percentage)			
		C-rich BCN	N-rich BCN
B 1*s*	B–B	80%	46%
	B–C	15%	21%
	B–N	5%	33%
C 1*s*	C–B	65%	84%
	C–C	31%	10%
	C–N	4%	6%
N 1*s*	N–B	83%	86%
	N–C	17%	14%

Table 4.1. Comparison of film composition and contribution of deconvoluted bonding states to the total area of the B 1*s*, C 1*s*, and N 1*s* XP spectra for C-rich and N-rich BCN film (350 ºC deposition on Si(100)) following 500 s Ar^+ sputter at 5 kV.

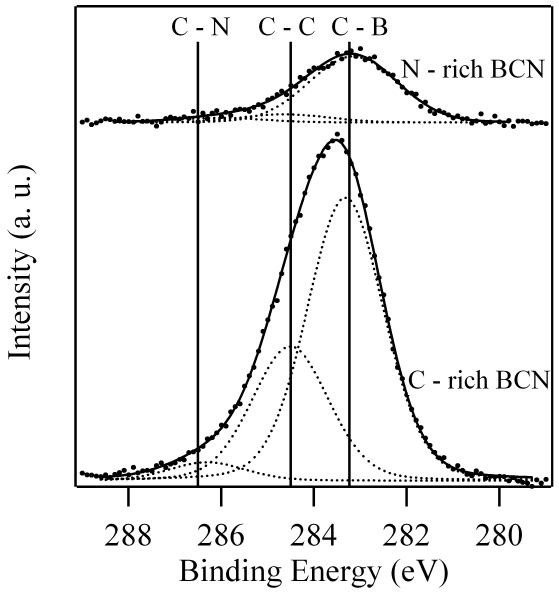

Figure 4.1. Deconvoluted C 1*s* spectra (dashed lines) for N-rich and C-rich BCN film (350 ºC deposition on Si(100)) following 500 s Ar^+ sputter at 5 kV. Solid line shows fit to raw data (dots).

In Fig. 4.2 an Arrhenius plot of the natural logarithm of the BCN deposition rate vs. reciprocal temperature is shown for C-rich and N-rich films on Si(100) and N-rich films on Ge(100). An activation energy for BCN deposition is calculated from the slope. For N-rich BCN deposited on Si(100), the apparent activation energy is 115 kJ/mol. C-rich BCN depositions on Si(100) proceed at a much slower rate, and the calculated activation energy is 258 kJ/mol. When N-rich BCN is deposited on Ge(100), the deposition rate at a given temperature is faster than N-rich depositions at Si(100). But the slope of the Arrhenius plot is similar for these two scenarios, and the calculated activation energy for N-rich BCN on Ge(100) is 116 kJ/mol.

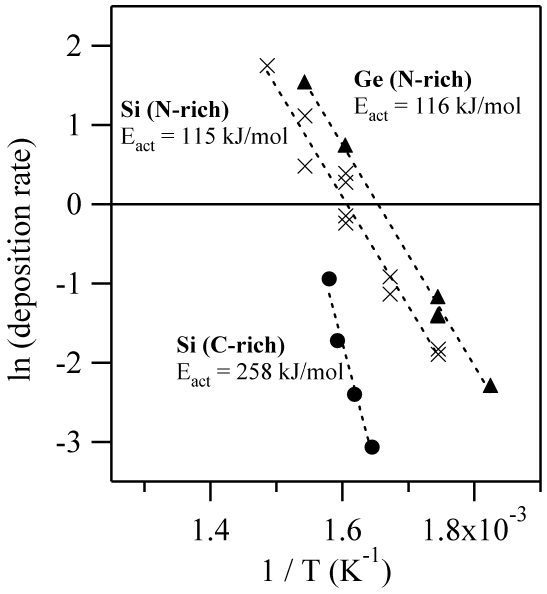

Figure 4.2. Arrhenius dependence of BCN deposition rate on deposition temperature for N-rich BCN on Si(100) and Ge(100) and C-rich BCN on Si(100).

The linear fit for N-rich BCN on Ge(100) is shifted to lower temperatures (higher reciprocal temperatures) by 17.5 º relative to the linear fit of N-rich BCN on Si(100). In a previous study we suggested that radiative heating of Ge(100) was more efficient than Si(100), and therefore the actual Ge(100) substrate temperature was higher than estimated by a temperature calibration experiment performed with Si(100) [30]. Since the activation energies for N-rich BCN deposition on Si(100) and Ge(100) are virtually identical, it is likely that the Ge(100) substrate temperature is ~ 17.5 ºC hotter than the targeted deposition temperature. The remainder of this chapter will continue to report Ge(100) substrate temperatures that are determined from a calibration experiment designed for Si(100) substrates, but it should be noted that the reported temperature likely underestimates the actual deposition temperature.

MIS capacitors consisting of TaN / HfO_2 / BCN / SiO_2 / Si(100) film stacks were constructed with various thicknesses of both C-rich and N-rich BCN. Figure 4.3 shows the *C–V* characteristics of these devices. In Fig. 4.3(a) there is considerable counterclockwise hysteresis for the device with 11.3 nm C-rich BCN. This hysteresis worsens for 15.6 nm BCN (not shown), and becomes even worse for a MIS device containing 35.6 nm C-rich BCN. The N-rich BCN films in Fig. 4.3(b) perform considerably better. There is virtually no hysteresis for a 5.2 nm N-rich film. Though there is measurable hysteresis for 30.4 nm N-rich BCN, it is still considerably less than the hysteresis measured for each of the MIS devices containing C-rich BCN.

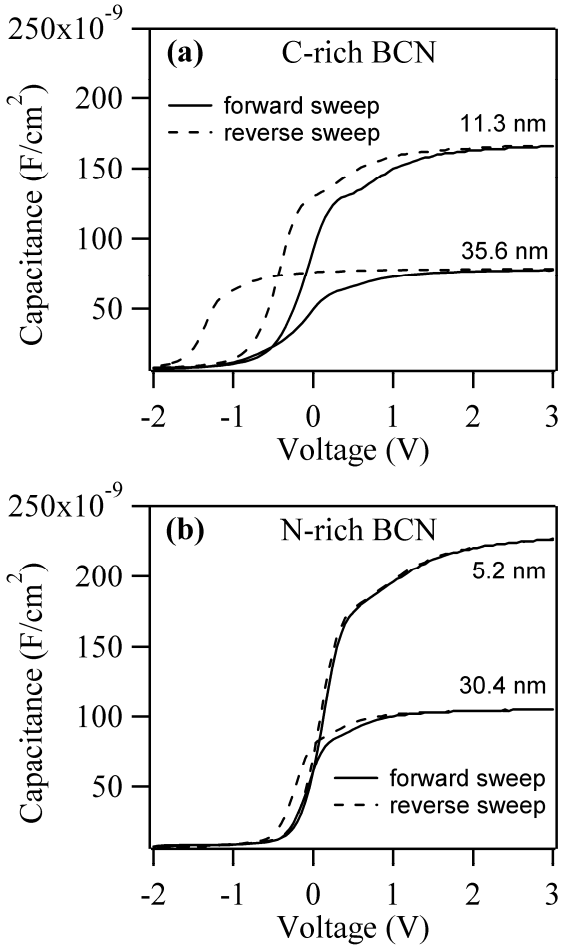

Figure 4.3. TaN / HfO_2 / BCN / SiO_2 / n-Si(100) MIS capacitor *C-V* curves showing hysteresis for (a) C-rich and (b) N-rich BCN. No PDA or PMA was performed for these devices.

Poor *C–V* characteristics were also observed for similar MIS devices containing C-rich BCN deposited on Si(100) substrates. In Fig. 4.4, large positive V_{FB} shifts are observed for these devices on both n- and p-type Si(100). As seen from the difference in 6.7 nm and 9.1 nm BCN, the magnitude of the shift increases with BCN film thickness. Because of the large degree of hysteresis observed in Fig. 4.3(a) and the large V_{FB} shifts in Fig. 4.4, fabrication of MIS devices containing C-rich BCN was abandoned. The remainder of this study addresses only N-rich BCN film properties and MIS devices. It should be noted that none of the MIS devices in Fig. 4.3 or Fig. 4.4 received a PDA or PMA. But the performance of C-rich BCN without any post-deposition treatment was poor enough to warrant focusing on N-rich BCN for future devices, especially considering the low levels of hysteresis for N-rich BCN devices in Fig. 4.3(b).

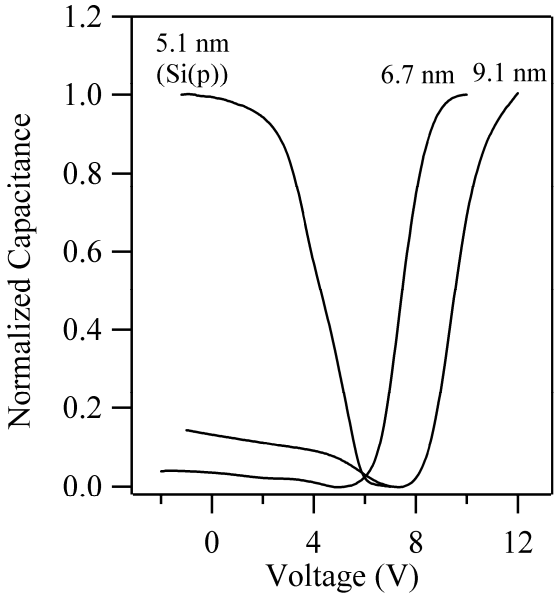

Figure 4.4. *C-V* curves of TaN / HfO_2 / BCN (C-rich) / Si(100) (n- and p-type) MIS capacitors with no PDA or PMA.

Figure 4.5 presents *C–V* and *I–V* characteristics for TaN / HfO_2 / BCN / Si(100) devices. The N-rich BCN films were deposited at temperatures of 325 ºC, 375 ºC, and 400 ºC, and in each case the film thickness was between 4.5 nm and 5 nm. Films of this thickness were chosen because they are known to be continuous [30] and resistant to oxidation of the underlying substrate [31]. Each device received a 5 min PDA in H_2 at 400 ºC following the HfO_2 deposition and a 30 min PMA in H_2 at 300 ºC following the TaN deposition. From Fig. 4.5(a) it is clear that as the BCN deposition temperature decreases, the *C–V* characteristics improve. There is less of a V_{FB} shift for the 325 ºC and 375 ºC BCN films relative to the 400 ºC film. The shape of the *C–V* curve also becomes less stretched along the voltage axis as the deposition temperature decreases, indicating a reduction in the interface trap density [8]. The dashed curve is the reverse sweep for the 325 ºC device. Clockwise hysteresis equal to 0.95 V exists for this device, while 1.90 V hysteresis is observed for the 375 ºC device (not shown). The *I–V* curves in Fig. 4.5(b) show that the gate leakage current density (*J*) is several orders of magnitude lower for the 325 ºC (8×10^{-10} A/cm^2 at 1 V) and 375 ºC (8×10^{-9} A/cm^2 at 1 V) films relative to the 400 ºC film (1×10^{-5} A/cm^2 at 1 V).

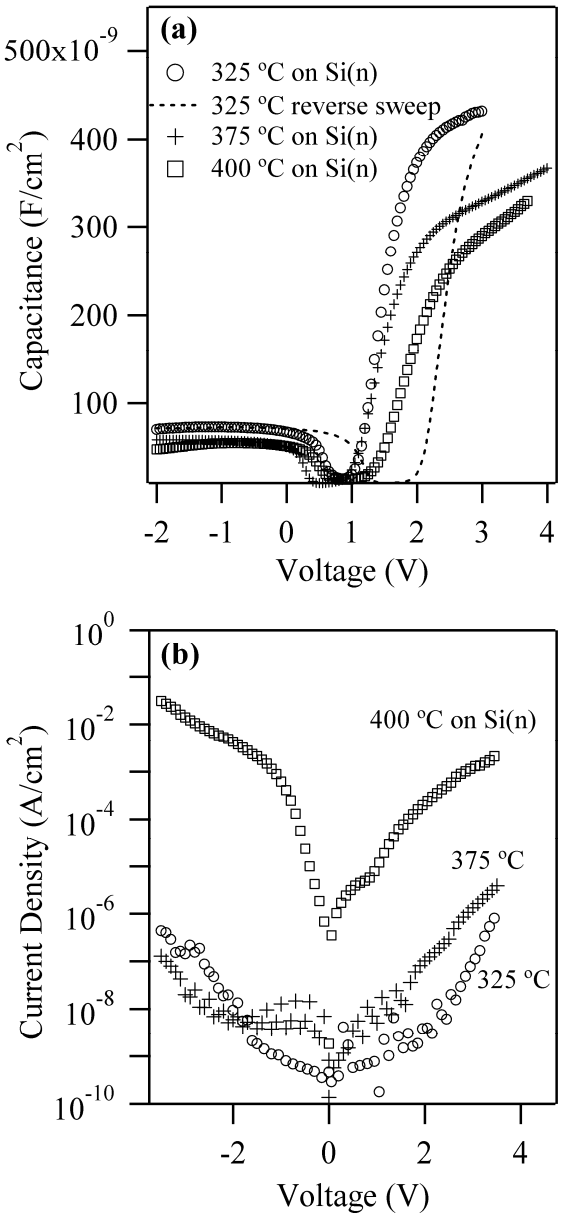

Figure 4.5. (a) *C-V* and (b) *I-V* curves of TaN / HfO_2 / BCN / n-Si(100) MIS capacitors for BCN films deposited at 325 ºC, 375 ºC, and 400 ºC. Devices received PDA and PMA.

Figure 4.6 presents the electrical results for similar MIS devices fabricated on Ge(100) substrates. In this case BCN was deposited at 275 ºC, 300 ºC, and 350 ºC. In Fig. 4.6(a), as the deposition temperature increases, V_{FB} shifts positive, and the *C–V* curves stretch out along the voltage axis. This again indicates an increased interface state density with increasing BCN deposition temperature. The hysteresis of the 275 ºC device is 1.05 V, and for the 300 ºC device (not shown) it is 1.55 V. The *I–V* curves in Fig. 4.6(b) show that the gate leakage current density of the 275 ºC device (7×10^{-8} A/cm^2 at 1 V) was several orders of magnitude lower than that of the 300 ºC film (2×10^{-3} A/cm^2 at 1 V). The leakage current of the device incorporating 350 ºC BCN was not tested because of the poor *C–V* characteristics of that sample. The results presented in Fig. 4.6 are for devices that received a PDA following HfO_2 deposition, but no PMA was performed. *C–V* and *I–V* measurements were also made for the same samples following a PMA (not shown). Regardless of deposition temperature, each device exhibited leakage currents similar to the 300 ºC sample in Fig. 4.6(b). And the *C–V* curves were similar to and often worse than the 350 ºC sample in Fig. 4.6(a). The devices receiving a PMA would often experience dielectric breakdown at voltages ranging from 2–3 V during testing.

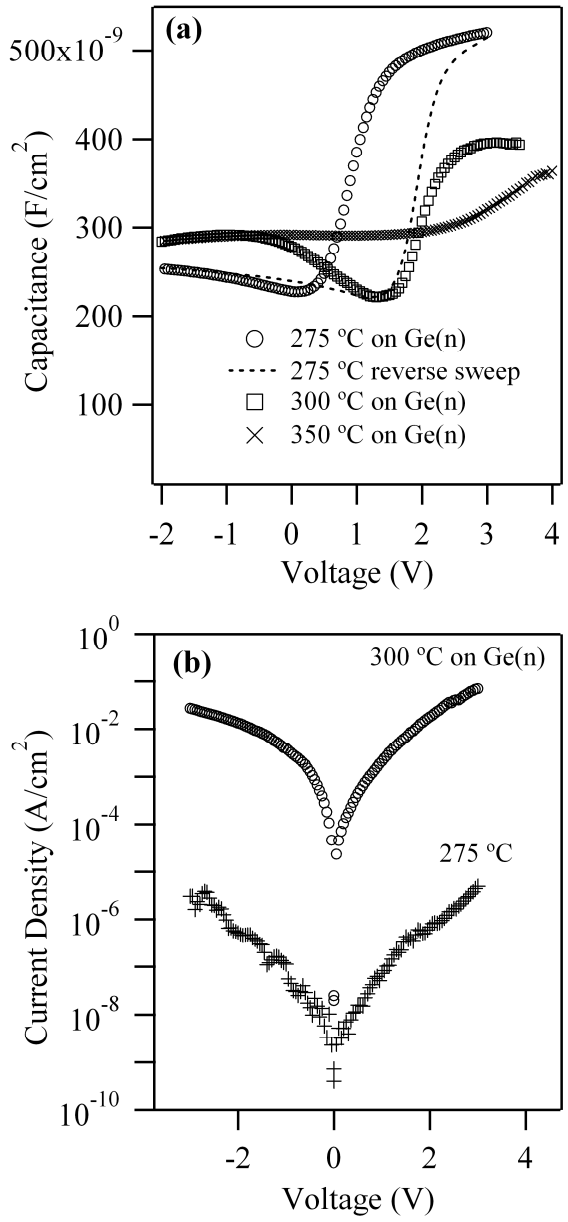

Figure 4.6. (a) *C-V* and (b) *I-V* curves of TaN / HfO_2 / BCN / n-Ge(100) MIS capacitors for BCN films deposited at 275 ºC and 300 ºC. Devices received PDA but no PMA.

To more closely examine the current leakage mechanism for the devices in Figs. 4.5(b) and 6(b), the ln (*J/E*) is plotted vs. $E^{1/2}$ (where *E* is the electric field across the insulator stack) in Fig. 4.7 for each of the MIS devices on Si(100) and Ge(100) substrates. There is a threshold electric field for each device where the relationship becomes linear, indicating Frenkel-Poole emission of trapped electrons [8]. For BCN-passivated Si(100) devices, this transition to linearity occurs at approximately 1.30 $MV^{1/2}$ $cm^{-1/2}$, 1.08 $MV^{1/2}$ $cm^{-1/2}$, and 0.97 $MV^{1/2}$ $cm^{-1/2}$ for 325 ºC, 375 ºC, and 400 ºC deposition temperatures, respectively. On Ge(100) devices, the transition occurs at 0.60 $MV^{1/2}$ $cm^{-1/2}$ and 0.49 $MV^{1/2}$ $cm^{-1/2}$ for 275 ºC and 300 ºC depositions, respectively.

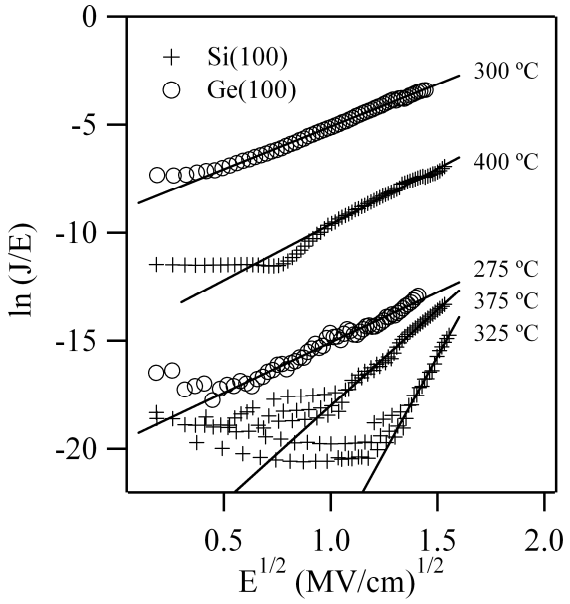

Figure 4.7. Frenkel-Poole emission plot of ln (*J/E*) vs. $E^{1/2}$ for MIS capacitors on BCN-passivated n-Si(100) and n-Ge(100) at various BCN deposition temperatures.

The influence of deposition temperature on uptake of O by BCN was examined by XPS depth profiling. Thicker (15–25 nm) BCN films deposited on Si(100) and Ge(100) substrates were left in ambient for times ranging from 2–35 d, and depth profiles were performed by alternating 2 kV Ar^+ sputter sequences with XPS analysis. The atomic % O as a function of sputter time is plotted in Fig. 4.8. The sputter rate of several films was estimated by first measuring the XPS peak attenuation thickness of BCN material remaining after several sputter cycles. This was subtracted from the original thickness before sputtering and divided by the sputter time to give a sputter rate of 0.28 ± 0.05 (one standard deviation) nm/min. No clear correlation between sputter rate and deposition temperature was observed. Based on this sputter rate, 1000 s of sputtering removes ~ 4.7 nm of BCN.

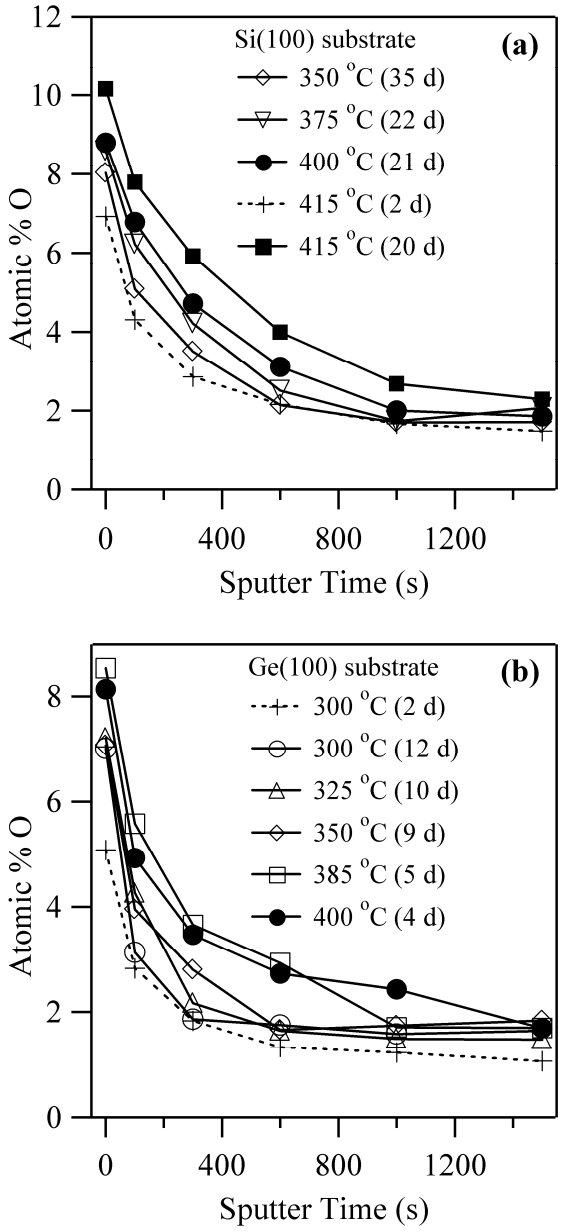

Figure 4.8. XPS depth profile tracking atomic % O in BCN films deposited on (a) Si(100) and (b) Ge(100) at various temperatures and left in ambient for various times.

In Fig. 4.8(a) there is a clear correlation between BCN deposition temperature and the rate of O incorporation in the film. After 35 d of ambient exposure, the atomic % O in BCN deposited at 350 ºC ranges from 8% at the ambient interface to < 2% after 1000 s of sputtering. For reference, *in situ* XPS analysis immediately after BCN deposition (not shown) reveals < 2% O in the film. A 375 ºC film after 22 d ambient exposure ranges from 8.6% O at the surface to < 2% after 1000 s of sputtering. 400 ºC and 415 ºC films range from 8.8% to 2% and 10.2% to 2.7%, respectively, after similar ambient exposure times. The depth profile of the same 415 ºC film after just 2 d of ambient exposure (6.9% O to < 2% O) is included to illustrate how the oxygen uptake in this film progresses with ambient exposure.

Similar results are obtained for BCN on Ge(100) substrates, as shown in Fig. 4.8(b). Shorter ambient exposure times were studied in this case to better demonstrate how the O incorporation penetrates deeper into the film for higher temperature depositions. A 300 ºC film exposed for 12 d reaches < 2% O after just 300 s of sputtering, whereas a 400 ºC film exposed for just 4 d requires 1500 s of sputtering to reach the same % O level. The intermediate temperatures follow a similar trend. 325 ºC BCN (10 d ambient) drops below 2% O after 600 s of sputtering. 350 ºC also contains < 2% O after 600 s sputtering, but it does so in less ambient exposure time (9d). And 385 ºC BCN exposed for 5 d requires 1000 s of sputtering to reach the background level of O in the BCN.

Figure 4.9 shows the B 1*s*, C 1*s*, N 1*s*, and O 1*s* XP spectra for the 415 ºC BCN film from Fig. 4.8(a) after 2 d (solid line) and 20 d (dashed line) ambient exposure. The spectra were taken after 100 s of 2 kV Ar^+ sputtering. The arrows in Fig. 4.9(a–c) indicate the lowest binding energy that would be expected from O bond formation with each of the elements (192.1 eV for B 1*s*, 286.1 eV for C 1*s*, and 402.0 eV for N 1*s*) [32].

The B 1*s* spectrum undergoes a subtle shift to higher binding energy, indicating the presence of more B–O bonding in this sample after 20 d of ambient exposure. The C 1*s* and N 1*s* spectra do not appear to shift to binding energies representative of O bonding, suggesting much lower (if any) C–O and N–O bond formation in this sample with increased ambient exposure.

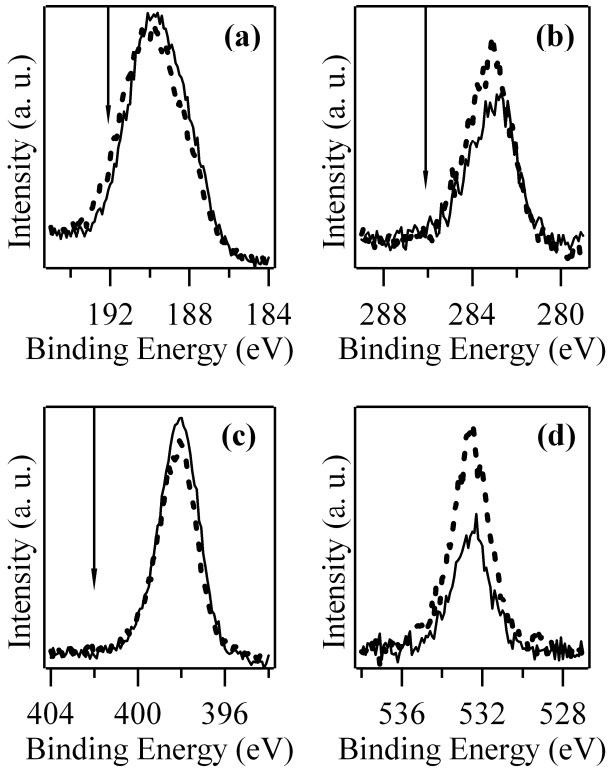

Figure 4.9. (a) B 1*s*, (b) C 1*s*, (c) N 1*s*, and (d) O 1*s* XP spectra for BCN grown at 415 ºC on Si(100) and exposed to ambient for 2 d (solid lines) and 20 d (dashed lines). Arrows indicate the lowest expected binding energy for O bond formation with each of the elements. Spectra were taken after 100 s of 2 kV Ar^+ sputtering.

A temperature dependence of BCN film stoichiometry was also observed. Figure 4.10 shows how the N:B and C:B (after removing adventitious surface C with 100 s of Ar^+ sputtering at 2 kV) atomic ratios increase with increasing deposition temperature. Films deposited at 300 ºC on Si(100) are $BC_{0.10}N_{0.38}$ stoichiometry. As the temperature increases, the relative amount of B in the films decreases in favor of increased N and C. At 415 ºC, films of $BC_{0.14}N_{0.49}$ stoichiometry are deposited. Deposition on Ge(100) substrates reveal slightly higher N:B ratios at each temperature. But this is attributed to an underestimation of the actual Ge(100) substrate temperature during BCN deposition, as was discussed above.

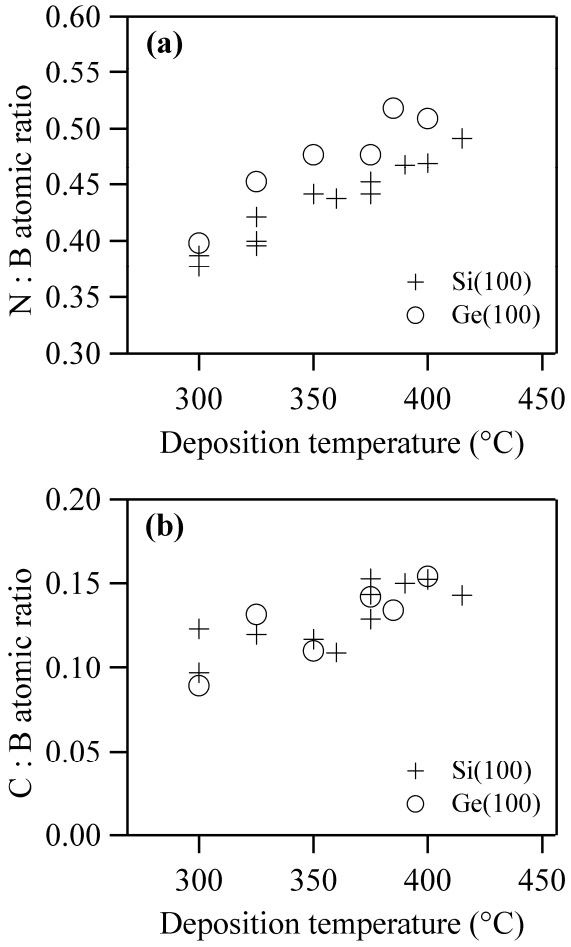

Figure 4.10. (a) N:B and (b) C:B atomic ratio of BCN films as a function of deposition temperature. The C:B ratio was calculated after a 100 s Ar^+ sputter at 2 kV to remove the contribution from adventitious C on the surface.

Thick BCN films were optically characterized using spectroscopic ellipsometry measurements to determine temperature dependent changes in the extinction coefficient, *k*, and refractive index, *n*. Figure 4.11(a) shows that BCN films deposited on Si(100) at higher temperatures have a higher absorption coefficient (α), which was calculated from *k*, for photon energies ($h\upsilon$) greater than 3 eV. A similar trend is observed for BCN on

Ge(100), except the temperature dependence of α exists for photon energies greater than 2.2 eV. The optical band gap, E_g, of BCN was extracted from the absorption coefficient plots following a procedure outlined for amorphous films [35]. For each substrate $(\alpha h\upsilon)^{1/2}$ vs. $h\upsilon$ was plotted, and E_g was estimated from the x-intercept of a fit to the linear portion of the graph. Figure 4.12 shows the graphically-determined values of E_g for BCN deposited on Si(100) and Ge(100) substrates. The BCN band gap for 300 ºC deposition on Si(100) is 3.56 eV, and it linearly decreases to 3.25 eV for a 400 ºC film. The same trend is observed for Ge(100) substrates, with measured E_g values ranging from 3.55 eV (275 ºC) to 3.26 eV (375 ºC). Linear fits to the E_g values in Fig. 4.12 have similar slopes for Si(100) and Ge(100) substrates (-0.003 eV / ºC and -0.0029 eV / ºC, respectively). If the fit to the Ge(100) data is shifted 16.7 ºC on the temperature axis, the measured band gaps on each substrate would closely overlap. This temperature offset is in very close agreement with the 17.5 ºC difference observed for the Arrhenius-dependent deposition rate fits for Si(100) and Ge(100) substrates in Fig. 4.2. Therefore it is likely that the lower band gaps observed for BCN on Ge(100) substrates is again attributed to an underestimation of the Ge(100) substrate temperature by ~ 17ºC.

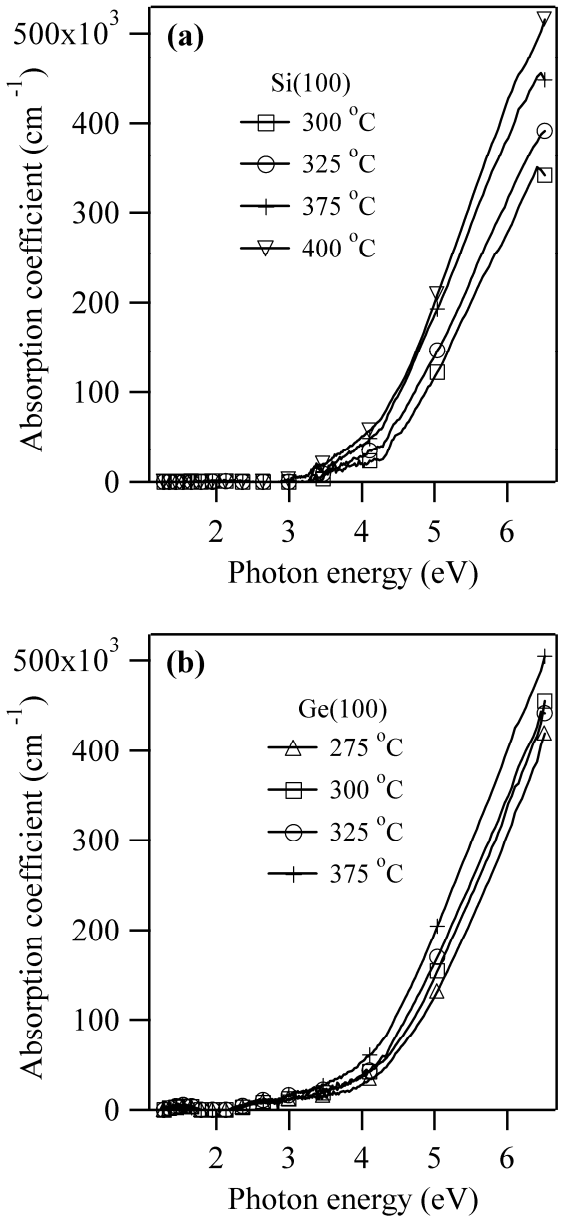

Figure 4.11. Absorption coefficient of BCN films deposited on (a) Si(100) and (b) Ge(100) substrates at various temperatures.

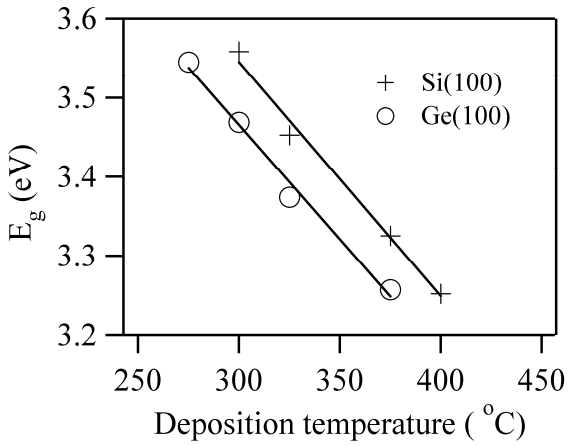

Figure 4.12. Optical band gap of BCN films deposited on (a) Si(100) and (b) Ge(100) substrates at various temperatures.

Figure 4.13 shows the dependence of the refractive index on deposition temperature for Si(100) substrates. The refractive index increases with an increase in deposition temperature. At 633 nm, the measured value of *n* is 1.76, 1.86, 1.90, and 1.94 for BCN films deposited at 300 ºC, 325 ºC, 375 ºC, and 400 ºC, respectively. A similar trend was observed for BCN on Ge(100) substrates, with *n*(633 nm) ranging from 1.84 at 275 ºC to 1.90 at 375 ºC.

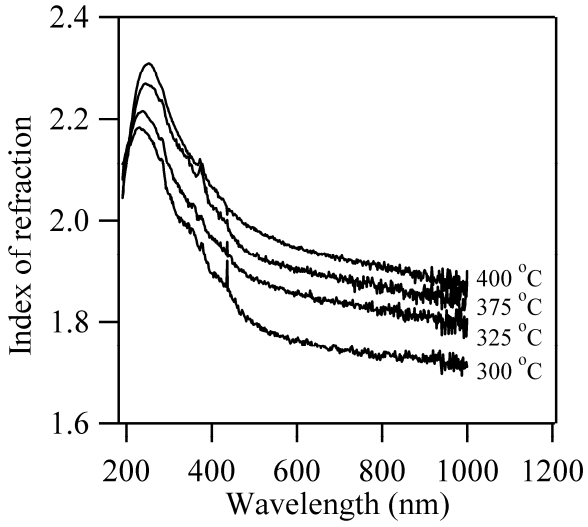

Figure 4.13. Index of refraction of BCN films deposited on Si(100) substrates at various temperatures. Films on Ge(100) follow a similar trend (not shown).

4.4. DISCUSSION

The counterclockwise hysteresis observed for C-rich BCN MIS capacitors in Fig. 4.3(a) suggests there are more donor type (positive) trapping centers in this stochiometry than in N-rich BCN. This could possibly be due to incomplete bonding within the amorphous C-rich BCN. The significantly higher activation energy for deposition of C-rich BCN (258 kJ/mol) compared to N-rich BCN (115 kJ/mol) in Fig. 4.2 may explain this. It is likely that the less reactive C_2H_4 is not as efficient at tying up dangling bonds during film growth as the NH_3 is. These unsatisfied bonds then become sites for charge trapping, contributing to the hysteresis.

When C-rich BCN was deposited directly on Si(100) with no intermediate SiO_2 layer, significant positive V_{FB} shifts were observed (Fig. 4.4). The presence of such a shift on both n- and p-type substrates suggests that the C-rich BCN film contains fixed

negative charge [8]. And because the magnitude of the V_{FB} shift increases for thicker BCN, the fixed charge is distributed throughout the bulk of the BCN and not confined just to the Si(100) interface. Gauss' law (Eqn. 4.2) describes the magnitude of a V_{FB} shift for a MIS capacitor:

$$\Delta V_{FB} = -\frac{1}{C_i}\left[\frac{1}{d}\int_0^d x\rho(x)dx\right] \tag{4.2}$$

where C_i is the dielectric capacitance, d is the dielectric layer thickness, x is the location within the dielectric (equal to zero at the metal interface and equal to d at the semiconductor interface), and $\rho(x)$ is the charge density per unit volume [8]. If $\rho(x)$ is constant, as might be expected for a CVD process where the deposition conditions remain constant throughout film growth, then ΔV_{FB} would be proportional to d. This would explain the larger shift seen for 9.1 nm BCN in Fig. 4.4. Shifts in V_{FB} were not observed for the MIS devices in Fig. 4.3. This is because the magnitude of ΔV_{FB} in Eqn. 2 is also weighted according to the location of the fixed charge. The closer the charge is to the semiconductor interface, the greater its influence on the V_{FB} shift. The MIS devices in Fig. 4.3 had a 10.7 nm thermal SiO_2 insulator between the BCN and the Si(100), which shielded the charge carriers in the semiconductor from the fixed negative charge in the BCN.

The higher density of fixed negative charge in C-rich BCN relative to the N-rich films may stem from the greater % C in the film, which has the ability to sp^2 hybridize and delocalize charge. Zhu *et al*. have attempted to deconvolute the sp^2 and sp^3 contributions to the C 1*s* XP spectra [36]. However, the 0.8 eV difference between sp^2 C (284.3 eV) and sp^3 C (285.1 eV) that they report is difficult to deconvolute, especially without a monochromatic x-ray source. Furthermore, Speranza *et al*. have recently

questioned the peak contributions proposed by Zhu, and they concluded that quantifying sp^2 vs. sp^3 hybridization using XPS is very complex [37]. This study does not attempt to deconvolute the contributions from the two C hybridizations. But if sp^2-hybridized C is present in BCN, it will likely show up as a contribution to the C–C bonding feature at 284.5 eV in the deconvoluted C 1*s* spectra in Fig. 4.1. Table 4.1 shows that C–C bonding constitutes 31% of the entire C 1*s* spectrum for C-rich BCN, whereas the deconvoluted C 1*s* spectrum for N-rich BCN contains only 10% C–C bonding character. This coupled with the fact that C-rich BCN contains 35% C compared to N-rich BCN's 8% C suggests there is a greater chance for sp^2-hybridized C to exist in the C-rich BCN. This could explain the presence of fixed negative charge in these films. Furthermore, Speranza *et al*. also argue that the component at 285.1 eV is not necessarily solely attributed to sp^3-hybridized C, but it could also be from unsaturated C atoms with dangling bonds [37]. This would support the witnessed hysteresis caused by trapping states in Fig. 4.3(a).

The MIS devices containing N-rich BCN on Si(100) in Fig. 4.5 also exhibited hysteresis. While the minor hysteresis observed for N-rich BCN on SiO_2 / Si(100) in Fig. 4.3(b) was counterclockwise, the clockwise hysteresis on Si(100) suggests that acceptor type traps (negative when populated) also exist in the film. The observation of this in Fig. 4.5(a) is due to the fact that BCN and the n-type Si(100) substrate share an interface. Upon positive biasing of the MIS device, electron injection from the Si(100) into the BCN populates the acceptor traps, leading to counterclockwise hysteresis during the reverse voltage sweep. In Fig. 4.3(b), the 10.7 nm SiO_2 layer prevents population of BCN's acceptor type traps by electron injection, and therefore the clockwise hysteresis is not observed for these devices. But there are enough donor type traps (positive when populated) in the 30.4 nm BCN layer to produce a small amount of counterclockwise hysteresis. This is due to population of the donor type traps by electron injection from

the BCN into the positively biased TaN gate (or hole injection from the gate), which shares an interface with BCN in this device.

As the BCN deposition temperature increases, increased hysteresis and deterioration of other electrical characteristics (including greater V_{FB} shift, stretching of the *C–V* curve along the voltage axis, and increased gate leakage current) are observed for MIS devices on Si(100) and Ge(100) (Figs. 4.5 and 4.6, respectively). This may be attributed to increased defects within the BCN and at the semiconductor interface, due to accelerated growth rates at higher temperatures. As the deposition temperature increases, the rate of surface reactions accelerates. When this happens it may be possible that the film grows vertically at a fast enough rate that some of the bonding at the semiconductor interface and within the BCN is left incomplete. This would result in a higher density of bulk and interfacial defects that would serve as trapping centers. These traps contribute to the increased hysteresis that was observed for devices fabricated from higher temperature BCN growths. The higher density of interface states, as indicated by the stretch out of the *C–V* curves, would also be explained by the poor bonding of BCN with the Si(100) or Ge(100) substrate that is exacerbated by higher deposition rates. The greater V_{FB} shifts at higher temperatures may be due to the increased C content in these N-rich films at higher deposition temperatures, as was seen in Fig. 4.10(b).

If a greater density of defects is present, trap-assisted tunneling could also explain the enhanced leakage current that was observed for BCN films grown at higher temperature. In Fig. 4.7 it was observed that the electric field threshold for Frenkel-Poole emission of trapped electrons decreased with increasing deposition temperature for both substrates. This indicates that as BCN deposition temperature increases, trap-assisted tunneling of electrons becomes the dominant leakage current mechanism. Therefore BCN films deposited at higher temperatures are likely to have increased traps or defects.

The decrease in E_g with increasing temperature (Fig. 4.12) also explains the increased susceptibility to gate leakage, because dielectric materials with high defect densities are more susceptible to tunneling of charge carriers.

The exact chemical nature of the defects in bulk BCN is unknown. It can be said that as the temperature increases there are changes in the relative amounts of B, C, and N and the ways in which they bond to one another. Figure 4.10 revealed that greater amounts of C and N were substituted for B at higher deposition temperatures. And the increase in index of refraction with increasing deposition temperature (Fig. 4.13) suggests that the higher temperature films are denser. This indicates that the constituent bonding profiles within bulk BCN are changing at higher temperatures. Attempting to use these changes in the BCN material properties to speculate on the nature of the defect sites is difficult. This is partially due to the fact that this material is an amorphous mixture of multiple elements that are capable of several bonding states. For example, the bonding orbitals of both C and N can undergo multiple hybridizations, which creates the possibility of single, double, and even triple bonds within BCN. This increased complexity of the material system hinders efforts to identify the defects that affect BCN's electrical characteristics.

One BCN material property that does correlate with electrical performance is the increased O uptake that occurs at higher BCN deposition temperatures (Fig. 4.8). This observation may be explained by the increased density of bulk defects at higher temperatures, which are more susceptible to oxidation than the satisfied bonds within the film. If BCN were free of defects, it would be expected that films with higher B content (lower deposition temperature according to Fig. 4.10) would more readily oxidize. This is because the relative strengths of bonds containing B are much lower than the possible BCN bonding states that do not involve B. It is likely that oxidation would more readily

facilitate cleavage of the weak B–B (290 kJ/mol), B–N (378 kJ/mol), or even B–C (448 kJ/mol) bonds instead of the stronger C–C (618 kJ/mol) or N–C (750 kJ/mol) bonds [38]. And formation of B–O (809 kJ/mol) bonding upon oxidation would be a stable arrangement based on these bond strengths. Indeed, Aoki *et al.* have reported that the O_2 plasma etching rate of BCN films increases as the amount of B in the film increases, though these films were deposited from BCl_3, CH_4, and N_2 in a plasma-assisted process [39]. The fact that the BCN films deposited in our laboratory are more susceptible to O uptake when the % B is lower suggests that an alternative mechanism is responsible for the observed increase in % O. Perhaps the O incorporation is not due to the breaking of existing B-, C-, or N-containing bonds upon ambient exposure, but rather to oxidation of defect sites within BCN. It is easier to oxidize a dangling bond than it is to cleave the relatively weak B–B bond. Figure 4.9 revealed a slight increase in the binding energy of B 1*s* following increased ambient exposure, while C 1*s* and N 1*s* were relatively unchanged. This suggests that the O uptake may be occurring at B atoms with unsatisfied bonding arrangements. O uptake by moisture absorption, which has been attributed to increased device hysteresis [12], cannot be ruled out, however. O incorporation by this mechanism probably would not result in a significant higher binding energy shift in the XP spectra, therefore moisture uptake at C or N defect sites remains a possibility. But the increase in O uptake with increasing deposition temperature that was observed in Fig. 4.8 does support the presence of higher levels of bulk defects in these films, which translates to poor electrical performance.

Comparison of *C–V* characteristics in Figs. 4.5 and 4.6 reveals that MIS devices on Si(100) perform better than devices on Ge(100). Though the 275 ºC device in Fig. 4.6(a) had acceptable electrical characteristics with just a PDA, these were lost during the 30 min 300 ºC H_2 PMA that all of the Si(100) devices in Fig. 4.5 received. Matsubara *et*

al. observed a similar deterioration in electrical characteristics (in the form of increased interface state density) for thermally oxidized Ge(100) MIS structures when subjected to a PMA ≥ 300 ºC [15]. Part of the poorer Ge(100) device performance may be attributed to interfacial differences between BCN on Ge(100) compared to Si(100). The absorption coefficient data in Fig. 4.11 revealed a longer absorption tail at low photon energies for BCN on Ge(100) (measurable absorption beginning at 2.2 eV) compared to BCN on Si(100) (measurable absorption beginning at 3 eV). This higher sub-band gap absorption may be due to more defect states at the BCN–Ge(100) interface than at the BCN–Si(100) interface. As the BCN deposition temperature decreases, the amount of sub-band gap absorption decreases as well. This suggests that lower temperature depositions create fewer interfacial defects, which is consistent with the improvement in electrical performance witnessed for devices at lower BCN deposition temperatures.

The Frenkel-Poole emission plot in Fig. 4.7 also suggests that higher interface state densities exist at the BCN–Ge(100) interface compared to BCN–Si(100). On Ge(100) substrates the electric field threshold for Frenkel-Poole emission was significantly lower at both deposition temperatures (0.60 $MV^{1/2}$ $cm^{-1/2}$ at 275 ºC and 0.49 $MV^{1/2}$ $cm^{-1/2}$ at 300 ºC) than for even the 400 ºC deposition on Si(100) (0.97 $MV^{1/2}$ $cm^{-1/2}$). A 17 ºC underestimation of the Ge(100) substrate temperature is incapable of explaining this difference in the leakage current mechanism. Since the bulk properties of BCN on Si(100) and Ge(100) are likely identical, a higher level of interface traps at the Ge(100) interface would explain the trap-assisted tunneling that is more prevalent in BCN-passivated Ge(100) devices.

Differences in the way BCN forms its interface with Ge(100) compared to Si(100) may explain the higher density of interface states that is observed for Ge(100). Many have reported that nitridation of a semiconductor interface improves electrical

performance by reducing the number of interface states [17,19,20,22]. Most nitridation approaches for Ge(100) substrates utilize a NH_3 or N_2 plasma environment [17,22] or a high temperature (> 500 ºC) thermal environment [19,20] to create the Ge–N interfacial bonds. The approach in this study is to deposit a N-rich BCN passivation film at the Ge(100) or Si(100) substrate through the use of NH_3 coreactant gas in a low temperature (≤ 400 ºC) thermal CVD environment. Aubel *et al*. discovered that while NH_3 readily dissociates into $–NH_2$ and –H passivating species on Si(100), adsorption of NH_3 on Ge(100) is non-dissociative at temperatures as high as 600 ºC. They attribute the relative inertness of Ge(100) to nitridation to the difference in the formation enthalpies of Si_3N_4 (-741 kJ/mol) and Ge–N (-63 kJ/mol) [40]. At the range of CVD temperatures employed in this study (275–400 ºC), it is unlikely that the NH_3 coreactant participates in the initial stages of BCN growth at the Ge(100) surface. This suggests that while the Si(100) devices may contain Si–N bonds that help to reduce the interface state density, Ge(100) devices are more B-rich at the Ge(100) interface. Once the BCN film is nucleated on the Ge(100) substrate, participation of the NH_3 coreactant in further film growth is expected to behave the same as it would on Si(100) substrates. But the proposed lack of Ge–N interfacial bonding could result in higher interface state densities, which would explain the higher sub-band gap absorption and the worse electrical characteristics for BCN-passivated Ge(100).

Another reason that the Si(100) MIS devices outperform the Ge(100) devices may be due to the higher sensitivity of Ge to band alignment with the BCN passivation film and HfO_2 dielectric. Lucovsky *et al.* have recently explained the poor electrical characteristics of MIS devices on n-type Ge [41]. They propose that when a Ge-based interfacial transition layer (ITL), such as GeO_2 or Ge_3N_4, is used between the HfO_2 and Ge, a potential well that serves as an electron trap is formed at the HfO_2–ITL interface.

Upon positive biasing of the gate, electron injection from the substrate and Fowler-Nordheim tunneling through the ITL will populate the trap. The reason for the tunneling is the small conduction band offset between Ge and the ITL (~1.5 eV for both GeO_2 and Ge_3N_4). The reason for the potential well formation is that this Ge–ITL conduction band offset is less than the conduction band offset between Ge and HfO_2 (~ 2.0 eV). Therefore, when positive gate bias is applied, the bands are misaligned at the HfO_2–ITL interface and a potential well forms.

The BCN films deposited in this study have even lower band gaps (3.26–3.55 eV) than the GeO_2 (5.5 eV) and Ge_3N_4 (4.4 eV) in Lucovsky *et al*.'s study. It is therefore reasonable to suspect that the conduction band offset between Ge and BCN will be much smaller than the 2.0 eV offset between Ge and HfO_2. Therefore the threshold voltage for electron injection into the BCN film from the substrate will be lower. This may explain the high leakage current observed for 300 ºC BCN in Fig. 4.6(b). Even the 275 ºC BCN film reveals immediate injection of electrons with increasing voltage, though the observed current density is lower. The improved leakage characteristics may be attributed to the larger band gap of 275 ºC BCN, but the conduction band offset is likely still too low to prevent electron injection. The 325 ºC BCN MIS device on Si (100) in Fig. 4.5(b) shows that electron injection does not occur until a gate voltage of ~ 2 V is applied. Lucovsky *et al*. report that the Si and HfO_2 conduction band offset is 1.8 eV, which is lower than the Ge and HfO_2 conduction band offset [41]. This lower conduction band offset on Si substrates may make the formation of a potential well at the HfO_2–BCN interface less likely for these devices than for MIS devices containing Ge (100). This would help to enhance the electrical performance of BCN-passivated Si(100) MIS devices compared to similar Ge(100) structures. A detailed analysis of the band offsets between BCN and Ge(100) and HfO_2 is beyond the scope of this study. But the

sensitivity of Ge MIS devices to this alignment is presented as a possible additional explanation for the poor performance of BCN-passivated Ge(100).

4.5. SUMMARY AND CONCLUSIONS

The *C–V* and *I–V* characteristics of MIS capacitors containing HfO_2 dielectric deposited on Ge(100) (n-type) and Si(100) (n-type) passivated with 4.5–5 nm of N-rich BC_xN_y ($0.09 \leq x \leq 0.15$, $0.38 \leq y \leq 0.52$) were measured. BCN deposition temperatures ranging from 275–400 ºC were tested, and an improvement in the electrical characteristics (less hysteresis, less V_{FB} shift, less *C–V* stretch out, and lower leakage current) was observed as the deposition temperature decreased. This was attributed to a decreasing density of bulk and interfacial defects in BCN grown at lower deposition rates, with an Arrhenius relationship between growth rate and temperature observed. The higher level of defects in higher temperature BCN growths is supported by XPS depth profile experiments, which reveal higher rates of ambient O uptake (likely at bulk defect sites) for high temperature growths. Deteriorating electrical properties can also be explained by a decrease in the optical band gap of BCN with decreasing deposition temperature, again possibly related to increased defect densities. C-rich $BC_{0.61}N_{0.08}$ films were also briefly studied, but the effort was abandoned in favor of N-rich films due to large amounts of hysteresis and high levels of fixed negative charge observed for C-rich BCN MIS devices on SiO_2 / Si(100) and Si(100) substrates, respectively.

In general, MIS devices consisting of BCN-passivated Si(100) outperformed BCN-passivated Ge(100) devices. It is speculated that a difference in the interfacial properties of BCN on Si(100) and Ge(100) due to the relative inertness of Ge(100) to thermal nitridation could be the cause. The heightened sensitivity of n-type Ge(100) to band gap alignment issues involving BCN and HfO_2 could also be a factor.

Though reduction of BCN growth temperature improves the electrical performance of MIS capacitors, it is unlikely that the material would serve well as a passivation film for Ge(100). The low band gap of BCN makes the material susceptible to leakage, and the relatively thick (~ 4 nm) layer needed for continuous substrate coverage [30] and oxidation resistance [31] would undesirably increase the EOT due to a decrease in the effective κ value for the dielectric stack. While device performance on Si(100) substrates was improved with a 5 min 400 ºC H_2 PDA and a 30 min 300 ºC H_2 PMA, devices on Ge(100) substrates performed best when only a PDA was performed. The PMA produced high leakage current devices, with poor *C–V* characteristics and a propensity to breakdown at low voltages (< 3V). This suggests that BCN-passivated Ge(100) devices could not withstand the thermal budget experienced during CMOS device processing. While earlier studies have indicated that this material forms a good interface with Ge(100) [30] and protects it from oxidation [31], the present work shows that BCN does not behave well electrically.

4.6. REFERENCES

[1] S. Van Elshocht, M. Caymax, T. Conard, S. De Gendt, I. Hoflijk, M. Houssa, F. Leys, R. Bonzom, B. De Jaeger, J. Van Steenbergen, W. Vandervorst, M. Heyns, and M. Meuris, Thin Solid Films **508**, 1 (2006).

[2] M. Houssa, G. Pourtois, B. Kaczer, B. De Jaeger, F. E. Leys, D. Nelis, K. Paredis, A. Vantomme, M. Caymax, M. Meuris, and M. M. Heyns, Microelectron. Eng. **84**, 2267 (2007).

[3] C. H. Lee, T. D. Lin, L. T. Tung, M. L. Huang, M. Hong, and J. Kwo, J. Vac. Sci. Technol. B **26**, 1128 (2008).

[4] K. Saraswat, C. O. Chui, T. Krishnamohan, D. Kim, A. Nayfeh, and A. Pethe, Mater. Sci. Eng., B **135**, 242 (2006).

[5] G. Nicholas, D. P. Brunco, A. Dimoulas, J. Van Steenbergen, F. Bellenger, M. Houssa, M. Caymax, M. Meuris, Y. Panayiotatos, and A. Sotiropoulos, IEEE Trans. Electron Devices **54**, 1425 (2007).

[6] A. Ritenour, A. Khakifirooz, D. A. Antoniadis, R. Z. Lei, W. Tsai, A. Dimoulas, G. Mavrou, and Y. Panayiotatos, Appl. Phys. Lett. **88** (2006).

[7] W. P. Bai, N. Lu, A. Ritenour, M. L. Lee, D. A. Antoniadis, and D. L. Kwong, IEEE Electron Device Lett. **27**, 175 (2006).

[8] S. M. Sze and K. K. Ng, *Physics of Semiconductor Devices*, 3rd ed. (John Wiley & Sons, Inc., Hoboken, N.J., 2007).

[9] K. Prabhakaran and T. Ogino, Surf. Sci. **325**, 263 (1995).

[10] P. W. Loscutoff and S. F. Bent, Annu. Rev. Phys. Chem. **57**, 467 (2006).

[11] R. H. Kingston, J. Appl. Phys. **27**, 101 (1956).

[12] D. W. Wang, Y. L. Chang, Q. Wang, J. Cao, D. B. Farmer, R. G. Gordon, and H. J. Dai, J. Am. Chem. Soc. **126**, 11602 (2004).

[13] D. W. Wang, Q. Wang, A. Javey, R. Tu, H. J. Dai, H. Kim, P. C. McIntyre, T. Krishnamohan, and K. C. Saraswat, Appl. Phys. Lett. **83**, 2432 (2003).

[14] M. Caymax, M. Houssa, G. Pourtois, F. Bellenger, K. Martens, A. Delabie, and S. Van Elshocht, Appl. Surf. Sci. **254**, 6094 (2008).

[15] H. Matsubara, T. Sasada, M. Takenaka, and S. Takagi, Appl. Phys. Lett. **93** (2008).

[16] X. F. Zhang, J. P. Xu, C. X. Li, P. T. Lai, C. L. Chan, and J. G. Guan, Appl. Phys. Lett. **92** (2008).

[17] T. Sugawara, Y. Oshima, R. Sreenivasan, and P. C. McIntyre, Appl. Phys. Lett. **90** (2007).

[18] M. S. Rahman, E. K. Evangelou, I. I. Androulidakis, A. Dimoulas, G. Mavrou, and P. Tsipas, J. Vac. Sci. Technol. B **27**, 439 (2009).

[19] H. Kim, P. C. McIntyre, C. O. Chui, K. C. Saraswat, and M.-H. Cho, Appl. Phys. Lett. **85**, 2902 (2004).

[20] N. Lu, W. Bai, A. Ramirez, C. Mouli, A. Ritenour, M. L. Lee, D. Antoniadis, and D. L. Kwong, Appl. Phys. Lett. **87**, 051922 (2005).

[21] S. J. Wang, J. W. Chai, J. S. Pan, and A. C. H. Huan, Appl. Phys. Lett. **89**, 022105 (2006).

[22] T. Maeda, M. Nishizawa, Y. Morita, and S. Takagi, Appl. Phys. Lett. **90**, 072911 (2007).

[23] G. Lucovsky, J. P. Long, K.-B. Chung, H. Seo, B. Watts, R. Vasic, and M. D. Ulrich, J. Vac. Sci. Technol. B **27**, 294 (2009).

[24] A. Delabie, F. Bellenger, M. Houssa, T. Conard, S. Van Elshocht, M. Caymax, M. Heyns, and M. Meuris, Appl. Phys. Lett. **91** (2007).

[25] S. Joshi, C. Krug, D. Heh, H. J. Na, H. R. Harris, J. W. Oh, P. D. Kirsch, P. Majhi, B. H. Lee, H. H. Tseng, R. Jammy, J. C. Lee, and S. K. Banerjee, IEEE Electron Device Lett. **28**, 308 (2007).

[26] R. L. Xie, N. Wu, C. Shen, and C. X. Zhu, Appl. Phys. Lett. **93** (2008).

[27] N. Wu, Q. C. Zhang, D. S. H. Chan, N. Balasubramanian, and C. X. Zhu, IEEE Electron Device Lett. **27**, 479 (2006).

[28] H. L. Shang, K. L. Lee, P. Kozlowski, C. D'Emic, I. Babich, E. Sikorski, M. K. Ieong, H. S. P. Wong, K. Guarini, and N. Haensch, IEEE Electron Device Lett. **25**, 135 (2004).

[29] E. R. Engbrecht, Y. M. Sun, K. H. Junker, J. M. White, and J. G. Ekerdt, J. Vac. Sci. Technol. A **22**, 2152 (2004).

[30] P. R. Fitzpatrick and J. G. Ekerdt, J. Vac. Sci. Technol. A **26**, 1397 (2008).

[31] P. R. Fitzpatrick, T. Wang, A. T. Heitsch, B. A. Korgel, and J. G. Ekerdt, Thin Solid Films **In Press, Corrected Proof**.

[32] J. F. Moulder, W. F. Stickle, P. E. Sobol, and K. D. Bomben, *Handbook of X-ray Photoelectron Spectroscopy*. (Physical Electronics, Inc., Eden Prairie, MN, 1995).

[33] C. J. Powell and A. Jablonski, NIST Electron Effective Attenuation Length Database (National Institute of Standards and Technology, Gaithersburg, MD, 2001).

[34] J. F. Wang, J. J. Hu, X. C. Sun, A. M. Agarwal, L. C. Kimerling, D. R. Lim, and R. A. Synowicki, J. Appl. Phys. **104** (2008).

[35] E. Kim, Z. T. Jiang, and K. No, Jpn. J. Appl. Phys. Part 1 - Regul. Pap. Short Notes Rev. Pap. **39**, 4820 (2000).

[36] J. Zhu, C. Jiang, J. Han, and J. Liang, Appl. Phys. A-Mater. Sci. Process. **89**, 497 (2007).

[37] G. Speranza and L. Minati, Diam. Relat. Mat. **16**, 1321 (2007).

[38] D. R. Lide, *CRC Handbook of Chemistry and Physics*, 88 (Internet Version 2008) ed. (CRC Press/Taylor and Francis, Boca Raton, FL, 2008).

[39] H. Aoki, T. Masuzumi, D. Watanabe, M. K. Mazumder, H. Sota, C. Kimura, and T. Sugino, Appl. Surf. Sci. **255**, 3635 (2009).

[40] D. Aubel, M. Diani, L. Kubler, J. L. Bischoff, and D. Bolmont, J. Non-Cryst. Solids **187**, 319 (1995).

[41] G. Lucovsky, S. Lee, J. P. Long, H. Seo, and J. Lüning, Appl. Surf. Sci. **254**, 7933 (2008).

Chapter 5: Summary

5.1. CONCLUSIONS

$BC_{0.75}N_{0.07}$ stoichiometry films were deposited on Ge(100) substrates, and $BCN_{0.07}$ stoichiometry films were deposited on Si(100) substrates. From ISS and ARXPS measurements, it appears the minimum continuous BCN film on Ge(100) is nominally 2.5–5 nm thick, measured by XPS peak attenuation. Subsequent passivation studies involving BCN on Ge(100) targeted a minimum thickness within this range. Below this thickness range there will be exposed portions of Ge(100), which will be free to oxidize during subsequent electronic device processing steps. On Si(100) substrates the required thickness for continuity determined by ISS and ARXPS is 1.5–2 nm.

ARXPS was also used to study the interface bonding of BCN with Ge(100) and Si(100) surfaces. In each case, BCN appears to create a clean, abrupt interface with the substrate. There is no evidence of intermixing with either substrate to create an interfacial layer. BCN bonding in the bulk matched bonding at the Ge(100) and Si(100) surfaces. Analysis of the FWHM of the Ge 3*d*, Ge 2*p*, and Si 2*p* signals before and after BCN deposition suggests that Ge and Si bonding within their respective bulk crystalline lattices is preserved at the interface with BCN.

For passivation purposes, it is critical that an interfacial layer does not form from intermixing of the BCN passivating elements with the Ge(100). Such an occurrence would create mechanical and electrical defects in the Ge. But an abrupt interface is not enough to ensure passivation. It is also essential that the Ge bonding features in the crystalline bulk are preserved at the interface with BCN. It is possible to have an abrupt interface that still distorts the Ge surface bonds. Such a distortion in bonding would

result in interface states, which would reduce charge carrier mobility in an electronic device. The ARXPS analysis in this study shows that the BCN–Ge(100) interface is abrupt and that the Ge bulk bonding is very well preserved at the BCN interface. Based on these criteria, BCN looks to be a promising passivation layer.

Films of $BC_{0.7}N_{0.08}$ stoichiometry were deposited on Ge(100) to test their ability to resist oxidation of Ge in several different oxidizing environments. The minimum BCN thickness that completely covers the Ge(100) substrate and prevents oxidation is ~ 4 nm. XPS analysis of the Ge *3d* spectra shows that a 6.6 nm BCN film resists oxidation of Ge(100) for at least 14 months. A 3.2 nm BCN film, which likely leaves a minor portion of the Ge(100) surface exposed, begins to show signs of GeO_2 formation after 2 months of ambient exposure. GeO_2 forms on an unpassivated control Ge(100) surface within several hours of ambient exposure. Oxidation of the BCN overlayer occurs immediately upon ambient exposure, leading to significant B–O and C–O bonding features within the film. XPS depth profile experiments reveal that this O incorporation saturates at 15% O, with no change in the % O from 2 weeks to 6 months of ambient exposure. This suggests that despite some oxidation of the BCN passivation layer, the underlying Ge(100) is protected.

In situ XPS depth profiles of HfO_2 / BCN / Ge(100) film stacks suggest that continuous BCN also resists formation of GeO_2 and Hf germanide upon exposure to the oxidizing environment of a 250 °C ALD HfO_2 process. Wet oxidation of BCN-coated Ge(100) was studied by immersing samples in 50 °C DI water for up to 20 min and tracking GeO_x formation with XPS. The minimum C-rich $BC_{0.7}N_{0.08}$ film thickness required to resist GeO_x was between 3.0 and 4.0 nm, consistent with the minimum thickness at which BCN resists ambient oxidation of Ge(100).

BCN passivation of GeNWs was also studied. A 5.7 nm BCN film resists oxidation of a GeNW for at least 5 months. HRTEM images upon initial ambient exposure and after 5 months show no change, with BCN forming a sharp, abrupt interface with the Ge surface.

The *C–V* and *I–V* characteristics of MIS capacitors containing HfO_2 dielectric deposited on Ge(100) (n-type) and Si(100) (n-type) passivated with 4.5–5 nm of N-rich BC_xN_y ($0.09 \leq x \leq 0.15$, $0.38 \leq y \leq 0.52$) were measured. BCN deposition temperatures ranging from 275–400 ºC were tested, and an improvement in the electrical characteristics (less hysteresis, less V_{FB} shift, less *C–V* stretch out, and lower leakage current) was observed as the deposition temperature decreased. This was attributed to a decreasing density of bulk and interfacial defects in BCN grown at lower deposition rates, with an Arrhenius relationship between growth rate and temperature observed. The higher level of defects in higher temperature BCN growths is supported by XPS depth profile experiments, which reveal higher rates of ambient O uptake (likely at bulk defect sites) for high temperature growths. Deteriorating electrical properties can also be explained by a decrease in the optical band gap of BCN with decreasing deposition temperature, again possibly related to increased defect densities. C-rich $BC_{0.61}N_{0.08}$ films were also briefly studied, but the effort was abandoned in favor of N-rich films due to large amounts of hysteresis and high levels of fixed negative charge observed for C-rich BCN MIS devices on SiO_2 / Si(100) and Si(100) substrates, respectively.

In general, MIS devices consisting of BCN-passivated Si(100) outperformed BCN-passivated Ge(100) devices. It is speculated that a difference in the interfacial properties of BCN on Si(100) and Ge(100) due to the relative inertness of Ge(100) to thermal nitridation could be the cause. The heightened sensitivity of n-type Ge(100) to band gap alignment issues involving BCN and HfO_2 could also be a factor.

Though reduction of BCN growth temperature improves the electrical performance of MIS capacitors, it is unlikely that the material would serve well as a passivation film for Ge(100). The low band gap of BCN makes the material susceptible to leakage, and the relatively thick (~ 4 nm) layer needed for continuous substrate coverage and oxidation resistance would undesirably increase the EOT due to a decrease in the effective κ value for the dielectric stack. While device performance on Si(100) substrates was improved with a 5 min 400 ºC H_2 PDA and a 30 min 300 ºC H_2 PMA, devices on Ge(100) substrates performed best when only a PDA was performed. The PMA produced high leakage current devices, with poor *C–V* characteristics and a propensity to breakdown at low voltages (< 3V). This suggests that BCN-passivated Ge(100) devices could not withstand the thermal budget experienced during CMOS device processing.

5.2. RECOMMENDATIONS FOR FUTURE WORK

While BCN deposited on Ge(100) creates an abrupt interface that preserves Ge bulk bonding and prevents oxidation of the substrate, the poor electrical performance of BCN on Ge(100) requires a closer inspection of the bulk and interfacial defects that may be responsible. Better insight into the nature of the defects would possibly allow one to tailor the deposition to produce a material with more complete bonding, and hence, better electrical characteristics.

Fourier transform infrared (FTIR) spectroscopy of BCN films would highlight bonding features that are more difficult to extract from the XPS analysis done in this study. FTIR would be especially effective at detecting the presence of different hybridizations of C, which were believed to be responsible for the fixed negative charge in BCN that caused a positive V_{FB} shift. FTIR may also provide better insight into the

nature of O uptake by BCN by separating moisture absorption from O bond formation with B, C, and/or N. The presence of an absorption band attributable to H–O–H would signify that moisture incorporation plays a significant role in the O uptake that was witnessed with XPS.

Knowledge of how the H content depends on the deposition conditions would provide a deeper understanding of the BCN reaction mechanism and the bulk defects that form during film growth. XPS analysis is not sensitive enough to determine the % H present, but dynamic secondary ion mass spectroscopy (SIMS) may provide a qualitative comparison of the H levels present at different stoichiometries and deposition temperatures. Preliminary dynamic SIMS results using Cs^+ incident ions (not reported in this study) revealed a subtle dependence of the relative HCs^+ normalized signal intensity on BCN stoichiometry for films deposited at 350 ºC. C-rich BCN had slightly more H than N-rich BCN when deposited on Si(100), and this trend was exaggerated for Ge(100) substrates, possibly due to the higher substrate temperature of Ge(100).

Steps to reduce the defects at the BCN–Ge(100) interface may also improve the electrical characteristics of devices. Nitridating the Ge(100) surface with NH_3 in a plasma environment would overcome the inertness of Ge(100) to thermal nitridation. Producing such an interface characterized by Ge–N bonding prior to BCN deposition may reduce the interface state densities and produce *C–V* curves that are less stretched out. An initial high temperature (≥ 600 ºC) NH_3 exposure may also achieve this, though the subsequent BCN deposition should be performed at a much lower temperature (< 300 ºC) due to incorporation of bulk defects at high growth rates. Plasma-enhanced CVD of BCN is another approach that would present additional interfacial and bulk bonding features that thermal CVD is incapable of. But it is unlikely that a film with fewer bulk defects would result from a PECVD process due to its aggressive nature.

Ultimately it may be necessary to abandon the DMAB precursor and explore different growth chemistries if the defect density cannot be lowered. BCl_3 is one possible precursor that would shift control of C incorporation to the choice of coreactant gas. Residual C is always detected in the films grown with DMAB because of the dimethyl ligands on the precursor. Borazine and diborane are two other carbon-free precursors, however significant safety concerns accompany the use of these.

All of these approaches to improve BCN–Ge(100) device characteristics would benefit further by carrying them out in a clean room environment. The heightened electrical sensitivity of Ge (relative to Si) to interfacial impurities and band alignment with the insulating dielectric suggests that any interfacial contamination between the cleaned Ge(100) surface and BCN would degrade device performance. Processing in a clean room would significantly reduce this contamination. It is also possible that native Ge–O bonding remains after HF treatment of Ge(100), but it is below the detection limit of XPS. If the native Ge oxide were removed *in situ* by desorption at temperatures ≥ 450 ºC prior to BCN deposition, a cleaner BCN interface could be ensured. Reflection high energy electron diffraction to look for 2 × 1 reconstruction of the Ge(100) surface following oxide desorption would be a highly accurate technique to verify that the starting surface is pristine. The BCN CVD chamber used in this work is incapable of reaching 450 ºC, and even if it was the 2 × 1 reconstruction would not be achieved due to reaction with background B-, C-, and N-containing species during the oxide desorption.

Bibliography

International Technology Roadmap for Semiconductors 2007 Update. (SIA, 2008).

H. Adhikari, P. C. McIntyre, S. Y. Sun, P. Pianetta, and C. E. D. Chidsey, Appl. Phys. Lett. **87** (2005).

W. J. Ahearn, P. R. Fitzpatrick, and J. G. Ekerdt, J. Vac. Sci. Technol. A **25**, 570 (2007).

G. W. Anderson, M. C. Hanf, P. R. Norton, Z. H. Lu, and M. J. Graham, Appl. Phys. Lett. **66**, 1123 (1995).

H. Aoki, D. Watanabe, R. Moriyama, M. K. Mazumder, N. Komatsu, C. Kimura, and T. Sugino, Diamond Relat. Mater. **17**, 628 (2008).

H. Aoki, T. Masuzumi, D. Watanabe, M. K. Mazumder, H. Sota, C. Kimura, and T. Sugino, Appl. Surf. Sci. **255**, 3635 (2009).

J. A. Appelbaum, G. A. Baraff, D. R. Hamann, H. D. Hagstrum, and T. Sakurai, Surf. Sci. **70**, 654 (1978).

D. Aubel, M. Diani, L. Kubler, J. L. Bischoff, and D. Bolmont, J. Non-Cryst. Solids **187**, 319 (1995).

W. P. Bai, N. Lu, A. Ritenour, M. L. Lee, D. A. Antoniadis, and D. L. Kwong, IEEE Electron Device Lett. **27**, 175 (2006).

D. Bodlaki, H. Yamamoto, D. H. Waldeck, and E. Borguet, Surf. Sci. **543**, 63 (2003).

H. H. Brongersma and J. P. Jacobs, Appl. Surf. Sci. **75**, 133 (1994).

H. H. Brongersma, M. Draxler, M. de Ridder, and P. Bauer, Surface Science Reports **62**, 63 (2007).

M. Caymax, M. Houssa, G. Pourtois, F. Bellenger, K. Martens, A. Delabie, and S. Van Elshocht, Appl. Surf. Sci. **254**, 6094 (2008).

Y. J. Chabal, Surf. Sci. **168**, 594 (1986).

R. Champaneria, P. Mack, R. White, and J. Wolstenholme, Surf. Interface Anal. **35**, 1028 (2003).

L. Chen, T. Goto, T. Hirai, and T. Amano, J. Mater. Sci. Lett. **9**, 997 (1990).

K. Choi and J. M. Buriak, Langmuir **16**, 7737 (2000).

S. M. Cohen, T. I. Hukka, Y. L. Yang, and M. P. D'Evelyn, Thin Solid Films **225**, 155 (1993).

G. W. Cullen, J. A. Amick, and D. Gerlixh, J. Electrochem. Soc. **109**, 124 (1962).

A. Delabie, F. Bellenger, M. Houssa, T. Conard, S. Van Elshocht, M. Caymax, M. Heyns, and M. Meuris, Appl. Phys. Lett. **91** (2007).

E. R. Engbrecht, Y. M. Sun, K. H. Junker, J. M. White, and J. G. Ekerdt, J. Vac. Sci. Technol. A **22**, 2152 (2004).

E. R. Engbrecht, Y. M. Sun, K. H. Junker, J. M. White, and J. G. Ekerdt, J. Vac. Sci. Technol. B **23**, 463 (2005).

E. R. Engbrecht, P. R. Fitzpatrick, K. H. Junker, Y. M. Sun, J. M. White, and J. G. Ekerdt, J. Mater. Res. **20**, 2218 (2005).

B. Feddes, A. M. Vredenberg, J. G. C. Wolke, and J. A. Jansen, Surf. Interface Anal. **35**, 287 (2003).

P. R. Fitzpatrick and J. G. Ekerdt, J. Vac. Sci. Technol. A **26**, 1397 (2008).

P. R. Fitzpatrick, T. Wang, A. T. Heitsch, B. A. Korgel, and J. G. Ekerdt, Thin Solid Films **In Press, Corrected Proof**.

C. Guimon, D. Gonbeau, G. Pfisterguillouzo, O. Dugne, A. Guette, R. Naslain, and M. Lahaye, Surf. Interface Anal. **16**, 440 (1990).

R. J. Hamers, J. S. Hovis, C. M. Greenlief, and D. F. Padowitz, Jpn. J. Appl. Phys., Part 1 **38**, 3879 (1999).

S. M. Han, W. R. Ashurst, C. Carraro, and R. Maboudian, J. Am. Chem. Soc. **123**, 2422 (2001).

T. Hanrath and B. A. Korgel, J. Am. Chem. Soc. **124**, 1424 (2002).

T. Hanrath and B. A. Korgel, J. Am. Chem. Soc. **126**, 15466 (2004).

T. Hanrath and B. A. Korgel, J. Phys. Chem. B **109**, 5518 (2005).

J. L. He, Z. H. Lu, S. A. Mitchell, and D. D. M. Wayner, J. Am. Chem. Soc. **120**, 2660 (1998).

M. Houssa, G. Pourtois, B. Kaczer, B. De Jaeger, F. E. Leys, D. Nelis, K. Paredis, A. Vantomme, M. Caymax, M. Meuris, and M. M. Heyns, Microelectron. Eng. **84**, 2267 (2007).

S. Joshi, C. Krug, D. Heh, H. J. Na, H. R. Harris, J. W. Oh, P. D. Kirsch, P. Majhi, B. H. Lee, H. H. Tseng, R. Jammy, J. C. Lee, and S. K. Banerjee, IEEE Electron Device Lett. **28**, 308 (2007).

E. Kim, Z. T. Jiang, and K. No, Jpn. J. Appl. Phys. Part 1 - Regul. Pap. Short Notes Rev. Pap. **39**, 4820 (2000).

H. Kim, P. C. McIntyre, C. O. Chui, K. C. Saraswat, and M.-H. Cho, Appl. Phys. Lett. **85**, 2902 (2004).

R. H. Kingston, J. Appl. Phys. **27**, 101 (1956).

M. Koto, P. W. Leu, and P. C. McIntyre, J. Electrochem. Soc. **156**, K11 (2009).

I. Kusunoki, T. Takagaki, S. Ishidzuka, Y. Igari, and T. Takaoka, Surf. Sci. **380**, 131 (1997).

C. H. Lee, T. D. Lin, L. T. Tung, M. L. Huang, M. Hong, and J. Kwo, J. Vac. Sci. Technol. B **26**, 1128 (2008).

S. W. Lee, L. N. Nelen, H. Ihm, T. Scoggins, and C. M. Greenlief, Surf. Sci. **410**, L773 (1998).

M. K. Lei, Q. Li, Z. F. Zhou, I. Bello, C. S. Lee, and S. T. Lee, Thin Solid Films **389**, 194 (2001).

B. Li, B. Xiong, L. N. Jiang, Y. Zohar, and M. Wong, J. Microelectromech. Syst. **8**, 366 (1999).

D. R. Lide, *CRC Handbook of Chemistry and Physics*, 88 (Internet Version 2008) ed. (CRC Press/Taylor and Francis, Boca Raton, FL, 2008).

P. W. Loscutoff and S. F. Bent, Annu. Rev. Phys. Chem. **57**, 467 (2006).

N. Lu, W. Bai, A. Ramirez, C. Mouli, A. Ritenour, M. L. Lee, D. Antoniadis, and D. L. Kwong, Appl. Phys. Lett. **87**, 051922 (2005).

Z. H. Lu, Appl. Phys. Lett. **68**, 520 (1996).

G. Lucovsky, S. Lee, J. P. Long, H. Seo, and J. Lüning, Appl. Surf. Sci. **254**, 7933 (2008).

G. Lucovsky, J. P. Long, K.-B. Chung, H. Seo, B. Watts, R. Vasic, and M. D. Ulrich, J. Vac. Sci. Technol. B **27**, 294 (2009).

P. F. Lyman, O. Sakata, D. L. Marasco, T. L. Lee, K. D. Breneman, D. T. Keane, and M. J. Bedzyk, Surf. Sci. **462**, L594 (2000).

P. Mack, R. G. White, J. Wolstenholme, and T. Conard, Appl. Surf. Sci. **252**, 8270 (2006).

T. Maeda, M. Nishizawa, Y. Morita, and S. Takagi, Appl. Phys. Lett. **90**, 072911 (2007).

J. Y. Maeng, J. Y. Lee, Y. E. Cho, S. Kim, and S. K. Jo, Appl. Phys. Lett. **81**, 3555 (2002).

H. Matsubara, T. Sasada, M. Takenaka, and S. Takagi, Appl. Phys. Lett. **93** (2008).

M. Mieno and T. Satoh, J. Mater. Sci. **36**, 3925 (2001).

G. E. Moore, Electronics **38**, 114 (1965).

A. M. Morales and C. M. Lieber, Science **279**, 208 (1998).

J. F. Moulder, W. F. Stickle, P. E. Sobol, and K. D. Bomben, *Handbook of X-ray Photoelectron Spectroscopy*. (Physical Electronics, Inc., Eden Prairie, MN, 1995).

Q. D. Nghiem and D. P. Kim, J. Mater. Chem. **15**, 2188 (2005).

G. Nicholas, D. P. Brunco, A. Dimoulas, J. Van Steenbergen, F. Bellenger, M. Houssa, M. Caymax, M. Meuris, Y. Panayiotatos, and A. Sotiropoulos, IEEE Trans. Electron Devices **54**, 1425 (2007).

M. Oehme, J. Werner, M. Kaschel, O. Kirfel, and E. Kasper, Thin Solid Films **517**, 137 (2008).

L. Papagno, X. Y. Shen, J. Anderson, G. S. Spagnolo, and G. J. Lapeyre, Phys. Rev. B **34**, 7188 (1986).

K. Park, Y. Lee, J. Lee, and S. Lim, Appl. Surf. Sci. **254**, 4828 (2008).

D. Poelman, P. Clauws, and B. Depuydt, Sol. Energy Mater. **76**, 167 (2003).

C. J. Powell and A. Jablonski, NIST Electron Effective Attenuation Length Database (National Institute of Standards and Technology, Gaithersburg, MD, 2001).

K. Prabhakaran and T. Ogino, Surf. Sci. **325**, 263 (1995).

M. S. Rahman, E. K. Evangelou, I. I. Androulidakis, A. Dimoulas, G. Mavrou, and P. Tsipas, J. Vac. Sci. Technol. B **27**, 439 (2009).

A. Ritenour, A. Khakifirooz, D. A. Antoniadis, R. Z. Lei, W. Tsai, A. Dimoulas, G. Mavrou, and Y. Panayiotatos, Appl. Phys. Lett. **88** (2006).

K. Saraswat, C. O. Chui, T. Krishnamohan, D. Kim, A. Nayfeh, and A. Pethe, Mater. Sci. Eng., B **135**, 242 (2006).

D. Schmeisser, R. D. Schnell, A. Bogen, F. J. Himpsel, D. Rieger, G. Landgren, and J. F. Morar, Surf. Sci. **172**, 455 (1986).

A. D. Schricker, S. V. Joshi, T. Hanrath, S. K. Banerjee, and B. A. Korgel, J. Phys. Chem. B **110**, 6816 (2006).

M. P. Seah and S. J. Spencer, Surf. Interface Anal. **33**, 640 (2002).

M. P. Seah and R. White, Surf. Interface Anal. **33**, 960 (2002).

H. L. Shang, K. L. Lee, P. Kozlowski, C. D'Emic, I. Babich, E. Sikorski, M. K. Ieong, H. S. P. Wong, K. Guarini, and N. Haensch, IEEE Electron Device Lett. **25**, 135 (2004).

G. Speranza and L. Minati, Diam. Relat. Mat. **16**, 1321 (2007).

B. G. Streetman and S. Banerjee, *Solid State Electronic Devices*, Fifth Edition ed. (Prentice Hall, Upper Saddle River, New Jersey, 2000).

T. Sugawara, Y. Oshima, R. Sreenivasan, and P. C. McIntyre, Appl. Phys. Lett. **90** (2007).

T. Sugiyama, T. Tai, and T. Sugino, Appl. Phys. Lett. **80**, 4214 (2002).

B. P. Swain, Surf. Coat. Technol. **201**, 1589 (2006).

S. M. Sze, *Physics of Semiconductor Devices*, Second ed. (John Wiley & Sons, New York, 1981).

S. M. Sze and K. K. Ng, *Physics of Semiconductor Devices*, 3rd ed. (John Wiley & Sons, Inc., Hoboken, N.J., 2007).

S. Takagi, T. Maeda, N. Taoka, M. Nishizawa, Y. Morita, K. Ikeda, Y. Yamashita, M. Nishikawa, H. Kumagai, R. Nakane, S. Sugahara, and N. Sugiyama, Microelectron. Eng. **84**, 2314 (2007).

S. Tanuma, C. J. Powell, and D. R. Penn, Surf. Interface Anal. **17**, 927 (1991).

H. Temkin, T. P. Pearsall, J. C. Bean, R. A. Logan, and S. Luryi, Appl. Phys. Lett. **48**, 963 (1986).

A. V. Teplyakov, P. Lal, Y. A. Noah, and S. F. Bent, J. Am. Chem. Soc. **120**, 7377 (1998).

A. Toneva, T. Marinova, and V. Krastev, J. Lumin. **80**, 455 (1998).

M. N. Uddin, M. Shimoyama, Y. Baba, T. Sekiguchi, and M. Nagano, J. Vac. Sci. Technol. A **23**, 497 (2005).

S. Umeda, T. Yuki, T. Sugiyama, and T. Sugino, Diamond Relat. Mater. **13**, 1135 (2004).

S. Van Elshocht, M. Caymax, T. Conard, S. De Gendt, I. Hoflijk, M. Houssa, F. Leys, R. Bonzom, B. De Jaeger, J. Van Steenbergen, W. Vandervorst, M. Heyns, and M. Meuris, Thin Solid Films **508**, 1 (2006).

R. G. Vitchev, J. J. Pireaux, T. Conard, H. Bender, J. Wolstenholme, and C. Defranoux, Appl. Surf. Sci. **235**, 21 (2004).

D. W. Wang, Y. L. Chang, Z. Liu, and H. J. Dai, J. Am. Chem. Soc. **127**, 11871 (2005).

D. W. Wang, Y. L. Chang, Q. Wang, J. Cao, D. B. Farmer, R. G. Gordon, and H. J. Dai, J. Am. Chem. Soc. **126**, 11602 (2004).

D. W. Wang, Q. Wang, A. Javey, R. Tu, H. J. Dai, H. Kim, P. C. McIntyre, T. Krishnamohan, and K. C. Saraswat, Appl. Phys. Lett. **83**, 2432 (2003).

J. F. Wang, J. J. Hu, X. C. Sun, A. M. Agarwal, L. C. Kimerling, D. R. Lim, and R. A. Synowicki, J. Appl. Phys. **104** (2008).

S. J. Wang, J. W. Chai, J. S. Pan, and A. C. H. Huan, Appl. Phys. Lett. **89**, 022105 (2006).

N. Wu, Q. C. Zhang, D. S. H. Chan, N. Balasubramanian, and C. X. Zhu, IEEE Electron Device Lett. **27**, 479 (2006).

R. L. Xie, N. Wu, C. Shen, and C. X. Zhu, Appl. Phys. Lett. **93** (2008).

X. F. Zhang, J. P. Xu, C. X. Li, P. T. Lai, C. L. Chan, and J. G. Guan, Appl. Phys. Lett. **92** (2008).

Z. J. Zhang, C. Kimura, and T. Sugino, J. Appl. Phys. **98**, 036105 (2005).

Z. F. Zhou, I. Bello, M. K. Lei, K. Y. Li, C. S. Lee, and S. T. Lee, Surf. Coat. Technol. **128-129**, 334 (2000).

J. Zhu, C. Jiang, J. Han, and J. Liang, Appl. Phys. A-Mater. Sci. Process. **89**, 497 (2007).

Vita

Patrick Ryan Fitzpatrick graduated from the Governor's School for Government and International Studies in Richmond, VA in June 1999. In September 1999 he enrolled at the University of Virginia, in Charlottesville, Virginia, earning the distinction of Rodman Scholar from the School of Engineering and Applied Science. In May 2003 he received a Bachelor of Science in Chemical Engineering, graduating with high distinction. During the summer of 2002 he conducted undergraduate research at IBM's Almaden Research Center in San Jose, CA. There he studied humidity effects on the rheological properties of perflouropolyether magnetic recording disk lubricants under the guidance of Dr. Tom E. Karis. Upon returning to the University of Virginia, he produced an undergraduate thesis from his rheological studies at IBM under the mentorship of Prof. James Oberhauser.

Ryan began graduate school at The University of Texas at Austin in September 2003. Advised by Prof. John G. Ekerdt, his initial graduate research focused on the growth of boron carbo-nitride (BCN) films by chemical vapor deposition and their use as an insulating diffusion barrier for copper interconnects. In 2004 this transitioned to a study of the material's ability to seal porous low-κ dielectrics from the penetration of metallic precursors. Ryan's graduate work was put on hold in 2005 to do a 6 month internship at IBM East Fishkill in Hopewell Junction, NY. There he worked with a front-end integration team studying the electrical performance and reliability of gate oxides under development for next generation transistors. Upon returning to The University of

Texas in November 2005, he worked for one year modifying an existing growth and analysis system to implement a novel silicon nitride deposition capability. In the fall of 2006 Ryan returned to working with BCN and studied its ability to serve as a passivation layer for germanium surfaces, which became the focus of his PhD dissertation.

During Ryan's second year at The University of Texas he served as the co-chair of the department's Graduate Student Executive Committee. In 2007 / 2008 he served as the Corporate Relations Director for the Graduate And Industry Networking conference, which took place in February, 2008. During his first two years at The University of Texas he received an Engineering Foundation Endowed Presidential Scholarship, and he received a Thrust Fellowship during his remaining years.

Ryan has authored or co-authored six publications submitted to refereed journals. He has presented his research results at the MRS Spring Meeting in San Francisco, CA, in March 2005 and the AVS 54th International Symposium in Seattle, WA, in October 2007.

Permanent address: 4800 Cap Rock Dr, Austin, TX 78735

This dissertation was typed by the author.